University of Pennsylvania
ScholarlyCommons

Publicly Accessible Penn Dissertations

2017

Rotorcraft Blade Pitch Control Through Torque Modulation

James John Paulos
University of Pennsylvania, jpaulos@gmail.com

Follow this and additional works at: https://repository.upenn.edu/edissertations

Part of the Aerospace Engineering Commons, and the Robotics Commons

Recommended Citation

Paulos, James John, "Rotorcraft Blade Pitch Control Through Torque Modulation" (2017). *Publicly Accessible Penn Dissertations*. 2901.
https://repository.upenn.edu/edissertations/2901

This paper is posted at ScholarlyCommons. https://repository.upenn.edu/edissertations/2901
For more information, please contact repository@pobox.upenn.edu.

Rotorcraft Blade Pitch Control Through Torque Modulation

Abstract

Micro air vehicle (MAV) technology has broken with simple mimicry of manned aircraft in order to fulfill emerging roles which demand low-cost reliability in the hands of novice users, safe operation in confined spaces, contact and manipulation of the environment, or merging vertical flight and forward flight capabilities. These specialized needs have motivated a surge of new specialized aircraft, but the majority of these design variations remain constrained by the same fundamental technologies underpinning their thrust and control. This dissertation solves the problem of simultaneously governing MAV thrust, roll, and pitch using only a single rotor and single motor. Such an actuator enables new cheap, robust, and light weight aircraft by eliminating the need for the complex ancillary controls of a conventional helicopter swashplate or the distributed propeller array of a quadrotor.

An analytic model explains how cyclic blade pitch variations in a special passively articulated rotor may be obtained by modulating the main drive motor torque in phase with the rotor rotation. Experiments with rotors from 10 cm to 100 cm in diameter confirm the predicted blade lag, pitch, and flap motions. We show the operating principle scales similarly as traditional helicopter rotor technologies, but is subject to additional new dynamics and technology considerations. Using this new rotor, experimental aircraft from 29 g to 870 g demonstrate conventional flight capabilities without requiring more than two motors for actuation. In addition, we emulate the unusual capabilities of a fully actuated MAV over six degrees of freedom using only the thrust vectoring qualities of two teetering rotors. Such independent control over forces and moments has been previously obtained by holonomic or omnidirection multirotors with at least six motors, but we now demonstrate similar abilities using only two. Expressive control from a single actuator enables new categories of MAV, illustrated by experiments with a single actuator aircraft with spatial control and a vertical takeoff and landing airplane whose flight authority is derived entirely from two rotors.

Degree Type

Dissertation

Degree Name

Doctor of Philosophy (PhD)

Graduate Group

Mechanical Engineering & Applied Mechanics

First Advisor

Mark H. Yim

Keywords

dynamics, helicopter, MAV, robotics, swashplate

Subject Categories

Aerospace Engineering | Robotics

This dissertation is available at ScholarlyCommons: https://repository.upenn.edu/edissertations/2901

ROTORCRAFT BLADE PITCH CONTROL THROUGH TORQUE MODULATION

James J. Paulos

A DISSERTATION

in

Mechanical Engineering and Applied Mechanics

Presented to the Faculties of the University of Pennsylvania

in

Partial Fulfillment of the Requirements for the

Degree of Doctor of Philosophy

2017

Mark H. Yim, Supervisor of Dissertation
Professor of Mechanical Engineering and Applied Mechanics
and Director of Integrated Product Design

Kevin T. Turner, Graduate Group Chairperson
Professor of Mechanical Engineering and Applied Mechanics

Dissertation Committee

Daniel E. Koditschek, Alfred Fitler Moore Professor of Electrical and Systems Engineering and Director of PERCH, University of Pennsylvania
Bruce D. Kothmann, Senior Lecturer of Mechanical Engineering and Applied Mechanics, University of Pennsylvania
R. Vijay Kumar, Professor of Mechanical Engineering and Applied Mechanics and Nemirovsky Family Dean of Penn Engineering, University of Pennsylvania
Paul Pounds, Senior Lecturer in Mechatronics, University of Queensland
Mark H. Yim, Professor of Mechanical Engineering and Applied Mechanics and Director of Integrated Product Design, University of Pennsylvania

ROTORCRAFT BLADE PITCH CONTROL THROUGH TORQUE MODULATION

© COPYRIGHT

2017

James J. Paulos

Acknowledgments

I would like to thank my advisor, Mark Yim, for nurturing a lab culture full of worthy distractions as well as giving me the personal encouragement and freedom to pursue this work. I am also grateful to Vijay Kumar, Dan Koditschek, Paul Pounds, and Bruce Kothmann for serving on my dissertation committee. Among them I have found inspiration, challenge, boundless enthusiasm, and good natured incredulity all to my benefit.

I would like to thank Terry Kientz and Jeremy Wang for their help and creativity in preparing some of my experiments, and I also must thank Charity Payne and Gaby Alfaro for making the GRASP Lab and PERCH such a special place to work. Matt Piccoli gave me a running start into aerial robotics research, and I benefited enormously from our conversations and collaborations. I would like to acknowledge all of the support I've received from my friends in the Modlab and GRASP Labs and especially the undergraduate and masters students who have helped me in this work including Bennet C., Makarios C., Bhavya G., Erica K., Ashish M., Holden M., Julian M., Lindsey M., Brad P., and Mutian Z.

I am indebted to Ephrahim Garcia, my advisor at Cornell, who introduced me to graduate research, pushed hard, and encouraged me to embark on this path.

I am grateful for the support of my family, who seeded every opportunity I have enjoyed and have cheered me along the way. I am especially fortunate for the loving support and patience of my wife, Suzanna, who has believed in me from the very beginning.

ABSTRACT

ROTORCRAFT BLADE PITCH CONTROL THROUGH TORQUE MODULATION

James J. Paulos

Mark H. Yim

Micro air vehicle (MAV) technology has broken with simple mimicry of manned aircraft in order to fulfill emerging roles which demand low-cost reliability in the hands of novice users, safe operation in confined spaces, contact and manipulation of the environment, or merging vertical flight and forward flight capabilities. These specialized needs have motivated a surge of new specialized aircraft, but the majority of these design variations remain constrained by the same fundamental technologies underpinning their thrust and control. This dissertation solves the problem of simultaneously governing MAV thrust, roll, and pitch using only a single rotor and single motor. Such an actuator enables new cheap, robust, and light weight aircraft by eliminating the need for the complex ancillary controls of a conventional helicopter swashplate or the distributed propeller array of a quadrotor.

An analytic model explains how cyclic blade pitch variations in a special passively articulated rotor may be obtained by modulating the main drive motor torque in phase with the rotor rotation. Experiments with rotors from 10 cm to 100 cm in diameter confirm the predicted blade lag, pitch, and flap motions. We show the operating principle scales similarly as traditional helicopter rotor technologies, but is subject to additional new dynamics and technology considerations. Using this new rotor, experimental aircraft from 29 g to 870 g demonstrate conventional flight capabilities without requiring more than two motors for actuation. In addition, we emulate the unusual capabilities of a fully actuated MAV over six degrees of freedom using only the thrust vectoring qualities of two teetering rotors. Such independent control over forces and moments has been previously obtained by holonomic or omnidirection multirotors with at least six motors, but we now demonstrate similar abilities using only two. Expressive control from a single actuator enables new categories of MAV, illustrated by experiments with a single actuator aircraft with spatial control and a vertical takeoff and landing airplane whose flight authority is derived entirely from two rotors.

Contents

Acknowledgments iii

Abstract iv

Contents v

List of Tables viii

List of Figures ix

Nomenclature xii

1 Introduction 1

2 Background and Related Work 5
- 2.1 Quadrotor and Multirotor MAV . . . 6
- 2.2 Control Surfaces and Gimbaled Actuators . . . 8
- 2.3 Cyclic Blade Pitch Control . . . 9
- 2.4 Torque Modulating Cyclic Control . . . 13

3 Design and Modeling 16
- 3.1 Basic Operating Principle . . . 16
- 3.2 Design and Kinematics . . . 18
- 3.3 Dynamical Model . . . 22
- 3.4 Open-Chain Dynamics . . . 22
- 3.5 Aerodynamic Forces . . . 26
- 3.6 Hinge Losses . . . 30
- 3.7 Motor Equation And Speed Governor . . . 33
- 3.8 Equilibrium . . . 35
- 3.9 Linearized System Equations . . . 37
- 3.10 Illustrative Simplified Models . . . 39
  - 3.10.1 Flapping . . . 39
  - 3.10.2 Lead-Lag . . . 40

4 Rotor Experiments 45
- 4.1 Prototype Construction . . . 45

4.2 Experiments 47
4.3 Motor Torque 48
4.4 Hub Speed Response 50
4.5 Lag Response 51
4.6 Flap Response 54

5 Scaling 57
5.1 Isolated Rotor Scaling 58
  5.1.1 Prescriptive Requirements for Dynamic Similarity 58
  5.1.2 Extrapolation Across Scale and Speed 61
  5.1.3 Experimental Confirmation 62
5.2 Impact of Rotor Size 71
5.3 Impact of Vehicle Size 72
5.4 Practical Limitations for Manned Helicopters 75

6 Flight Without a Swashplate 76
6.1 Coaxial Helicopter 76
6.2 Electrical Design 77
6.3 Control Rates and Timescales 78
6.4 Attitude Control 79
6.5 Trajectory Tracking 81
6.6 Power for Hover 82
  6.6.1 Symmetric Loading 82
  6.6.2 Asymmetric Loading 84
6.7 Actuator Mass Budget 85
6.8 Manufacturability and Cost 87
6.9 Acoustics 87
6.10 Other Coaxial Helicopter Demonstrations 88
  6.10.1 Larger MAV with Loosely Integrated Avionics 88
  6.10.2 Smaller MAV With Highly Integrated Avionics 88

7 Emulating a Fully Actuated MAV 92
7.1 Underactuated and Fully Actuated Aircraft 92
7.2 Idealized Vehicle Dynamics 94
7.3 Implementation Of Thrust Vectoring 96
7.4 Hardware Design 99
7.5 Control Design 101
7.6 Flight Experiments 102
  7.6.1 Orientation Control in Hover 102
  7.6.2 Acceleration without Pitch or Roll 104
  7.6.3 Smooth Trajectory Following 104
7.7 Applications and Future Work 107

8 Future Aircraft Formats 109
8.1 Single Motor Aircraft 109
8.2 VTOL Flying Wing Aircraft 111

9 Conclusion **114**

Appendices **118**

A Motor Drive System Identification **119**
A.1 Method 1: Speed and Torque Measurement 120
A.2 Method 2: Speed Measurement with Proof Mass Flywheel 124

Bibliography **128**

List of Tables

3.1 Undamped flap frequency ratio. 40
3.2 Undamped lag frequency ratio. 43

4.1 Propeller properties. 46
4.2 Motor properties and control gains for 200 rad/s test speed. 47

5.1 Characteristic scales for nondimensionalization. 59
5.2 Nondimensional parameter groups. 59
5.3 Dimensional basis and isometric scaling result for model quantities. 61
5.4 Rotor assembly properties. 63
5.5 Motor properties. 63
5.6 Nondimensional Parameters. 63
5.7 Scaling at constant thrust. 71
5.8 Froude scaling for isometric vehicle and rotor growth. 74

6.1 Mass budget of coaxial helicopter shown in Fig. 6.1. 86
6.2 Mass budget of original coaxial helicopter. 89

8.1 VTOL fixed wing aircraft properties. 113

9.1 Flight validation experiments. 116

A.1 Quanum MT 2212 motor properties from speed and torque. 121
A.2 AP03 motor properties obtained by speed and torque. 121
A.3 U13 motor properties from flywheel tests. 125
A.4 AP03 motor properties from flywheel tests. 125

List of Figures

2.1 Quadrotor control moments generated by differential lift and drag. 6
2.2 Schematic drawing of swashplate. 10
2.3 Azimuthal location of maximum cyclic blade pitch in order to obtain a pure aircraft pitching response. Adapted from [15]. 12
2.4 Stabilizer bar for the upper rotor of the Blade CX2 coaxial helicopter. 12
2.5 Swashplate for the lower rotor of the Blade CX2 coaxial helicopter. 12
2.6 US patent figures for the Keyence Corporation Revolutor model helicopter [74]. 14
2.7 German patent figure shows concept for attitude control with a hinged propeller [18]. 15

3.1 Two blades are attached by canted hinges to a hub directly affixed to the main motor. 16
3.2 As the positive blade lags backwards, the pitch increases. As it leads forward, the pitch decreases. 17
3.3 Positive and negative blades respond 180° out of phase with each other. . . . 17
3.4 Serial flap and lag hinges resemble a skewed universal joint. The the hub and blade grip are connected by an intermediate cross which carries the pin joints. 18
3.5 The flap and lag-pitch hinges are approximately co-located at radius eR. In the reference pose the lag-pitch axis is skewed by angle δ from vertical. 19
3.6 For analysis, the kinematics are approximated by conventional flap angle β and lag angle ζ about orthogonal axis vectors fixed in the rotating hub frame. A lag-pitch coupling coefficient is imposed separately. 20
3.7 Center of mass r_{cm}, radius of gyration k, and center of oscillation l. 24
3.8 Flap frequency ratio. 40
3.9 Lag frequency ratio. 43

4.1 Power electronics, motor, and articulated hub for a 318 mm diameter cyclic rotor. 47
4.2 Measured motor torque response compared with model prediction for a range of normalized drive torque amplitudes u at three test speeds. 49
4.3 Cumulative measurements over one second of operation at 200 rad/s show a hub speed response phase locked to hub orientation. Results with and without an applied sinusoidal drive voltage are shown. 50
4.4 Measured hub speed response compared with model prediction for a range of normalized drive torque amplitudes u at three test speeds. 51

4.5 The cyclic lag angle response for the positive lag-pitch coupled blade is measured at an operating speed of 200 rad/s with and without an exciting voltage amplitude. 52
4.6 Measured blade lag angle response compared with model prediction at three speeds for both the positive and negative lag-pitch coupling blades. 53
4.7 The positive coefficient blade begins on the right side at peak downward flap, and achieves maximum upward flap 180° later in the rotation. 55
4.8 The cyclic flap angle response for the positive lag-pitch coupled blade is measured directly at a rotor speed of 200 rad/s with and without an exciting voltage amplitude. 55
4.9 Measured blade flap angle response compared with model prediction at three test speeds. The positive coupling blade response is approximately 180° out of phase with the negative coupling blade. 56

5.1 10 cm diameter rotor. 64
5.2 10 cm diameter rotor with motor and motor controller. 64
5.3 1 m diameter rotor. 64
5.4 1 m diameter rotor on test stand with motor and motor controller. 65
5.5 1 m diameter rotor with inertial flybar and fiducial markers. 65
5.6 Hub speed response in small rotor. 67
5.7 Hub speed response in large rotor. 67
5.8 Lag (pitch) angle response in small rotor. 69
5.9 Lag (pitch) angle response in large rotor. 69
5.10 Flap angle response in small rotor. 70
5.11 Flap angle response in large rotor. 70
5.12 Production helicopter mass vs rotor diameter. 73

6.1 A 227 g coaxial MAV exhibits cyclic control without a swashplate or any additional actuators. 77
6.2 Representative frequencies. The attitude control rate is decoupled from both the rotor speed and PWM synthesis of the pulsing torque. 78
6.3 The controller operates on an estimated orientation and angular rate ($\hat{q}$, $\hat{w}$) and desired values ($\bar{q}$, $\bar{w}$). Outputs are mean drive voltages u_{bottom}, u_{top} and an additive sinusoidal component of amplitude A and phase ϕ. 79
6.4 A 20 cm step in desired position towards the right results in a roll response and corrective lateral motion. 82
6.5 Automated tracking of a spiral ascent to 1.5 m height, a 1.5 m radius circuit at 1 m/s, and return to origin. 82
6.6 Electrical power consumption in hover with various payload masses. 83
6.7 Rotor speed of the top (pulsing) and bottom (non-pulsing) propellers in hover with various payload masses. 83
6.8 Electrical power consumption in hover with a 10 g payload offset laterally from the vehicle center. 85
6.9 Rotor speed of the top (pulsing) and bottom (non-pulsing) propellers in hover with a 10 g payload offset laterally from the vehicle center. 85

6.10 The swashplate and servomotors are a large fraction of the mass in a conventional coaxial helicopter (Blade CX2) but are eliminated in a pulsing coaxial helicopter and in quadrotors (ensemble averages from [52]). 86
6.11 First coaxial helicopter to incorporate the dynamic cyclic rotor. 89
6.12 A 37 g coaxial MAV with onboard camera. 90
6.13 Pin hinge hub and alternative one-piece flexible hub. 91
6.14 Polyurethane overmolding of flexible polyethylene sheet. 91

7.1 Teetering rotors allow independent control of force and moments. 95
7.2 Teetering rotor with skewed lag-pitch hinges. 97
7.3 Top rotor of coaxial helicopter. 99
7.4 Coaxial helicopter. 100
7.5 Bench measurements of lateral forces and increasing voltage modulation amplitude. 100
7.6 Tip path plane transition over 200 ms shown with ±12° reference. 101
7.7 Conventional trajectory control for underactuated quadrotor. 102
7.8 Fully actuated trajectory and orientation control. 102
7.9 Stationary hover while pitching from $-8°$ to $8°$. 103
7.10 Acceleration at 1 m/s^2 while maintaining flat attitude. 105
7.11 Flight at 0.5 m/s into a circle of radius 35 cm. 106
7.12 Rapid changes in desired acceleration tracked while maintaining vertical orientation. 106

8.1 UNO, a single motor MAV. Photo credit: Matthew Piccoli [68]. 110
8.2 VTOL flying wing aircraft with only two motors. 112
8.3 Rotor tilt for roll and yaw maneuvers. Photo credit: Ashish Macwan. 113

A.1 Speed frequency response for medium 22 mm size motor. 122
A.2 Torque frequency response for medium 22 mm size motor. 122
A.3 Speed frequency response for small 11 mm size motor. 123
A.4 Torque frequency response for small 11 mm size motor. 123
A.5 Speed frequency response of large U13 105 mm size motor with inertial flywheel. 126
A.6 Inertia regression for large U13 105 mm size motor. 126
A.7 Speed frequency response of small AP03 11 mm size motor with inertial flywheel. 127
A.8 Inertia regression for small AP03 11 mm size motor. 127

Nomenclature

a	section lift curve slope
A_β, A_ζ	flap and lag amplitude, rad
c	section chord length, m
c_{d_0}	section drag coefficient
c_β, c_ζ	equivalent flap and lag hinge damping
c_m, k_m	motor damping and stiffness coefficients
C_Q	torque coefficient, $C_Q = Q/\rho\pi R^5\Omega^2$
dD, dL	differential drag and lift forces, N
e	offset hinge eccentricity
dF_y, dF_z	differential section forces, N
G_D, G_P	hinge geometry coefficients for disk and pin
i, i_0	motor current and no-load current, A
I_β	flap inertia, $\mathrm{kg\,m^2}$
I_h	hub inertia, $\mathrm{kg\,m^2}$
K_e	motor emf constant, V/(rad/s) or N m/A
K_I, K_P	integral and proportional control gains
N_b	number of blades
Q	shaft torque, N m
R	blade tip radius, m
R_D, R_P	hinge disk and pin radius, m
R_{ohm}	motor electrical resistance, ohms
u	additive modulation input
U_∞	incident velocity, m/s
U_P, U_T	perpendicular and tangential incident velocity, m/s
v_i	inflow velocity, m/s
V	total motor terminal voltage, V
$\tilde{V}$	additive modulation voltage, V
X_{I_h}	hub inertia ratio, $X_{I_h} = I_h/(N_b I_\beta)$
α	angle of attack, rad
β	flap angle, rad
γ	Lock number, $\gamma = \rho a c R^4/I_\beta$
δ	skew lag-pitch hinge angle, rad
ζ	lag angle, rad
θ	blade pitch, rad
$\Delta\theta/\Delta\zeta$	geometric lag-pitch coupling coefficient

θ_1, θ_2	axis rotation angles, rad
μ_1	friction coefficient steel-plastic
μ_2	friction coefficient PTFE-PTFE
ξ	spanwise blade station
ρ	air density, kg/m^3
σ	rotor solidity, $\sigma = N_b c/(\pi R)$
ϕ	inflow angle, rad, $\phi = U_P/U_T$
ϕ_i	downwash angle, rad, $\phi_i = v_i/(\Omega R \xi)$
$\phi_{3/4}$	downwash angle at 3/4 spanwise station, rad
ψ	hub orientation, rad
ω	hub speed perturbation, $\omega = \dot{\psi} - \Omega$, rad/s
Ω	hub speed average, rad/s

Chapter 1

Introduction

Unmanned aerial vehicles (UAV) promise to enable a wide range of new robotic activities and services for both professional and private use. In the past, unmanned aircraft have been associated most closely with military surveillance roles. UAV were envisioned to be fielded with extensive ground control support, flown by expert remote operators, and used in preplanned, high altitude missions similar to those that might be flown by manned aircraft. In contrast, micro aerial vehicles (MAV) today are applied to a wide variety of tasks by an equally diverse set of users including civilian professionals, researchers, and enthusiasts. New applications include cinematography, live event videography, disaster relief support, and post-damage assessments. When equipped with new remote sensing payloads, MAV can support precision agriculture with spatially and temporally granular data about plant and soil fitness. Autonomous networks of unmanned vehicles are imagined as an alternative to static infrastructure including security camera networks or wireless communication services. Flight in close quarters or near buildings enables remote structural health assessment of bridges and dams. Similar capabilities would be required for last-mile package delivery, where vehicles with a high level of autonomy will need to be operated with confidence in public spaces.

With these new users and applications, operational expectations for MAV are changing. Future MAV must be cost competitive in these new applications. They must be portable, easily deployed, simple to service, and mechanically robust. Flight durations must be extended to meet user expectations. Operational safety becomes paramount as these devices are put into service near humans and buildings, in dynamic environments, and by non-specialist personnel.

These needs have put pressure on MAV to becomes increasingly small and light weight. Thankfully, improvements in the underlying technology including battery power density, strategic use of composite materials, MEMS inertial sensors, and miniaturized digital cameras and computation have supported this trend. In many respects, however, the commodification of MAV technology has not reduced either the fundamental complexity or the delicacy of performance devices. The continuing integration of new technologies is only slowly steering the design of these platforms away from simply being "aircraft in miniature." Significant departures from large scale fixed and rotary wing formats are possible.

Obtaining the required attitude control authority for highly dynamic maneuvers and outdoor operation in micro air vehicles is a significant challenge in light of their stringent form factor and system weight requirements. This dissertation considers how MAV may be endowed with cyclic blade pitch control such that thrust, roll, and pitch authority can all be obtained from a single rotor and a single motor. Cyclic pitch systems which use auxiliary roll and pitch actuators to drive a kinematic swashplate and linkage system remain the state of the art for agile helicopters at large and medium scales. Obtaining this kind of control authority without the gross weight, expense, assembly complexity, and maintenance issues inextricably linked to the swashplate enables new viable aircraft formats, capabilities, and operating scales.

Much of the technical content of this dissertation has been published by the author [60], [61], [64], [65] and publicly exhibited [63]. These publications are specifically referenced where excerpted in the following chapters.

Chapter 2 provides an overview of attitude control strategies for MAV in the literature with a special emphasis on cyclic blade pitch technologies. We present a general description of swashplate cyclic systems along with the challenges that have accompanied their practice at small scale. Multirotor aircraft are introduced as the most prolific alternative technology. Finally, a series of conceptual designs directly related to this work are described which seek cyclic control by manipulating flexible rotors with unsteady motor torques.

Chapter 3 introduces the theory of operation and basic kinematic design for the proposed rotor system. It derives a dynamical model governing the lag, pitch, and flap response of the rotor. The unique inclusion of hub speed variations and lag-pitch coupling explains the dynamical link between applied cyclic motor voltages and obtained cyclic blade pitch. Consideration of inertial effects, aerodynamic forces, hinge friction, and motor dynamics together permit accurate predictions of rotor performance as a function of basic design parameters.

Rotor experiments on a fixed test stand are described in Chapter 4. We present new techniques for measuring the hub speed, lag angle, blade pitch, and flap angle throughout each revolution of the rotor which are easily applied to the small, fast rotors central to future NAV research. The model predictions of the response amplitude and relative phase are in good agreement with measurement.

Chapter 5 considers how this technology may be applied to both very large and very small rotorcraft. Experiments with a 10 cm and 100 cm diameter rotor validate the extrapolation of test and modeling results from one scale to another. We also discuss technology and failure analysis considerations unique to manned aircraft.

Conventional attitude tracking flight capabilities using the rotor are demonstrated in Chapter 6. System integration and free flight testing are reported for both a 227 g experimental aircraft and a 28 g proof of concept vehicle, both of which rely entirely on underactuated cyclic control for flight authority. The larger aircraft demonstrates conventional trajectory tracking capabilities, and it illustrates that near-hover power consumption can be improved by reducing actuator weight even while expending the electrical power required for torque modulation. One version of the smaller aircraft incorporates a flexible single-piece rotor fabricated using an overmolding process. This proof of concept vehicle shows how the existing mass manufacturing capabilities for today's cheapest toy aircraft can be leveraged to produce sophisticated MAV systems by incorporating dynamic cyclic rotor control.

Chapter 7 demonstrates how the capabilities of a fully actuated MAV can now be emulated using only two actuators. In contrast, quadrotors exemplify underactuated dynamics. A quadrotor's thrust vector is fixed upward in the vehicle's body frame and so the only way to maneuver spatially is by constantly reorienting the vehicle attitude. Those rare aircraft capable of controlling both orientation and position are sometimes described as holonomic or omnidirectional, and all previous embodiments of this capability require at least six rotors or other ancillary actuators. In contrast, we demonstrate how two dynamic cyclic rotors can achieve simultaneous control over forces and moments. The resulting aircraft governs both orientation and position in six coordinates using a total of only two actuators. This represents a significant savings in weight and complexity for aircraft capable of stabilizing a camera independent of flight maneuvers or applying contact forces and torques to the environment.

Additional unusual aircraft formats made possible with the rotor are described in Chapter 8. Previously studied single-motor flying vehicles can now be endowed with position control in space. Alternatively, a flying wing with vertical takeoff and landing capabilities can rely entirely on two rotors for control, without requiring an excess of rotors or gimbal systems. Obtaining sophisticated flight behaviors from simple one and two actuator aircraft is a step towards re-imagining MAV as low cost and zero maintenance tools for general use.

Chapter 9 closes by briefly reviewing the primary contributions of this work as well as new application and research areas enabled by exploiting the underactuated cyclic principle.

Chapter 2

Background and Related Work

Many tasks for micro air vehicles (MAV) require the ability to hover in place with zero forward speed, or the capability to land and then take off from a point perch on a structure or on the ground. These are described as vertical take-off and landing (VTOL) or vertical flight capabilities, and are typified by full scale aircraft such as conventional helicopters and tiltrotor airplanes. MAV operate in a six-dimensional workspace. Casual operators expect them to govern both their three-dimensional spatial position in the air as well as their roll, pitch, and yaw body orientation. In practice, aircraft are often actuated with authority only over thrust force and roll, pitch, and yaw moments. While the resulting underactuated system can not simultaneously maintain arbitrary orientations and positions in space, backstepping controllers can allow them to spatially maneuver while maintaining heading and stabilizing their attitude dynamics.

Nearly without exception, the VTOL MAV in service today all employ spinning propellers to generate thrust. The radical diversity in design for these aircraft reflects the varied techniques and added actuators necessary to obtain maneuvering control over vehicle attitude.

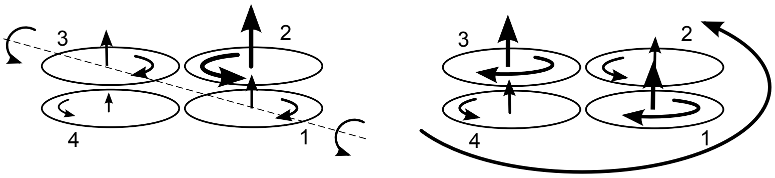

Figure 2.1: Quadrotor control moments generated by differential lift and drag.

2.1 Quadrotor and Multirotor MAV

A direct approach to control multiple degrees of freedom is to use multiple simple rigid rotors distributed about the airframe. Quadrotors and multirotors operate on this principle. With at least four independent rotors in an appropriate arrangement, linear combinations of the thrust from each rotor can affect simultaneous arbitrary thrust, roll, pitch, and yaw actuation.

A typical quadrotor employs four similar rotors arranged symmetrically about the body and collocated in the plane, as illustrated in Fig. 2.1. The two opposing pairs of rotors are matched sets, one pair spinning clockwise and the other pair counterclockwise. The net thrust of the four rotors generates lift, and simple combinations of controls to the four rotors can produce general moments about the body axes. Increasing the speed of the clockwise set of rotors while decreasing the speed of the counterclockwise set generates a yaw moment due to drag imbalance without exciting a roll response. Similarly, increasing the speed of one member of a pair while appropriately decreasing the speed of its mate generates a roll moment about the perpendicular axis without exciting a yaw response. In both cases, the net thrust can remain unchanged.

We can identify a linear, invertible transformation from the four individual rotor thrusts to the four net thrust, roll, pitch, and yaw commands. The thrust F_j and drag moment magnitude D_j of each propeller j are determined by its rotational speed Ω_j through the relations $F_j = k_F \Omega_j^2$ and $D_j = k_D \Omega_j^2$ [73]. If propellers are located a radius L from the center of mass with propellers 1 and 3 on the body fixed x-axis and propellers 2 and 4 on the body fixed y-axis, then the three moments about body fixed axes and the net force along the body-fixed z-axis can be computed from a matrix product with the vector of rotor thrusts [73] or a vector related to rotor speeds [48] as shown in Eq. 2.1.

$$\begin{bmatrix} F \\ m_x \\ m_y \\ m_z \end{bmatrix} = \begin{bmatrix} k_F & k_F & k_F & k_F \\ 0 & k_F L & 0 & -k_F L \\ -k_F L & 0 & k_F L & 0 \\ k_D & -k_D & k_D & -k_D \end{bmatrix} \begin{bmatrix} \Omega_1^2 \\ \Omega_2^2 \\ \Omega_3^2 \\ \Omega_4^2 \end{bmatrix} \tag{2.1}$$

This matrix is invertible, yielding the explicit formula 2.2 for choosing Ω_j to achieve a general lift force and moment $[F, m_x, m_y, m_z]^T$, subject to actuator constraints.

$$\begin{bmatrix} \Omega_1^2 \\ \Omega_2^2 \\ \Omega_3^2 \\ \Omega_4^2 \end{bmatrix} = \begin{bmatrix} \frac{1}{4k_F} & 0 & \frac{-1}{2k_F L} & \frac{1}{4k_D} \\ \frac{1}{4k_F} & \frac{1}{2k_F L} & 0 & \frac{-1}{4k_D} \\ \frac{1}{4k_F} & 0 & \frac{1}{2k_F L} & \frac{1}{4k_D} \\ \frac{1}{4k_F} & \frac{-1}{2k_F L} & 0 & \frac{-1}{4k_D} \end{bmatrix} \begin{bmatrix} F \\ m_x \\ m_y \\ m_z \end{bmatrix} \tag{2.2}$$

Through combinations of inputs the quadrotor utilizes four identical actuators in the mixed roll of thrust and control. Multirotor aircraft with more than four rotors in a redundant configuration may be controlled similarly.

Multirotor platforms have recently been embraced as a pragmatic alternative to pod and boom helicopters, particularly for sub-kilogram UAV. The rapid adoption of quadrotors could be viewed as a reaction to many factors, among them the design and maintenance complexity of good swashplate helicopter systems at this scale. What is more certain is that the catalyzing technologies were the advent of cheap inertial measurement systems (IMU) employing micro electromechanical systems (MEMS) and cheap on board computation. By relying entirely on electronic attitude control and stabilization, quadrotors dispense with the passive stability mechanisms such as stabilizer bars frequently used in coaxial MAV and NAV. Simultaneously, quadrotors eliminate the need for a swashplate control mechanism by employing four simple, rigid rotors working in concert.

The quadrotor has become a standard platform within the robotics research community. Its design, manufacture and maintenance are exceptionally simple, so much so that operational aircraft have been folded as kirigami [46] and tiny quadrotors can be made resilient to all manner of collisions with each other and the environment [51]. Its behavior is described well by simple dynamical models, making it an appealing subject system for controls research [9], trajectory planning [48], and multi-robot systems problems [84].

This simplicity does not reduce the number of actuators needed to fly, however, and increased power consumption may be associated with the added structure required to hold four distributed rotors and the increased mass associated with segmentation of the power plant and functional rotor disk. This has inspired new multirotor formats such as the triangular quadrotor of [19], [20] where a single central rotor provides the majority of the thrust and smaller rotors about the periphery are responsible for attitude control. In other work, pitch control has been added to the quadrotor's propellers in order to maintain optimum aerodynamic angle of attack over a range of climb rates or improve the dynamic thrust response of the rotors [13], [14]. Other extensions to the basic multirotor concept include introducing teetering instead of rigid hubs [72], controlling on estimated aerodynamic power instead of blade speed [4], and considering control in the case of actuator failure [50]. When six or more rotors are used in a non-redundant configuration, aircraft can be fully actuated near hover with control over both the net aerodynamic force vector and body moments [8], [31].

2.2 Control Surfaces and Gimbaled Actuators

While cyclic blade pitch control and multirotor systems together make up the vast majority of fielded micro air vehicles with vertical takeoff capabilities, the perceived complexity, performance, and efficiency tradeoffs of each have motivated continued work on the attitude control problem. A broad array of aircraft control systems have been investigated and deployed in the literature. Many of these can be broadly described as thrust vectoring strategies. These aircraft manipulate the direction of the thrust force with respect to the aircraft body or center of mass, in contrast to multirotor aircraft which maintain a thrust force fixed nominally upwards in the body frame at all times. This thrust vectoring may be accomplished by the use of servo-actuated vanes in the downwash of rigidly mounted motors [10]. Alternatively, motors and propellers can be mounted on actuated gimbals which allow the entire rotor assembly and resulting thrust forces to be pointed in arbitrary directions [42], [75]. Servo-controlled vanes and gimbaled motor assemblies can also be combined in a complementary way [55]. Very light and flexible MAV have been designed which use active deformations of their structure to reorient their thrust [78]. As an alternative to vectoring the aerodynamic thrust force, aircraft can manipulate the location of their center of mass and obtain net pitching moments from the balance of gravitational and aerodynamic forces [5]. All of these systems rely on adding extra actuated degrees of freedom in order to control vehicle attitude.

2.3 Cyclic Blade Pitch Control

Conventional pod and boom helicopters with cyclic control are the workhorse aircraft of manned vertical takeoff and landing (VTOL) flight. These aircraft typically have one main power plant and lifting rotor along with a separate tail rotor to control yaw and two separate servo actuators to control moments in pitch and roll. Unmanned helicopters of this style such as Arthur Young's 1941 model have been flown nearly as long as their manned counterparts (albeit manually piloted through wired connections) [77]. As a mature technology, some of the earliest autonomous VTOL aircraft have been of this type [32]. Such aircraft with rotor diameters of approximately one meter can be astonishingly agile in the hands of expert pilots or autonomous control [1]. In spite of the numerous technology alternatives, pod and boom helicopters continue to remain a popular research aircraft in robotics, particularly for outdoor work in grasping and manipulation [36], [71]. A slight modification of the traditional helicopter is to forgo the tail rotor in favor of two counter-rotating, coaxial main rotors. This format has been favor for some extremely small scale craft, most notably for the European muFly project [6] and the DARPA Nano Air Vehicle (NAV) program [80].

In both single-rotor and coaxial helicopter formats the aerodynamic control moments about pitch and roll are generated by actively changing the pitch of the rotor blade as it

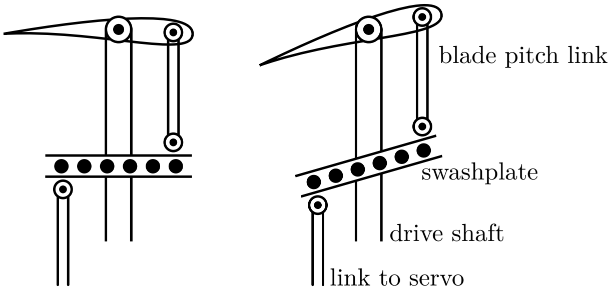

Figure 2.2: Schematic drawing of swashplate.

rotates through the use of auxiliary servos. Varying angle of attack, locked in phase with the rotor rotation, results in an asymmetric distribution of lift across the effective rotor disk. The resulting net moment and force reactions on the hub are transmitted to the helicopter body and used for attitude control. The amount of cyclic blade pitch variation and its phasing relative to the body of the helicopter is usually controlled by dedicated roll and pitch servos through a swashplate linkage. This complex mechanical linkage allows steady set points from relatively low bandwidth actuators in the vehicle's non-rotating frame to control high frequency cyclic pitch oscillations in the rotating hub frame.

There are many variations on the implementation of cyclic control with a swashplate, but a simple conceptual example is given in Fig. 2.2. The bottom rotor pivots on a feathering hinge and its pitch can be manipulated by a blade pitch link running down to the swashplate. As the rotor spins this pitch link follows the swashplate. This means that if the swashplate plane is held at a tilted angle, the blade pitch will rise and fall on each revolution of the rotor head. The motion of the swashplate is controlled from below by more linkages to servomotor actuators – typically two servos are used to control roll and pitch in fixed collective helicopters.

Small scale coaxial helicopters frequently employ an active swashplate system on the lower rotor and incorporate a separate passive linkage system into the upper rotor to improve dynamic stability. In such cases the upper rotor likewise pivots about a feather hinge, but its blade pitch is controlled by a linkage up to a stabilizer bar. This passive mechanism augments the overall vehicle rate damping, which can both make the vehicle easier to fly by a human pilot and reduce the bandwidth requirements on the swashplate servo system required for stability.

The relationship between the rotational phase of the blade pitch change and the net direction of hub forces or moments obtained is the combined result of aerodynamics, inertial properties, and structural stiffness. Two extreme examples are illustrated in Fig. 2.3. Supposing we imagine a perfectly rigid blade, rigidly affixed to the hub in flap. It will be the case that the cyclic blade pitch, aerodynamic lift, and hub reaction torque all peak simultaneously. As a result, maximum blade pitch should be obtained as the blade crosses the nose of the aircraft in order to obtain a net pitching moment on the vehicle. In contrast, some helicopter blades are free to flap up and down either on a central teetering hinge or articulated on flap hinges located very close to the center of rotation. For these systems, cyclic blade pitch at the rotor frequency excites a flapping blade response very close to resonance, such that the flapping response is approximately 90° out of phase with the driving cyclic input. In this case, maximum pitch must be obtained 90° in advance of the rotor crossing the aircraft nose in order to obtain a pure pitching effect. Most rotor systems lie somewhere in between these extremes, including the swashplateless systems described in this work. This pitching and flapping character is common to all cyclic systems no matter how blade pitch changes are actually obtained, and the details of the rotor flapping response will be of particular interest in Chapter 4.

A typical implementation of a swashplate and stabilizer bar system is shown in Fig. 2.4 and Fig. 2.5 for the Blade CX2 toy helicopter, which follows the simplest of swashplate systems illustrated earlier in Fig. 2.2. This aircraft has been used in the literature as both a object of study for system identification [15] and as a practical aerial platform for vision and controls research [26]. The large number of components and bearing surfaces shown present assembly, maintenance, and cost engineering challenges particularly as smaller and smaller MAV are desired. In full size aircraft, a study of helicopter accidents ascribed 33 % to mechanical failure [11], and while only a small fraction of these involved the swashplate itself the problem of developing fault tolerant cyclic systems has received attention from

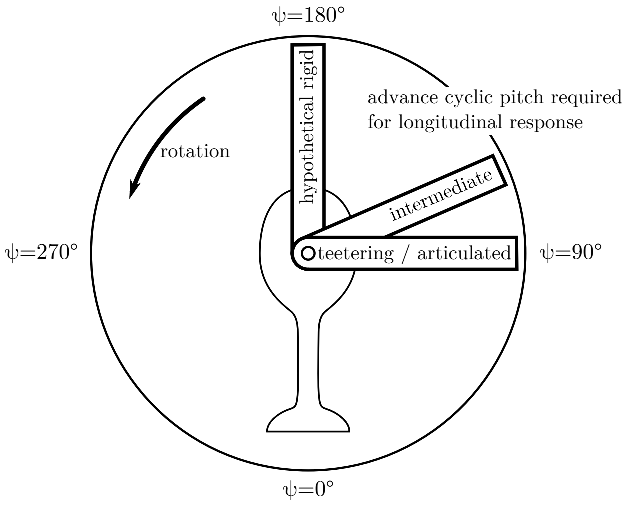
ψ=180°
hypothetical rigid
advance cyclic pitch required
for longitudinal response
rotation
intermediate
ψ=270°
teetering / articulated
ψ=90°
ψ=0°

Figure 2.3: Azimuthal location of maximum cyclic blade pitch in order to obtain a pure aircraft pitching response. Adapted from [15].

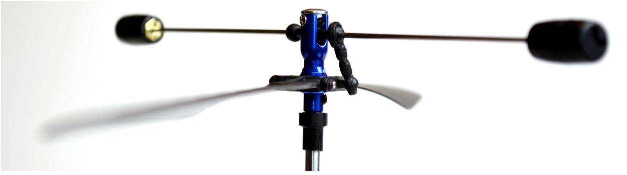

Figure 2.4: Stabilizer bar for the upper rotor of the Blade CX2 coaxial helicopter.

both a mechanical design [85] and control design [27] perspective.

Several efforts have been made to adapt swashplate-like cyclic pitch control to MAV and NAV, where the conventional bulk of a full mechanical swashplate and electromechanical servomotor actuators can be prohibitive. The muFly coaxial helicopter program proposed combining a simplified conventional swashplate with piezoelectric actuators instead of electromechanical servomotors[79], [80]. The Draper NAV program developed a tilting motor

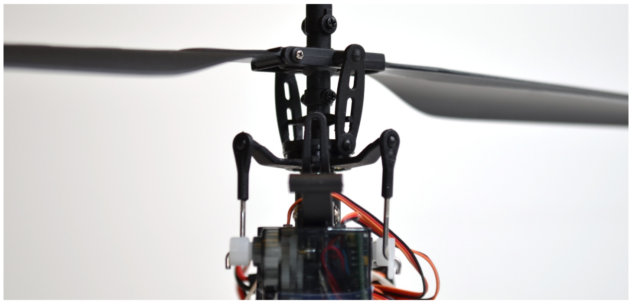

Figure 2.5: Swashplate for the lower rotor of the Blade CX2 coaxial helicopter.

concept which again employed piezoelectric actuators but avoided the need for linkage rods in the rotating head itself [25]. In spite of these advances, integrating these control structures into actual free flight vehicles remains a challenge.

2.4 Torque Modulating Cyclic Control

In large aerial vehicles cyclic pitch control allows for a strict dichotomy between thrust and control generating actuators. This permits the separate optimization of high power lifting engines with slow response times and low power servo control actuators with fast response times. Quadrotors show this to be an unnecessary distinction, at least for modern electronic motors and drives. However, quadrotors continue to use four motors to control vehicle thrust and attitude just as helicopters use four actuators to drive a main rotor, tail rotor, pitch cyclic axis, and roll cyclic axis. Our interest is in obtaining both thrust and attitude authority from a single rotor as in a cyclic control helicopter but without adding auxiliary actuators of any kind. Several concepts have been put forward which work on the premise that the main motor can maintain an average rotor speed and thrust while simultaneously modulating the applied torque to excite some desired once-per-revolution action on the rotor blade and affect attitude control.

One such technique is taught by a 1992 patent assigned to the Keyence Corporation describing the operation of the Revolutor H-610 toy helicopter, shown in Fig. 2.6. A single rigid rotor consisting of two blades is free to pivot about the feathering axis, such that if one blade's angle of attack is increased the other's will be depressed. Instead of being driven from a central shaft, the rotor is pulled forward by a cantilever spring which tugs on one of the blade roots. This linkage is designed such that an increase to the driving torque twists the attached blade to a higher pitch and a decrease relaxes the blade to a lower pitch. High frequency pulses in the motor torque at the rotational rate induce once-per-revolution oscillations in blade pitch, mimicking conventional cyclic control.

The Revolutor H-610 was one of the smallest helicopter platforms of its time and has been employed as a platform in research related to reinforcement learning [53] and optic

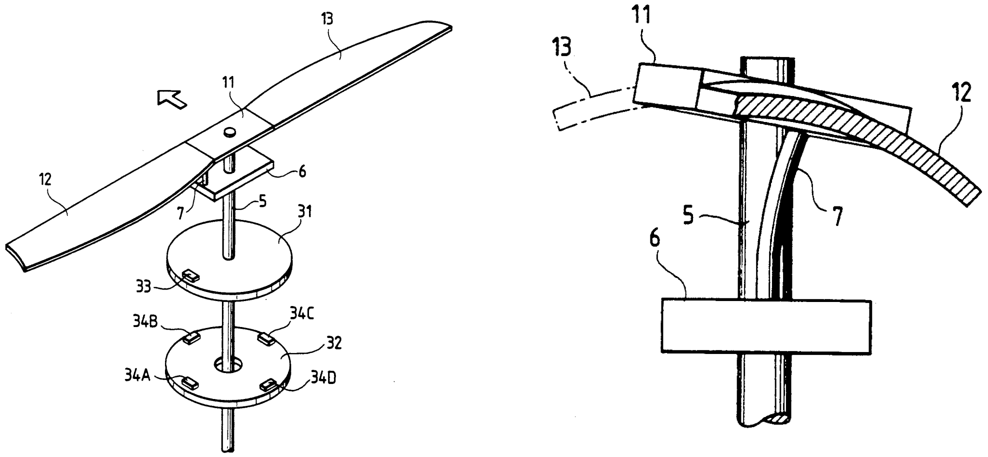

(a) Propeller 11 spins freely on shaft 5 and is driven indirectly through linkage 7 to drive plate 6.

(b) A torque at drive plate 6 bends linkage 7, resulting in increased angle of attack at 12 and decreased angle of attack at 13.

Figure 2.6: US patent figures for the Keyence Corporation Revolutor model helicopter [74].

flow [76]. In spite of this, the unique dynamics of the Keyence control system has not been specifically explored. One common treatment is to view these dynamics as a black box that transfers control signals to cyclic variation, at which point standard helicopter model approximations may be applied. A relatively detailed description of the Keyence mechanism and aircraft may be found [24], but even here the rotor control dynamics are not explicitly modeled or experimentally investigated.

The Keyence design is one path to a minimally actuated MAV that can express the full control authority of a standard helicopter without requiring the auxiliary actuators of a swashplate or the numerous rotors of a quadrotor. However, this realization still retains much of the mechanical complexity of a swashplate, including the need to support the propeller free to feather about the long axis and the exacting geometry of the flexible linkage between the motor drive plate and propeller. A later patent by Reich [18] describes conceptually how a hinged blade such as in Fig. 2.7 could respond directly to change in torque with changes in blade pitch. It is not reported if such a device was ever constructed and no mathematical model of the dynamics at work, simulation results, or experimental study are available. Nevertheless, the inspiration is the same as that of the designs described in the next chapter

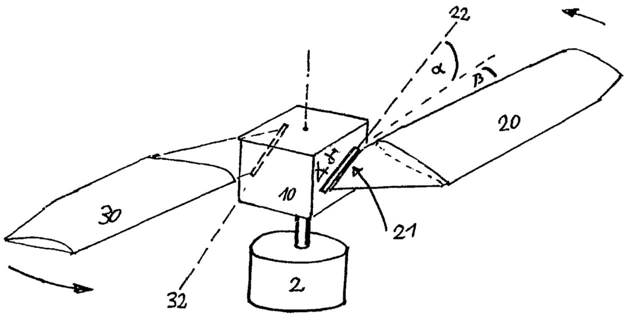

Figure 2.7: German patent figure shows concept for attitude control with a hinged propeller [18].

and followed through to detailed modeling, rotor experiments, and flying testbeds in this work.

Chapter 3

Design and Modeling

3.1 Basic Operating Principle

In this work we directly induce a controlled cyclic response in blade pitch by modulating the main drive motor already present. The initial design is shown in Fig. 3.1 where two blades are attached to the rotor hub by simple pin hinges at a small radius from the center of rotation. Crucially, the lines of these hinges are not vertical, as is typically found in the lead-lag hinges of a conventional helicopter. Instead, the top of the "positive" blade's hinge is inclined inward, and the top of the "negative" blade's hinge is inclined outward. This geometry couples the lead-lag motion of the blade tip about the central shaft to a pitching motion about the blade long axis, as depicted in Fig. 3.2.

The objective of the cyclic system is to induce an elevated blade pitch as the blades

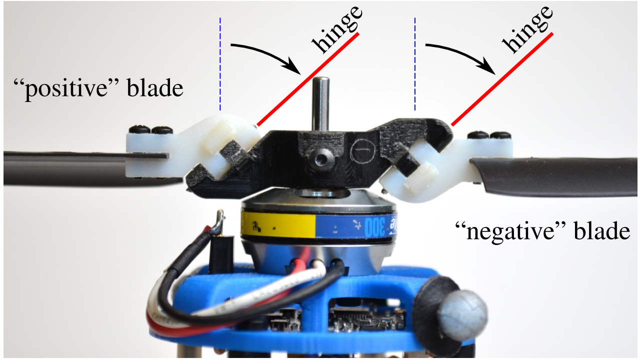

Figure 3.1: Two blades are attached by canted hinges to a hub directly affixed to the main motor.

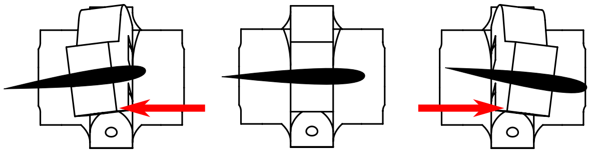

Figure 3.2: As the positive blade lags backwards, the pitch increases. As it leads forward, the pitch decreases.

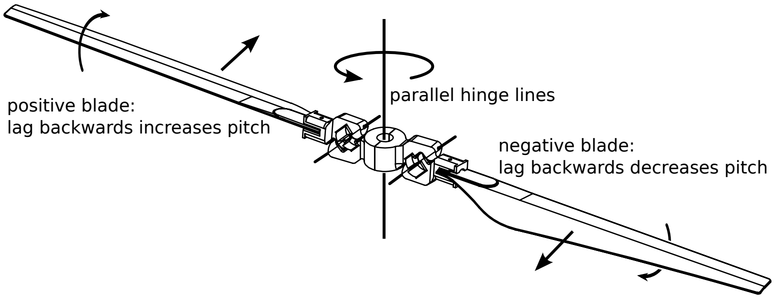

Figure 3.3: Positive and negative blades respond 180° out of phase with each other.

pass some station of the rotor disk and a depressed blade pitch as the blades pass 180° opposite. To this end, we modulate the torque applied to the motor by adding a sinusoidal component in phase with the motor rotation, exciting once per revolution variations in lag angle and therefore also in pitch. As the hub accelerates forwards the positive blade tip lags backwards relative to the hub and the kinematics require the pitch of the blade tip to increase. At the opposite station, 180° later, the positive blade tip now leads forwards relative to the hub and the pitch of the blade is instead depressed. The complementary geometry of the negative blade as show in Fig. 3.3 yields the opposite response, so that an appropriate input can induce both blades to, for example, elevate pitch while passing across the nose and decrease pitch while passing across the tail of the aircraft. Such smooth oscillation through every revolution bears a strong resemblance to conventional cyclic pitch control, but it is now achieved merely by electronically altering the amplitude and phase offset angle of the sinusoidal drive component.

Figure 3.1 is a very direct embodiment of the desired lag-pitch coupling, and the flight results described in Chapter 6 were obtained using precisely this type of rotor. However, this particular design presents difficulties for both aircraft integration and accurate modeling. If the blades are understood to be rigid, then the kinematics dictate that the blade tips flap up and down twice per revolution as the lag angle and blade pitch oscillate once per revolution. This unusual flapping behavior should induce unwanted higher harmonic forces on the hub, and may be responsible for the large vibrations in the landing gear visible in high speed videos of these aircraft. That said, it is plainly unrealistic to model these blades as rigid structures. Strobe photography shows that the blades flex in flight and the true flapping response is actually somewhere in between a conventional helicopter first harmonic flapping and the undesirable second harmonic rigid beats. The refined design described next resolves both these issues. It will be the primary subject of the rotor modeling effort in this chapter and the test stand experiments in Chapter 4 which have previously been reported by the author in [64]

3.2 Design and Kinematics

The updated design kinematically induces a lag-pitch coupling through the combination of a conventional flap hinge and a skewed lag-pitch hinge. Similar hinge kinematics are depicted by Bousman [7] in the study of dynamic blade stability; now we exploit this structure as part of the control effector design. Figure 3.4 illustrates the physical device consisting of the hub, cross, blade grip, and blade bodies. On the right side of the figure the hub is attached to the cross by a flap hinge pin joint. The cross connects to the blade grip by a skewed lag hinge pin joint.

The simplified kinematics are depicted in Fig. 3.5 with respect to a rotating hub-fixed coordinate system with unit vectors $\{\hat{\mathbf{x}}, \hat{\mathbf{y}}, \hat{\mathbf{z}}\}$. The kinematics and coordinate conventions for the positive lag-pitch coupling blade are shown on the right side of the figure. The hub

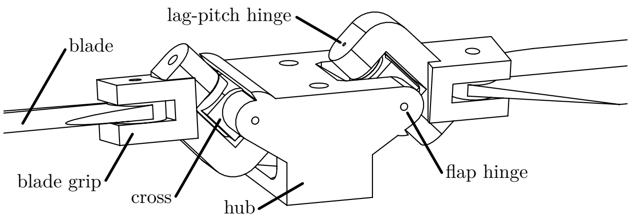

Figure 3.4: Serial flap and lag hinges resemble a skewed universal joint. The the hub and blade grip are connected by an intermediate cross which carries the pin joints.

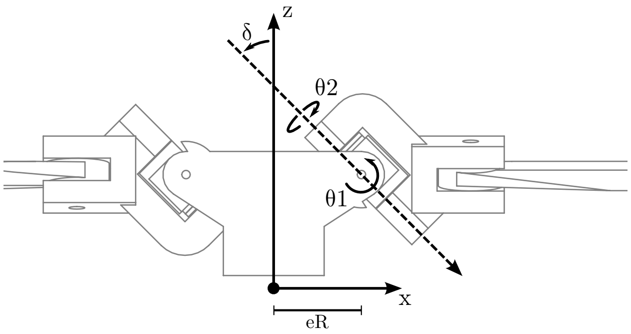

Figure 3.5: The flap and lag-pitch hinges are approximately co-located at radius eR. In the reference pose the lag-pitch axis is skewed by angle δ from vertical.

rotates about the $\hat{\mathbf{z}}$ axis by angle ψ with respect to an inertial frame. The inboard flap hinge axis is fixed in the hub body and joins the cross body. The flap hinge rotates by an angle θ_1 about an axis pointed in the $-\hat{\mathbf{y}}$ direction. The cross carries the skewed lag hinge axis and joins to the blade. The lag hinge axis of rotation is inclined by an angle δ from vertical to point in the $\sin(\delta)\hat{x} - \cos(\delta)\hat{\mathbf{z}}$ direction, and the hinge rotates by an angle θ_2. The flap hinge and lag hinge are collocated at radius eR for blade tip radius R and eccentricity $0 < e < 1$.

We would like to make a precise analogy between the actual kinematics of Fig. 3.5 and the conventional parameterization of blade motions in terms of orthogonal lag and flap axes typical to the helicopter literature [41]. To do this, we consider small deflections of the blade about its physical hinges. Under both axes conventions the rigid body motion of the blade is a pure rotation about the point at eR, so it is sufficient to show that both parameterizations describe equivalent rotations.

The composite rotation about first and second axes is conveniently described by exponential coordinates (or an axis and angle representation) when the rotations are infinitesimal. A finite rotation by angle θ_1 about an axis with unit vector $\boldsymbol{\omega}_1$ is described by the rotation matrix $\exp(\hat{\boldsymbol{\omega}}_1\theta_1)$ where $\hat{\boldsymbol{\omega}}_1$ is the skew symmetric matrix defined such that $\boldsymbol{\omega}_1 \times \mathbf{b} = \hat{\boldsymbol{\omega}}_1\mathbf{b}$ for all $\mathbf{b}$. For the case of an infinitesimal rotation size $d\theta_1$, then to a first order approximation $\exp(\hat{\boldsymbol{\omega}}_1\theta_1) = I + \hat{\boldsymbol{\omega}}_1\, d\theta_1$. It follows that the composite rotation about axis $\boldsymbol{\omega}_1$ by angle $d\theta_1$ and then about axis $\boldsymbol{\omega}_2$ by angle $d\theta_2$ is $\exp(\hat{\boldsymbol{\omega}}_2\, d\theta_2)\exp(\hat{\boldsymbol{\omega}}_1\, d\theta_1) = I + (\boldsymbol{\omega}_1\, d\theta_1 + \boldsymbol{\omega}_2\, d\theta_2)^{\wedge}$ to a first order approximation. A physical interpretation of this result is simply that infinitesimal

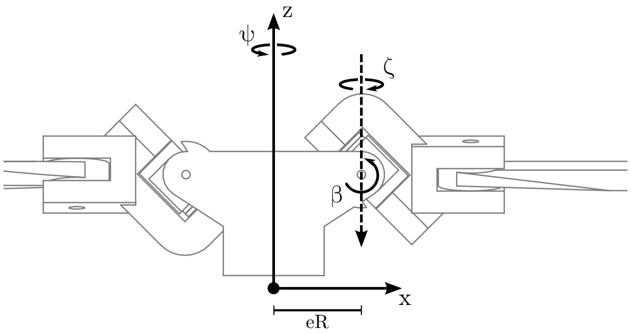

Figure 3.6: For analysis, the kinematics are approximated by conventional flap angle β and lag angle ζ about orthogonal axis vectors fixed in the rotating hub frame. A lag-pitch coupling coefficient is imposed separately.

rotations commute, or that angular velocity vectors add. The exponential coordinates for the composite rotation dictated by the design geometry of Fig. 3.5 is given by Eq. 3.1.

$$\begin{bmatrix} 0 \\ -1 \\ 0 \end{bmatrix} d\theta_1 + \begin{bmatrix} \sin(\delta) \\ 0 \\ -\cos(\delta) \end{bmatrix} d\theta_2 \tag{3.1}$$

For analysis, we re-parameterize the motion in terms of the canonical flap angle β about an axis in the $-\hat{\mathbf{y}}$ direction and lag angle ζ about the $-\hat{\mathbf{z}}$ direction, both axes fixed in the hub frame. This arrangement is shown in Fig. 3.6. We separately impose a geometric lag-pitch coupling coefficient $\Delta\theta/\Delta\zeta = \tan(\delta)$ and the resulting exponential coordinates for the composite rotation are given in Eq. 3.2.

$$\begin{bmatrix} 0 \\ -1 \\ 0 \end{bmatrix} d\beta + \begin{bmatrix} \Delta\theta/\Delta\zeta \\ 0 \\ -1 \end{bmatrix} d\zeta \tag{3.2}$$

The reparameterized expression in Eq. 3.2 encodes identical kinematics constraints as Eq. 3.1 for the blade rotation. Both formulations describe the rigid body motion of the blade as a pure rigid body rotation about the point at radius eR, so identical rotations indicate identical rigid body motions. The derived equation of motion, linearized for small deflections, will be equivalent if the flap and lag axes are coincident at eccentricity e and the rotational inertial of the small cross body and the blade about the pitch axis is neglected. This simplified parameterization in terms of the hub angle ψ, upward flap angle β, retrograde lag angle ζ, and geometric lag-pitch coupling coefficient $\Delta\theta/\Delta\zeta = \tan(\delta)$ will be used in the remainder.

This identical result can be shown by parameterizing the kinematics using twists and applying the product of exponentials formula [54] for manipulator forward kinematics. We define a blade frame with origin at the point eR and consider its motion relative to the reference configuration pose. The forward kinematics map with respect to the reference configuration can be computed in homogeneous coordinates as $e^{\hat{\boldsymbol{\xi}}_1\theta_1}e^{\hat{\boldsymbol{\xi}}_2\theta_2}$. Twist $\boldsymbol{\xi}_i$ is computed as $\boldsymbol{\xi}_i = (\mathbf{v}_i, \boldsymbol{\omega}_i) = (-\boldsymbol{\omega}_i \times \mathbf{p}_i, \boldsymbol{\omega}_i)$, having unit vector axis $\boldsymbol{\omega}_i$ and point on the axis $\mathbf{p}_i$ in the reference configuration. We have specified that in the reference configuration both axes intersect the origin, so the cross products are zero and the twists are all of form $\boldsymbol{\xi}_i = (0, \boldsymbol{\omega}_i)$.

In similarity to the previous analysis, the infinitesimal rigid body transformation to first order is given by $I + (\boldsymbol{\xi}_1\, d\theta_1 + \boldsymbol{\xi}_2\, d\theta_2)^\wedge$. The twist coordinates describing the infinitesimal rigid body transformation defined by Fig. 3.5 and Fig. 3.6 mirror the earlier result, and once again show the equivalence of the two different axes parameterizations.

$$\begin{bmatrix} 0 \\ 0 \\ 0 \\ 0 \\ -1 \\ 0 \end{bmatrix} d\theta_1 + \begin{bmatrix} 0 \\ 0 \\ 0 \\ \sin(\delta) \\ 0 \\ -\cos(\delta) \end{bmatrix} d\theta_2 \tag{3.3}$$

$$\begin{bmatrix} 0 \\ 0 \\ 0 \\ 0 \\ -1 \\ 0 \end{bmatrix} d\beta + \begin{bmatrix} 0 \\ 0 \\ 0 \\ \Delta\theta/\Delta\zeta \\ 0 \\ -1 \end{bmatrix} d\zeta \tag{3.4}$$

The use of twists highlights the impact of the hinge axes locations: the exact similitude between the skew axes and conventional orthogonal axes descriptors is only possible because we consider all axes to pass through the point at eR.

3.3 Dynamical Model

The dynamical model consists of a linearized, nondimensional equation of motion for the propeller incorporating hub and blade inertial effects, aerodynamic forces, hinge losses, and the motor dynamics. This chapter next considers each contribution in turn before constructing the final trim and perturbation equations in Sections 3.8–3.9 (Eqs. 3.50, 3.53, and 3.56). Instead of explicitly modeling two blades, the analysis is simplified by taking advantage of approximate symmetry and modeling only one blade and appropriately normalizing the hub inertia and motor torques by the number of blades. This derivation excerpts heavily from the author's work in [64].

3.4 Open-Chain Dynamics

The dynamics of the half propeller are developed as those of a three degree of freedom open-chain linkage with hub angle ψ, lag angle ζ, and flap angle β as defined in Fig. 3.6. The generic equation of motion is given by Eq. 3.5 where $\mathbf{q} = \{\psi, \zeta, \beta\}$, a general result for open-chain dynamical systems [54]. The inertial matrix $M(\mathbf{q})$ is a nonlinear function of the generalized coordinates and the Coriolis matrix $C(\mathbf{q}, \dot{\mathbf{q}})$ is a function of the coordinates and speeds. Both terms are derived directly from the kinematics depicted in Fig. 3.6 and inertial properties of the hub and blade body using the product of exponentials formula [54]. By convention, external (aerodynamic) forces applied to the rotor enter through $\boldsymbol{N}$ and joint torques from the motor and hinge losses enter on the right as $\boldsymbol{\tau}_{motor}$ and $\boldsymbol{\tau}_{hinge}$.

$$M(\mathbf{q})\ddot{\mathbf{q}} + C(\mathbf{q}, \dot{\mathbf{q}})\dot{\mathbf{q}} + \boldsymbol{N} = \frac{1}{N_b}\boldsymbol{\tau}_{motor} + \boldsymbol{\tau}_{hinge} \tag{3.5}$$

In anticipation of deriving a linearized governing equation, we identify a steady trim condition at rotor speed Ω with coordinates $\mathbf{q}_0$ and velocities $\dot{\mathbf{q}}_0$ given by Eq. 3.6. Steady drag forces will cause the blades to lag backwards by a small positive angle ζ_0 and lift forces will cause the blades to flap upwards by a small positive coning angle β_0.

$$\begin{aligned} \mathbf{q}_0 &= \{\Omega t, \zeta_0, \beta_0\} \\ \dot{\mathbf{q}}_0 &= \{\Omega, 0, 0\} \end{aligned} \tag{3.6}$$

The linearized equation will be written in terms of perturbation variables $\mathbf{x}$, $\dot{\mathbf{x}}$ relative to this equilibrium.

$$\begin{aligned} \mathbf{x} &= \mathbf{q} - \mathbf{q}_0 = \{\tilde{\psi}, \tilde{\zeta}, \tilde{\beta}\} \\ \dot{\mathbf{x}} &= \dot{\mathbf{q}} - \dot{\mathbf{q}}_0 = \{\omega, \dot{\zeta}, \dot{\beta}\} \end{aligned} \tag{3.7}$$

The inertial acceleration term is approximated using a constant inertia matrix M found by evaluating the inertial matrix in the trim configuration. The Coriolis product is replaced by an affine approximation including an effective stiffness coefficient matrix K_C, an effective gyroscopic coefficient G_C, and an additive constant term $\boldsymbol{C_0}$. For now the aerodynamic forces $\boldsymbol{N}$ and joint torques $\boldsymbol{\tau}_{motor}$, $\boldsymbol{\tau}_{hinge}$ are left as general functions and derived in the following sections.

$$M\ddot{\boldsymbol{x}} + G_C\dot{\boldsymbol{x}} + K_C\boldsymbol{x} + \boldsymbol{C_0} + \boldsymbol{N} = \frac{1}{N_b}\boldsymbol{\tau}_{motor} + \boldsymbol{\tau}_{hinge} \tag{3.8}$$

The coefficient matrices M, K_C, and G_C along with constant C_0 are primarily dependent

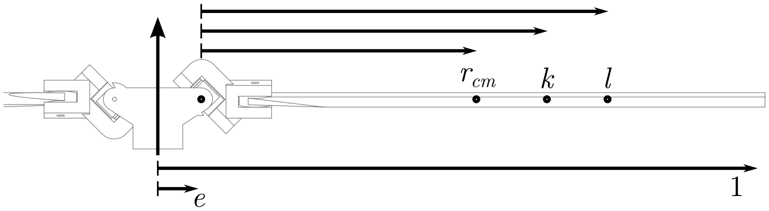

Figure 3.7: Center of mass r_{cm}, radius of gyration k, and center of oscillation l.

on the inertial properties of the hub and blade. A dimensional descriptor of the mass properties would be to specify the hub inertia I_h, blade mass m, location of the blade center of mass $r_{cm}R$, and blade inertia about the flap axis I_β. We assume a slender blade, so that the inertia about flap and lag axes are equal and the inertia about the longitudinal feather axis is negligible.

It will be convenient to describe the blade in terms of nondimensional parameters, normalized by the tip radius R and flap inertia I_β. The dimensionless hub inertia ratio X_{Ih} is the ratio of the hub inertia I_h to the flap inertia I_β and number of blades N_b. The blade mass distribution is represented by the radius of gyration k and radius of oscillation l from the hinge, each described as a fraction of the tip radius as shown in Fig. 3.7. The radius of gyration k defined in Eq. 3.10 identifies at what location a lump mass m would need to be placed in order to replicate inertia I_β. The center of oscillation l is defined in Eq. 3.11. For the classic compound pendulum, the center of oscillation identifies the equivalent simple pendulum length for equal period of oscillation.

$$X_{I_h} = \frac{I_h}{N_b I_\beta} \tag{3.9}$$

$$k^2 = \frac{I_\beta}{mR^2} \tag{3.10}$$

$$l = \frac{I_\beta}{r_{cm} m R^2} \tag{3.11}$$

Coefficients M, G_C, and K_C along with constant $\boldsymbol{C}_0$ are presented in Eq. 3.12-3.15. Their trigonometric dependence on the small constant trim lag and flap angles ζ_0 and β_0

have been approximated to first order by Taylor series expansion.

$$M = I_\beta \begin{bmatrix} 1 + X_{I_h} + 2\frac{e}{l} + \frac{e^2}{k^2} & -1 - \frac{e}{l} & 0 \\ -1 - \frac{e}{l} & 1 & 0 \\ 0 & 0 & 1 \end{bmatrix} \tag{3.12}$$

$$G_C = I_\beta \Omega \begin{bmatrix} 0 & -2\frac{e}{l}\zeta_0 & -2(1 + \frac{e}{l})\beta_0 \\ 2\frac{e}{l}\zeta_0 & 0 & 2\beta_0 \\ 2(1 + \frac{e}{l})\beta_0 & -2\beta_0 & 0 \end{bmatrix} \tag{3.13}$$

$$K_C = I_\beta \Omega^2 \begin{bmatrix} 0 & 0 & 0 \\ 0 & \frac{e}{l} & 0 \\ 0 & 0 & 1 + \frac{e}{l} \end{bmatrix} \tag{3.14}$$

$$\boldsymbol{C}_0 = I_\beta \Omega^2 \begin{bmatrix} 0 \\ \frac{e}{l}\zeta_0 \\ (1 + \frac{e}{l})\beta_0 \end{bmatrix} \tag{3.15}$$

In the special case of a blade with mass m uniformly distributed between the hinge at radius eR and the tip at radius R, the inertia I_β and mass distribution parameters k and l take on the values given in Eq. 3.16–3.18. With this simplification, Eq. 3.12–3.15 reduce to the form reported in [64].

$$I_\beta = \frac{1}{3}(1 - e)^2 m R^2 \tag{3.16}$$

$$k^2 = \frac{1}{3}(1 - e)^2 \tag{3.17}$$

$$l = \frac{2}{3}(1 - e) \tag{3.18}$$

3.5 Aerodynamic Forces

The generalized aerodynamic forces about the hub axis, lag axis, and flap axis are required to establish the external forces $\boldsymbol{N}$ in Eq. 3.8. These moments are developed by integrating the local section forces along the blade length. The differential section forces F_z in the vertical direction and F_y in the chord direction are developed from section lift and drag forces L, D and a small angle approximation on the inflow angle ϕ.

$$\begin{aligned} dF_z &= dL - \phi\, dD \\ dF_y &= -\phi\, dL - dD \end{aligned} \tag{3.19}$$

The local angle of attack $\alpha = \theta - \phi$ is the blade pitch angle θ less the local inflow angle ϕ. The inflow angle ϕ is determined from perpendicular and tangential local relative wind velocities U_P and U_T such that $\phi \simeq U_P/U_T$. The net incident wind speed U_∞ equates $U_\infty = \sqrt{U_P^2 + U_T^2}$. Lift and drag are determined from the section curve slope a and section drag coefficient c_{d_0}.

$$\begin{aligned} dL &= \frac{\rho a c}{2} U_\infty^2 (\theta - \frac{U_P}{U_T})\, dx \\ dD &= \frac{\rho c}{2} U_\infty^2 c_{d_0}\, dx \end{aligned} \tag{3.20}$$

The local velocities U_P and U_T are specialized for the case of a propeller with offset lag and flap hinges and hub with varying rotational speed $\dot{\psi} = \Omega + \omega$. Let v_i be the inflow velocity, $\Omega + \omega$ be the hub speed, β be the flap angle (positive up) and ζ be the lag angle (positive regressing). The local radius is ξR for tip radius R and nondimensional spanwise coordinate ξ with $0 \le \xi \le 1$, such that $dx = R\, d\xi$. The lag and flap hinges are located at a radius eR, offset from center by eccentricity e with $0 \le e \le 1$.

$$\begin{aligned} U_P &= v_i + R(\xi - e)\dot{\beta} \\ U_T &= R\xi(\Omega + \omega) - R(\xi - e)\dot{\zeta} \end{aligned} \tag{3.21}$$

The section differential forces at blade station ξ are obtained from Eqs. 3.19–3.21 upon substitution. Higher order products of small terms ω, $\dot{\zeta}$, and $\dot{\beta}$ are neglected.

$$\begin{aligned}
dF_z = \frac{\rho a c \Omega^2 R^3}{2} \Bigg\{ & -(1+\frac{c_{d0}}{a})\xi\frac{v_i}{\Omega R} + \theta\Big(\xi^2\Big) \\
& + \frac{\omega}{\Omega}\Big(2\theta\xi^2 - (1+\frac{c_{d0}}{a})\xi\frac{v_i}{\Omega R}\Big) \\
& - \frac{\dot{\zeta}}{\Omega}\Big(2\theta\xi(\xi-e) - (1+\frac{c_{d0}}{a})(\xi-e)\frac{v_i}{\Omega R}\Big) \\
& - \frac{\dot{\beta}}{\Omega}\Big((1+\frac{c_{d0}}{a})\xi(\xi-e)\Big)\Bigg\} d\xi
\end{aligned}$$

$$\begin{aligned}
dF_y = -\frac{\rho a c \Omega^2 R^3}{2} \Bigg\{ & \frac{c_{d0}}{a}\xi^2 - \frac{v_i^2}{\Omega^2 R^2} + \theta\Big(\xi\frac{v_i}{\Omega R}\Big) \\
& + \frac{\omega}{\Omega}\Big(2\frac{c_{d0}}{a}\xi^2 + \theta\xi\frac{v_i}{\Omega R}\Big) \\
& - \frac{\dot{\zeta}}{\Omega}\Big(2\frac{c_{d0}}{a}\xi(\xi-e) + \theta(\xi-e)\frac{v_i}{\Omega R}\Big) \\
& + \frac{\dot{\beta}}{\Omega}\Big(\theta\xi(\xi-e) - 2(\xi-e)\frac{v_i}{\Omega R}\Big)\Bigg\} d\xi
\end{aligned} \tag{3.22}$$

The hub, lag hinge, and flap hinge moments are obtained by integrating the differential forces along the blade length, neglecting the effect of the blade root cutout as well as tip loss.

$$\begin{aligned}
M_{\psi_{aero}} &= R\int_0^1 \xi\, dF_y \\
M_{\zeta_{aero}} &= -R\int_0^1 (\xi-e)\, dF_y \\
M_{\beta_{aero}} &= R\int_0^1 (\xi-e)\, dF_z
\end{aligned} \tag{3.23}$$

In undertaking this integral, station weighted averages of the local downwash angle $\phi_i = v_i/(\Omega R\xi)$ and square of the downwash angle appear. In Eq. 3.24 we define parameters A and C as developed in [58] and new analogous parameters B, D, E which are anticipated by the extension to offset lag and flap hinges in [7].

$$\begin{aligned}
A &= 4\int_0^1 \xi^3 \phi_i \, d\xi & A_{3/4} &= \phi_{3/4} \\
B &= 4\int_0^1 \xi^2 \phi_i \, d\xi & B_{3/4} &= \frac{4}{3}\phi_{3/4} \\
C &= 4\int_0^1 \xi^3 \phi_i^2 \, d\xi & C_{3/4} &= \phi_{3/4}^2 \\
D &= 4\int_0^1 \xi^2 \phi_i^2 \, d\xi & D_{3/4} &= \frac{4}{3}\phi_{3/4}^2 \\
E &= 4\int_0^1 \xi \phi_i \, d\xi & E_{3/4} &= 2\phi_{3/4}
\end{aligned} \tag{3.24}$$

The local downwash angle ϕ_i is determined from the local inflow velocity v_i, which may be calculated from blade element momentum theory within an annular ring at radius ξ. For the special case of a hovering rotor not in climb, Eq. 3.25 gives the inflow at blade station ξ as a function of solidity $\sigma = N_b c/(\pi R)$ [41].

$$\frac{v_i}{\Omega R} = \frac{a\sigma}{16}\left(\sqrt{1 + \frac{32\theta}{a\sigma}\xi} - 1\right) \tag{3.25}$$

In the remainder of the derivation, these integrals are approximated by evaluating them assuming uniform downwash angle ϕ_i equal to the value at the three-quarters station radius, $\phi_{3/4}$. The expression for $\phi_{3/4}$ in Eq. 3.26 has been used previously in [58]. An advantage of dealing in the downwash angle is that it is a nondimensional parameter independent of operating speed, unlike the inflow velocity itself. For the particular prototype described by Table 5.4 the calculated downwash angle is 4.4° while the inflow velocity varies from 0.9 m/s to 2.8 m/s at test speeds from 100 rad/s to 300 rad/s.

$$\phi_{3/4} = \frac{a\sigma}{12}\left(\sqrt{1 + \frac{24\theta_0}{a\sigma}} - 1\right) \tag{3.26}$$

The evaluated integrals for the full moments about the hub, lag, and flap axes are given in Eqs. 3.27–3.29, now written in terms of the Lock number $\gamma = \rho a c R^4 / I_\beta$. The distinguishing feature of this result in comparison to [7] is the dependence on ω following from consideration of a non-constant hub velocity $\dot{\psi} = \Omega + \omega$.

$$\begin{aligned} M_{\psi_{aero}} = \frac{1}{8}\gamma I_{\beta}\Omega^2 \bigg\{ & - \frac{c_{d_0}}{a} + \phi_{3/4}^2 - \theta \bigg(\phi_{3/4} \bigg) \\ & - \frac{\omega}{\Omega}\bigg(2\frac{c_{d_0}}{a} + \theta\phi_{3/4} \bigg) \\ & + \frac{\dot{\zeta}}{\Omega}\bigg((2\frac{c_{d_0}}{a} + \theta\phi_{3/4})(1 - \frac{4}{3}e) \bigg) \\ & - \frac{\dot{\beta}}{\Omega}\bigg((\theta - 2\phi_{3/4})(1 - \frac{4}{3}e) \bigg) \bigg\} \end{aligned} \tag{3.27}$$

$$\begin{aligned} M_{\zeta_{aero}} = \frac{1}{8}\gamma I_{\beta}\Omega^2 \bigg\{ & (\frac{c_{d_0}}{a} - \phi_{3/4}^2)(1 - \frac{4}{3}e) + \theta \bigg(\phi_{3/4}(1 - \frac{4}{3}e) \bigg) \\ & + \frac{\omega}{\Omega}\bigg((2\frac{c_{d_0}}{a} + \theta\phi_{3/4})(1 - \frac{4}{3}e) \bigg) \\ & - \frac{\dot{\zeta}}{\Omega}\bigg((2\frac{c_{d_0}}{a} + \theta\phi_{3/4})(1 - \frac{8}{3}e + 2e^2) \bigg) \\ & + \frac{\dot{\beta}}{\Omega}\bigg((\theta - 2\phi_{3/4})(1 - \frac{8}{3}e + 2e^2) \bigg) \bigg\} \end{aligned} \tag{3.28}$$

$$\begin{aligned} M_{\beta_{aero}} = \frac{1}{8}\gamma I_{\beta}\Omega^2 \bigg\{ & - (1 + \frac{c_{d_0}}{a})\phi_{3/4}(1 - \frac{4}{3}e) + \theta \bigg(1 - \frac{4}{3}e \bigg) \\ & + \frac{\omega}{\Omega}\bigg((2\theta - (1 + \frac{c_{d_0}}{a})\phi_{3/4})(1 - \frac{4}{3}e) \bigg) \\ & - \frac{\dot{\zeta}}{\Omega}\bigg((2\theta - (1 + \frac{c_{d_0}}{a})\phi_{3/4})(1 - \frac{8}{3}e + 2e^2) \bigg) \\ & - \frac{\dot{\beta}}{\Omega}\bigg((1 + \frac{c_{d_0}}{a})(1 - \frac{8}{3}e + 2e^2) \bigg) \bigg\} \end{aligned} \tag{3.29}$$

The final generalized moment vector required for the overall equation of motion Eq. 3.8 is $\boldsymbol{N} = \{-M_{\psi_{aero}}, -M_{\zeta_{aero}}, -M_{\beta_{aero}}\}$; incorporating moments about the hub, lag, and flap axes given in Eqs. 3.27–3.29. Near trim at speed Ω, this can be written affine in the perturbation angles $\mathbf{x}$ and rates $\dot{\mathbf{x}}$ defined in Eq. 3.7. The dependence on lag angle is due only to enforcing the lag-pitch coupling constraint $\theta = \theta_0 + (\Delta\theta/\Delta\zeta)\tilde{\zeta}$. A positive value for $\Delta\theta/\Delta\zeta$ permits a rearward lag deflection to increase blade pitch and upward flapping moment, and a negative value for $\Delta\theta/\Delta\zeta$ has the opposite effect.

$$
\begin{aligned}
\boldsymbol{N} = \frac{1}{8}\gamma I_\beta \Omega^2 &\begin{bmatrix} (\theta_0\phi_{3/4} - \phi_{3/4}^2 + \frac{c_{d_0}}{a}) \\ -(\theta_0\phi_{3/4} - \phi_{3/4}^2 + \frac{c_{d_0}}{a})(1 - \frac{4}{3}e) \\ -(\theta_0 - \phi_{3/4} - \frac{c_{d_0}}{a}\phi_{3/4})(1 - \frac{4}{3}e) \end{bmatrix} \\
+ \frac{1}{8}\gamma I_\beta \Omega^2 &\begin{bmatrix} (2\frac{c_{d_0}}{a}+\theta_0\phi_{3/4}) & -(2\frac{c_{d_0}}{a}+\theta_0\phi_{3/4})(1-\frac{4}{3}e) & (\theta_0-2\phi_{3/4})(1-\frac{4}{3}e) \\ -(2\frac{c_{d_0}}{a}+\theta_0\phi_{3/4})(1-\frac{4}{3}e) & (2\frac{c_{d_0}}{a}+\theta_0\phi_{3/4})(1-\frac{8}{3}e+2e^2) & -(\theta_0-2\phi_{3/4})(1-\frac{8}{3}e+2e^2) \\ -(2\theta_0-(1+\frac{c_{d_0}}{a})\phi_{3/4})(1-\frac{4}{3}e) & (2\theta_0-(1+\frac{c_{d_0}}{a})\phi_{3/4})(1-\frac{8}{3}e+2e^2) & (1+\frac{c_{d_0}}{a})(1-\frac{8}{3}e+2e^2) \end{bmatrix} \dot{\mathbf{x}} \\
+ \frac{1}{8}\gamma I_\beta \Omega^2 &\begin{bmatrix} \phi_{3/4} \\ -\phi_{3/4}(1 - \frac{4}{3}e) \\ -(1 - \frac{4}{3}e) \end{bmatrix} \begin{bmatrix} 0 & \frac{\Delta\theta}{\Delta\zeta} & 0 \end{bmatrix} \boldsymbol{x}
\end{aligned}
\tag{3.30}
$$

3.6 Hinge Losses

Rotational friction in the physical flap hinge and skewed lag-pitch hinge cause energy losses which must be represented in the dynamical model. These effects are lumped into equivalent nondimensional linear damping coefficients c_β and c_ζ for flap and lag in the analysis. Instead of fitting these parameters from data, reasonable estimates are derived by an energy argument which highlights some expected scaling relations for these coefficients.

The pin joints are principally loaded by the outward centrifugal force F of the spinning blade. Here station x is the spanwise distance from the hinge, and r_{cm} is the distance of the blade center of mass from the hinge.

$$
\begin{aligned}
F &= \Omega^2 \int (eR + xR)\, dm \\
F &= \Omega^2 R(\int e\, dm + \int x\, dm) \\
F &= \Omega^2 R(em + r_{cm} m)
\end{aligned}
\tag{3.31}
$$

Both the blade mass and the blade center of mass can be defined in terms of the flap inertia I_β, radius of gyration k, and radius of oscillation l for the blade as defined in Eq. 3.10–3.11. As a result, the normal force is shown to scale by the blade radius and blade inertia, and depends on nondimensional parameters for the radius of oscillation and radius of gyration.

$$F = \Omega^2 \frac{1}{R} I_\beta \left(\frac{e}{k^2} + \frac{1}{l}\right) \tag{3.32}$$

The physical flap hinge of Fig. 3.5 is modeled as a plain journal bearing or short shoe brake, for which the friction torque τ_{ξ_1} depends on the coefficient of friction μ_1 between the steel pin and plastic hole, the radius of the pin R_P, and the side load force F [59]. A nondimensional pin geometry parameter G_P is defined such that $R_P = G_P R$. The work done by friction torque τ_{ξ_1} integrated over one cycle of flap amplitude A_β is W_{ξ_1}.

$$\begin{aligned} \tau_{\xi_1} &= \mu_1 G_P R F \\ W_{\xi_1} &= 4 A_\beta \tau_{\xi_1} \\ W_{\xi_1} &= 4 I_\beta \Omega^2 A_\beta \mu_1 G_P \left(\frac{e}{k^2} + \frac{1}{l}\right) \end{aligned} \tag{3.33}$$

If instead, a linear damping model about the flap coordinate were considered, the flap hinge torque τ_β would be proportional to the velocity by nondimensional damping coefficient c_β and normalizing factor $I_\beta \Omega$. The integrated viscous work W_β over one cycle can be calculated based on the angular amplitude A_β and frequency Ω.

$$\begin{aligned} \tau_\beta &= I_\beta \Omega c_\beta \dot{\beta} \\ W_\beta &= \pi I_\beta \Omega^2 A_\beta^2 c_\beta \end{aligned} \tag{3.34}$$

The energy equivalent nondimensional damping c_β is found by equating these two different expressions for the flap cycle work. It is seen to depend only on the ratiometric geometry of the propeller, the friction coefficient, and the nominal amplitude. In particular this coefficient is independent of absolute scale or operating speed.

$$c_\beta = \frac{4}{\pi}\frac{\mu_1 G_P}{A_\beta}(\frac{e}{k^2} + \frac{1}{l}) \tag{3.35}$$

The skewed lag-pitch hinge experiences a friction torque τ_{ξ_2} which is the sum of two terms. The first term is a plain bearing friction torque under a side load of $F\cos(\delta)$. In addition, a large axial load $F|\sin(\delta)|$ is carried by two PTFE washers of radius R_D which slide against each other with material coefficient of friction μ_2. This contributes a second term to the friction torque about the skew axis, which is modeled as the torque of a uniform pressure contact disk brake [59]. Once again a geometric parameter G_D for these disks is introduced such that $R_D = G_D R$. The friction work W_{ξ_2} of torque τ_{ξ_2} integrated over one cycle of lag amplitude A_ζ is computed, recognizing from the geometry of Fig. 3.5 that the skew hinge axis rotates with an amplitude $A_\zeta/\cos(\delta)$.

$$\begin{aligned}
\tau_{\xi_2} &= \mu_1 G_P R F\cos(\delta) + \frac{2}{3}\mu_2 G_D R F|\sin(\delta)| \\
W_{\xi_2} &= 4A_\zeta \tau_{\xi_2}\frac{1}{\cos(\delta)} \\
W_{\xi_2} &= 4I_\beta \Omega^2 A_\zeta(\mu_1 G_P + \frac{2}{3}\mu_2 G_D|\tan(\delta)|)(\frac{e}{k^2} + \frac{1}{l})
\end{aligned} \tag{3.36}$$

As before, setting this friction work expression equal to a damping work expression allows an equivalent nondimensional damping coefficient c_ζ to be defined for the conventional lag coordinate in the dynamics.

$$c_\zeta = \frac{4}{\pi}\frac{1}{A_\zeta}(\mu_1 G_P + \frac{2}{3}\mu_2 G_D|\tan(\delta)|)(\frac{e}{k^2} + \frac{1}{l}) \tag{3.37}$$

The final contribution to the overall dynamics in Eq. 3.8, $\boldsymbol{\tau}_{hinge}$, is now written in terms of these damping coefficients and the coordinate velocities $\dot{\mathbf{x}} = (\omega, \dot{\zeta}, \dot{\beta})$.

$$\boldsymbol{\tau}_{hinge} = \begin{bmatrix} 0 & 0 & 0 \\ 0 & -I_\beta \Omega c_\zeta & 0 \\ 0 & 0 & -I_\beta \Omega c_\beta \end{bmatrix} \dot{\mathbf{x}} \tag{3.38}$$

For the special case of a blade with uniform mass distribution between the hinge at radius e and the blade tip at radius R, the nondimensional radius of gyration and radius of oscillation are determined by e as shown previously in Eq. 3.17–3.18. After substitution, the damping coefficients are found to take on the values previously reported in [64].

$$c_\beta = \frac{6}{\pi} \frac{\mu_1 G_P}{A_\beta} \frac{1+e}{(1-e)^2} \tag{3.39}$$

$$c_\zeta = \frac{6}{\pi} \frac{1}{A_\zeta} (\mu_1 G_P + \frac{2}{3} \mu_2 G_D |\tan(\delta)|) \frac{1+e}{(1-e)^2} \tag{3.40}$$

The naive linear model requires choosing representative amplitudes A_ζ and A_β to determine coefficients c_ζ and c_β. Instead of making such an assumption, the equation of motion can be solved iteratively to determine A_ζ and A_β for a particular drive amplitude. This approach was used to determine the theory curves for comparison with the experimental data in Chapter 4, and allows the model to predict the characteristic low amplitude nonlinearity in the gain response evident in Fig. 4.6.

3.7 Motor Equation And Speed Governor

The shaft torque required to overcome the rotor aerodynamic drag as well as excite the desired lag-pitch motion for cyclic control is generated by a single brushless electric motor. The motor torque Q obeys the basic DC motor model of Eq. 3.41. The applied terminal voltage V induces an electrical current i subject to the electrical motor constant K_e and electrical resistance R_{ohm}. The torque Q is proportional to the current i less the no load current i_0.

$$\begin{aligned} Q &= K_e(i - i_0) \\ i &= \frac{1}{R_{ohm}}(V - K_e\dot{\psi}) \end{aligned} \tag{3.41}$$

An average rotor speed Ω is maintained by employing a software defined proportional-integral (PI) control law with gains K_P and K_I. The applied voltage V is calculated according to Eq. 3.42 as the sum of three parts: the proportional control term, the integral control term, and an added sinusoidal signal $\tilde{V}$ used to excite the lag-pitch mode. During experiments, $\tilde{V}$ is computed as $\tilde{V} = A\cos\psi$ based on a desired voltage amplitude A and the instantaneous hub orientation ψ.

$$V = -K_P(\dot{\psi} - \Omega) - K_I\int(\dot{\psi} - \Omega)dt + \tilde{V} \tag{3.42}$$

The resulting motor torque is given by Eq. 3.43. The first two terms reflect the action of the proportional and integral control laws, while the remainder of the expression only depends on the physical motor properties.

$$Q = -\frac{K_P K_e}{R_{ohm}}(\dot{\psi} - \Omega) - \frac{K_I K_e}{R_{ohm}}\int(\dot{\psi} - \Omega)dt + \frac{K_e}{R_{ohm}}\tilde{V} - \frac{K_e^2}{R_{ohm}}\dot{\psi} - K_e i_0 \tag{3.43}$$

In steady operation with imposed $\tilde{V} = 0$ the integral control action ensures the rotor reaches a steady trim state with hub speed $\dot{\psi}$ equal to constant Ω and the motor torque Q taking a constant value Q_0. This trim condition is expressed in Eq. 3.44.

$$Q_0 = -\frac{K_I K_e}{R_{ohm}}\int(\dot{\psi} - \Omega)dt - \frac{K_e^2}{R_{ohm}}\Omega - K_e i_0 \tag{3.44}$$

The motor equation may be rewritten relative to this trim state in terms of perturbation variables $\tilde{Q} = Q - Q_0$ and $\omega = \dot{\psi} - \Omega$. In Eq. 3.45 the integral of ω is furthermore defined to be the (virtual) angle $\tilde{\psi}$ satisfying $\tilde{\psi} = \psi - \Omega t$.

$$\tilde{Q} = -(K_P + K_e)\frac{K_e}{R_{ohm}}\omega - K_I \frac{K_e}{R_{ohm}}\tilde{\psi} + \frac{K_e}{R_{ohm}}\tilde{V} \tag{3.45}$$

Equation 3.45 suggests the combined effects of the motor dynamics and speed governor are to act as a damping term on velocity ω with coefficient c_m and stiffness term on the (virtual) angle $\tilde{\psi}$ with coefficient k_m. The vector of joint torques due to the motor $\boldsymbol{\tau}_{motor}$ required by Eq. 3.8 can finally be written in vector form in terms of the perturbation variables $\mathbf{x}$, $\dot{\mathbf{x}}$ defined in Eq. 3.7 and the imposed sinusoidal input $\tilde{V}$.

$$c_m = (K_P + K_e)\frac{K_e}{R_{ohm}} \qquad k_m = K_I \frac{K_e}{R_{ohm}} \tag{3.46}$$

$$\boldsymbol{\tau}_{motor} = \begin{bmatrix} Q_0 \\ 0 \\ 0 \end{bmatrix} + \begin{bmatrix} -k_m & 0 & 0 \\ 0 & 0 & 0 \\ 0 & 0 & 0 \end{bmatrix} \mathbf{x} + \begin{bmatrix} -c_m & 0 & 0 \\ 0 & 0 & 0 \\ 0 & 0 & 0 \end{bmatrix} \dot{\mathbf{x}} + \begin{bmatrix} \frac{K_e}{R_{ohm}} \\ 0 \\ 0 \end{bmatrix} \tilde{V} \tag{3.47}$$

3.8 Equilibrium

Suppose that a constant applied motor torque Q_0 yields a steady trim state where the propeller spins with velocity Ω. The steady coordinate configuration is $\mathbf{q}_0 = (\Omega t, \zeta_0, \beta_0)$ and the velocities are $\dot{\mathbf{q}}_0 = (\Omega, 0, 0)$ for constant Ω. Further assume that in this state the residual internal static friction torques at the joints are zero. This assumed solution can be inserted into the equation of motion (Eq. 3.8) to solve for the unknown angles ζ_0 and β_0 and unknown drive torque Q_0. Under these conditions the steady Coriolis term $\boldsymbol{C}_0$, aerodynamic forces $\boldsymbol{N}_0$, and applied motor torque Q_0 obey the equilibrium expressed in Eq. 3.48.

$$\boldsymbol{C}_0 + \boldsymbol{N}_0 = \begin{bmatrix} Q_0/N_b \\ 0 \\ 0 \end{bmatrix} \tag{3.48}$$

The Coriolis term $\boldsymbol{C}_0$ was given previously in Eq. 3.15. The aerodynamic force $\boldsymbol{N}_0$ comes from the constant term in Eq. 3.30. The resulting equilibrium is now given by Eq. 3.49 where θ_0 is the collective blade pitch and $\phi_{3/4}$ is the downwash angle given by Eq. 3.26.

$$I_\beta\Omega^2\begin{bmatrix}0\\ \frac{e}{l}\zeta_0\\ (1+\frac{e}{l})\beta_0\end{bmatrix}+\frac{1}{8}\gamma I_\beta\Omega^2\begin{bmatrix}(\theta_0\phi_{3/4}-\phi_{3/4}^2+\frac{c_{d0}}{a})\\ -(\theta_0\phi_{3/4}-\phi_{3/4}^2+\frac{c_{d0}}{a})(1-\frac{4}{3}e)\\ -(\theta_0-\phi_{3/4}-\frac{c_{d0}}{a}\phi_{3/4})(1-\frac{4}{3}e)\end{bmatrix}=\begin{bmatrix}Q_0/N_b\\ 0\\ 0\end{bmatrix} \tag{3.49}$$

The trim drive torque given by Eq. 3.50 is obtained immediately from the first row. The corresponding shaft torque coefficient C_Q is computed in Eq. 3.51 from its definition after substituting in the disc solidity σ [41]. This trim value for the shaft torque coefficient provides context for the magnitude of the torque modulation used for cyclic control in the experiments.

$$Q_0=\frac{1}{8}\gamma I_\beta\Omega^2N_b(\theta_0\phi_{3/4}-\phi_{3/4}^2+\frac{c_{d0}}{a}) \tag{3.50}$$

$$C_Q=\frac{1}{8}a\sigma(\theta_0\phi_{3/4}-\phi_{3/4}^2+\frac{c_{d0}}{a}) \tag{3.51}$$

The lag and flap angles are found by solving the second and third row equations after simplification.

$$\begin{bmatrix}\frac{e}{l}\zeta_0\\ (1+\frac{e}{l})\beta_0\end{bmatrix}=\frac{1}{8}(1-\frac{4}{3}e)\gamma\begin{bmatrix}\theta_0\phi_{3/4}-\phi_{3/4}^2+\frac{c_{d0}}{a}\\ \theta_0-\phi_{3/4}-\frac{c_{d0}}{a}\phi_{3/4}\end{bmatrix} \tag{3.52}$$

$$\begin{aligned}\zeta_0&\approx\frac{1}{8}\frac{l}{e}(1-\frac{4}{3}e)\gamma(\theta_0\phi_{3/4}-\phi_{3/4}^2+\frac{c_{d0}}{a})\\ \beta_0&\approx\frac{1}{8}\frac{1}{1+\frac{e}{l}}(1-\frac{4}{3}e)\gamma(\theta_0-\phi_{3/4}-\frac{c_{d0}}{a}\phi_{3/4})\end{aligned} \tag{3.53}$$

3.9 Linearized System Equations

The governing equations for small variations in the hub, lag, and flap motion with respect to equilibrium are found by substituting into Eq. 3.8 from Eq. 3.12-3.14, 3.30, 3.38, and 3.47 and discarding the constant terms associated with trim. This results in a linear system of equations in the state vector $\mathbf{x} = \{\tilde{\psi}, \tilde{\zeta}, \tilde{\beta}\}$ with a single input which is the voltage excitation $\tilde{V}$ imposed to drive the cyclic response. We are primarily interested in the 1/rev system response because in practice the excitation is a function of the hub rotation, $\tilde{V} = A\cos\psi$ with some amplitude A. As a result it is convenient to introduce a nondimensional time $\hat{t}$ such that $\hat{t} = \Omega t$. Coordinate derivatives are rewritten nondimensionally where now $\mathbf{x}'$ and $\mathbf{x}''$ are derivatives of coordinates $\mathbf{x}$ with respect to nondimensional time $\hat{t}$.

$$\begin{aligned} \mathbf{x} &= \begin{bmatrix} \tilde{\psi} & \tilde{\zeta} & \tilde{\beta} \end{bmatrix} \\ \mathbf{x}' &= \begin{bmatrix} \frac{\omega}{\Omega} & \frac{\dot{\zeta}}{\Omega} & \frac{\dot{\beta}}{\Omega} \end{bmatrix} \\ \mathbf{x}'' &= \begin{bmatrix} \frac{\dot{\omega}}{\Omega^2} & \frac{\ddot{\zeta}}{\Omega^2} & \frac{\ddot{\beta}}{\Omega^2} \end{bmatrix} \end{aligned} \tag{3.54}$$

We similarly wish to nondimensionalize the input voltage excitation $\tilde{V}$ in a physically meaningful way in order to permit comparisons between systems with very different motor electrical characteristics. We choose to define a nondimensional scaled input u which is proportional to $\tilde{V}$, defined in Eq. 3.55. The scale factor is suggested by observing that under the motor model of Eq. 3.41 the motor torque rises proportional to an instantaneous increment in voltage by a constant of K_e/R_{ohm}. This torque can then be normalized by a factor of $\rho\pi R^5\Omega^2$ or equivalently $N_b I_\beta \gamma\Omega^2/(a\sigma)$, in similarity to how the rotor torque coefficient C_Q is conventionally defined [41]. The input u is the input to the full rotor system, so it is divided by N_b in the single blade equation.

$$u = \frac{1}{\rho\pi R^5\Omega^2}\frac{K_e}{R_{ohm}}\tilde{V} = \frac{a\sigma}{N_b I_\beta\gamma\Omega^2}\frac{K_e}{R_{ohm}}\tilde{V} \tag{3.55}$$

The final nondimensional equation of motion for the half propeller is obtained after dividing through by Ω^2 as well as the flap inertia I_β to obtain Eq. 3.56. The coefficient matrices owing to aerodynamic terms have been held separate from those describing inertial, motor, and friction dynamics to highlight their contributions to the overall model. Given this linear state space model, the cyclic hub speed, lag, and flap response are found directly by evaluating the associated transfer functions from the input u at frequency 1 (once-per-revolution excitation).

$$
\begin{aligned}
&\begin{bmatrix} 1 + X_{I_h} + 2\frac{e}{l} + \frac{e^2}{k^2} & -1 - \frac{e}{l} & 0 \\ -1 - \frac{e}{l} & 1 & 0 \\ 0 & 0 & 1 \end{bmatrix} \boldsymbol{x}'' + \left(\begin{bmatrix} \frac{c_m}{\Omega I_\beta}/N_b & -2\frac{e}{l}\zeta_0 & -2(1+\frac{e}{l})\beta_0 \\ 2\frac{e}{l}\zeta_0 & c_\zeta & 2\beta_0 \\ 2(1+\frac{e}{l})\beta_0 & -2\beta_0 & c_\beta \end{bmatrix} \right. \\
&\left. + \frac{1}{8}\gamma \begin{bmatrix} (2\frac{c_{d0}}{a}+\theta_0\phi_{3/4}) & -(2\frac{c_{d0}}{a}+\theta_0\phi_{3/4})(1-\frac{4}{3}e) & (\theta_0-2\phi_{3/4})(1-\frac{4}{3}e) \\ -(2\frac{c_{d0}}{a}+\theta_0\phi_{3/4})(1-\frac{4}{3}e) & (2\frac{c_{d0}}{a}+\theta_0\phi_{3/4})(1-\frac{8}{3}e+2e^2) & -(\theta_0-2\phi_{3/4})(1-\frac{8}{3}e+2e^2) \\ -(2\theta_0-(1+\frac{c_{d0}}{a})\phi_{3/4})(1-\frac{4}{3}e) & (2\theta_0-(1+\frac{c_{d0}}{a})\phi_{3/4})(1-\frac{8}{3}e+2e^2) & (1+\frac{c_{d0}}{a})(1-\frac{8}{3}e+2e^2) \end{bmatrix} \right) \boldsymbol{x}' \\
&+ \left(\begin{bmatrix} \frac{k_m}{\Omega^2 I_\beta}/N_b & 0 & 0 \\ 0 & \frac{e}{l} & 0 \\ 0 & 0 & 1+\frac{e}{l} \end{bmatrix} + \frac{1}{8}\gamma \begin{bmatrix} \phi_{3/4} \\ -\phi_{3/4}(1-\frac{4}{3}e) \\ -(1-\frac{4}{3}e) \end{bmatrix} \begin{bmatrix} 0 & \frac{\Delta\theta}{\Delta\zeta} & 0 \end{bmatrix} \right) \boldsymbol{x} = \begin{bmatrix} \frac{\gamma}{a\sigma} \\ 0 \\ 0 \end{bmatrix} u \qquad (3.56)
\end{aligned}
$$

The key interest for aircraft controls design will be the amplitude and phase relation between the input u and the ensuing cyclic pitch variation or flapping motion. In the case of small collective pitch θ_0 and small trim angles ζ_0 and β_0 the sparse dominant terms in Eq. 3.56 can be qualitatively interpreted as a cascaded response to the input u. Recalling that the state vector is ordered $\mathbf{x} = \{\tilde{\psi}, \tilde{\zeta}, \tilde{\beta}\}$, the voltage modulation described by u is seen to only contribute directly to the hub acceleration. This hub acceleration is coupled into lag accelerations primarily through the inertia matrix. Lag deflections induce pitch changes by the geometric constant $\Delta\theta/\Delta\zeta$, and the resulting aerodynamic forces drive the flap motion.

The nondimensional governing equations are almost entirely independent of absolute scale in terms of either physical extent (R, I_β, m, etc.) or operating speed (Ω). The only exception are the groupings $c_m/(\Omega I_\beta)$ and $k_m/(\Omega^2 I_\beta)$ related to the motor dynamics. Since the effective motor stiffness and damping coefficients c_m and k_m are determined by choice of software speed control gains it is straightforward to conduct experiments at varied scales and speeds with identical governing equations.

3.10 Illustrative Simplified Models

3.10.1 Flapping

While the lead-lag and flap motions of the real rotor are coupled through both Coriolis terms and aerodynamic effects, it is useful to consider the behavior of simplified flap-only and lag-only systems. First, we can can consider the flapping dynamics about an offset hinge in vacuum at rotational speed Ω. From Eq. 3.56 we see the undamped flapping equation of motion reduces to

$$I_\beta \ddot{\beta} + I_\beta \Omega^2 (1 + \frac{e}{l})\beta = 0$$

which motivates the definition of the flap frequency ratio λ_β

$$\lambda_\beta = \sqrt{1 + \frac{e}{l}} \tag{3.57}$$

in terms of the eccentric hinge location e and the radius of oscillation l defined in Eq. 3.11. The undamped natural frequency of the flapping motion is proportional to the frequency of revolution. Since λ_β must always be greater than one, we should expect to be forcing the flap motion below the natural frequency during typical cyclic operation. For the special case of a blade with uniform mass density between the hinge and the blade tip, the radius of oscillation is $l = (2/3)(1 - e)$ resulting in a flap frequency purely a function of the hinge location.

$$\lambda_\beta = \sqrt{1 + \frac{3}{2}\frac{e}{1 - e}} \tag{3.58}$$

This is precisely the conventional result for an articular rotor with offset hinge given by [33].

The flap frequency ratio λ_β is plotted as a function of e for uniform density blades in Fig. 3.8. The value of λ_β is never less than one, and it rises moderately as the hinge location is moved outward from center. Overlaid on this plot are the calculated flap frequency ratios

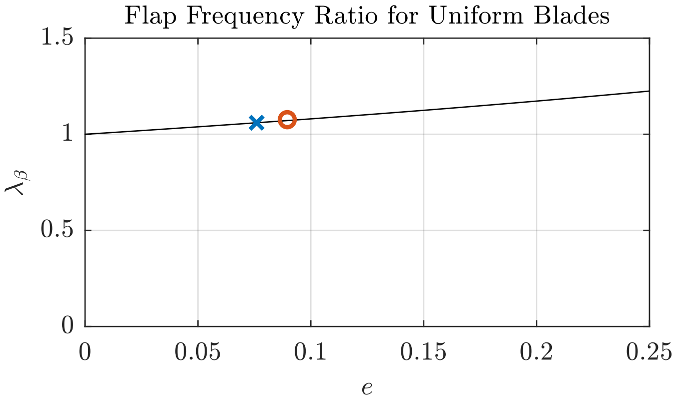

Figure 3.8: Flap frequency ratio.

Table 3.1: Undamped flap frequency ratio.

construction	diameter	mass	e	l	λ_β
carbon fiber, flat plate	10 cm	0.39 g	0.09	0.61	1.07
plastic, symmetric	31.8 cm	5.4 g	0.076	0.62	1.06
acetal, flat plate	100 cm	362 g	0.09	0.62	1.07
wood, symmetric	100 cm	223 g	0.09	0.57	1.08

for the physical rotors constructed for testing in this work, taking into account their true nonuniform mass distribution. The 30 cm rotor described in Chapter 4 is marked in blue, and the 10 cm and 100 cm rotors described in Chapter 5 are marked in red. The textbook expression assuming uniform blades accurately describes the physical blades even though all the physical blades examined in this work are significantly weighted towards the root as a result of the blade grip and hinge. The corresponding tabulated values in Table 3.1 show the flap frequency ratio is primarily a function of hinge location. It is lightly affected by the mass distribution, but can be considered independent of gross blade mass or size.

3.10.2 Lead-Lag

The lead-lag blade dynamics can also be considered in isolation. We will consider motions in the rotor plane associated with the hub speed changes and lag angle variation. Retaining only terms related to $\tilde{\psi}$ and $\tilde{\zeta}$, Eq. 3.59 yields coupled second order ODEs.

$$I_\beta \begin{bmatrix} 1 + X_{I_h} + 2\frac{e}{l} + \frac{e^2}{k^2} & -1 - \frac{e}{l} \\ -1 - \frac{e}{l} & 1 \end{bmatrix} \begin{bmatrix} \ddot{\tilde{\psi}} \\ \ddot{\tilde{\zeta}} \end{bmatrix} + I_\beta \Omega^2 \begin{bmatrix} 0 & 0 \\ 0 & \frac{e}{l} \end{bmatrix} \begin{bmatrix} \tilde{\psi} \\ \tilde{\zeta} \end{bmatrix} = \begin{bmatrix} 0 \\ 0 \end{bmatrix} \tag{3.59}$$

Coordinate $\tilde{\psi}$ itself is not required for the equation of motion, so the system can be written as only three coupled first order ODEs.

$$\begin{bmatrix} \dot{\zeta} \\ \ddot{\tilde{\psi}} \\ \ddot{\zeta} \end{bmatrix} = \begin{bmatrix} 0 & 0 & 1 \\ -\dfrac{e(1+\frac{e}{l})}{l(\frac{e^2}{k^2} - \frac{e^2}{l^2} + X_{I_h})}\Omega^2 & 0 & 0 \\ -\dfrac{e(1+\frac{e^2}{k^2} + 2\frac{e}{l} + X_{I_h})}{l(\frac{e^2}{k^2} - \frac{e^2}{l^2} + X_{I_h})}\Omega^2 & 0 & 0 \end{bmatrix} \begin{bmatrix} \zeta \\ \dot{\tilde{\psi}} \\ \dot{\zeta} \end{bmatrix} \tag{3.60}$$

The system has one eigenvalue at zero and a conjugate pair of pure imaginary eigenvalues.

$$\left\{ 0, \pm\sqrt{\frac{e(2ek^2 + e^2 l + k^2 l(1 + X_{I_h}))}{e^2(l+k)(l-k) + k^2 l^2 X_{I_h}}}\Omega \mathrm{i} \right\} \tag{3.61}$$

Note that the fraction in the radical is always positive real since $l > k$. This relation is derived in Eq. 3.62 by starting from the parallel axis theorem assuming an inertia I_{cm} about the blade center of mass and then applying the definitions of k and l from Eq. 3.10 and 3.11, recalling that all of k, l, and I_{cm} are real positive.

$$\begin{aligned} I_\beta &= m r_{cm}^2 R^2 + I_{cm} \\ \frac{I_\beta^2}{m^2 r_{cm}^2 R^4} &= \frac{I_\beta}{mR^2} + I_{cm} \frac{I_\beta}{m^2 r_{cm}^2 R^4} \\ l^2 &= k^2 + I_{cm} l^2 \\ l &> k \end{aligned} \tag{3.62}$$

The associated lag frequency ratio λ_ζ given by Eq. 3.63 is the magnitude of the eigenvalue normalized by the operating speed Ω.

$$\lambda_\zeta = \sqrt{\frac{e(2ek^2 + e^2 l + k^2 l(1 + X_{I_h}))}{e^2(l+k)(l-k) + k^2 l^2 X_{I_h}}} \tag{3.63}$$

In the limit as the hub inertia grows very large with respect to the blade inertia, the lag frequency ratio no longer depends on the hub inertia and reduces to the ultimate value given by Eq. 3.64.

$$\lambda_\zeta = \sqrt{\frac{e}{l}} \tag{3.64}$$

For the further special case of a blade with uniform mass density between the hinge and the blade tip, the radius of oscillation is $l = (2/3)(1-e)$ resulting in a lag frequency purely a function of the hinge location shown in Eq. 3.65. This is the conventional result considered in the helicopter literature [33].

$$\lambda_\zeta = \sqrt{\frac{3}{2}\frac{e}{1-e}} \tag{3.65}$$

In the limit as the hub inertia grows very small with respect to the blade, the lag frequency ratio reduces to Eq. 3.66.

$$\lambda_\zeta = \sqrt{\frac{2k^2 + el + k^2\frac{l}{e}}{l^2 - k^2}} \tag{3.66}$$

The specialized result for uniform blade mass distribution is shown in Eq. 3.67. This small hub inertia limiting case is not typically treated in the helicopter literature. It yields a lag frequency ratio much greater than that in the large hub inertia limit given uniform mass distribution blades mounted with any reasonable hinge eccentricity e.

$$\lambda_\zeta = \sqrt{2\left(\frac{1}{e} + 3\frac{1}{1-e} - 1\right)} \tag{3.67}$$

Figure 3.9 compares the lag frequency ratio obtained for uniform mass distribution blades mounted with different values of eccentricity e as determined by the light hub and heavy hub limiting cases. The true value for λ_ζ for a real system with finite nonzero hub inertia

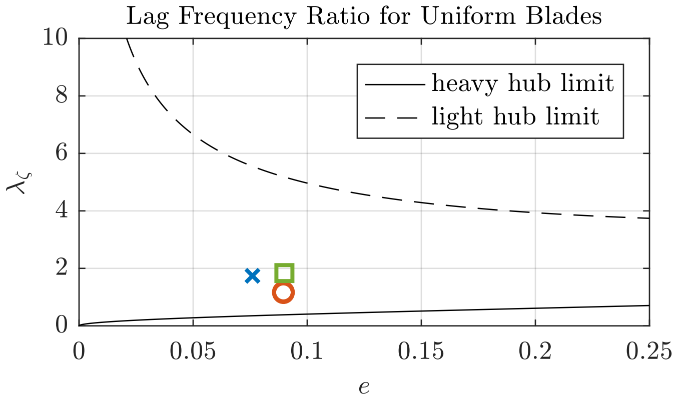

Figure 3.9: Lag frequency ratio.

Table 3.2: Undamped lag frequency ratio.

construction	diameter	mass	e	X_{Ih}	λ_ζ	
carbon fiber, flat plate	10 cm	0.39 g	0.09	0.15	1.14	
plastic, symmetric	31.8 cm	5.4 g	0.076	0.05	1.74	
acetal, flat plate	100 cm	362 g	0.09	0.15	1.12	
acetal, flat plate	100 cm	362 g	0.09	0.04	1.84	(reduced inertia)

is expected to interpolate between these limits. Marked on this plot are the calculated lag frequency ratios for the physical rotors constructed for testing in this work. The 30 cm rotor described in Chapter 4 is marked in blue, and the 10 cm and 100 cm rotors described in Chapter 5 are marked in red with the hub configuration described in those chapters. In Chapter 5 the large rotor was examined with an artificially increased hub inertia to obtain dynamic similarity with the small rotor. Removing the added hub weight increases the lag frequency to that marked in green. Numerical values are recorded in Table 3.2.

For large conventional helicopters it is reasonable to assume that the combined influence of the turbine engine dynamics and governor as well as the engine inertia reflected through the transmission yield very high effective hub inertias and the conventional result of Eq. 3.65 holds. However, the conventional approximation may significantly underestimate the true lag frequency ratio for new MAV with small direct drive electric motors. In particular, the rotor dynamic response is frequently not scrutinized for multirotor designs, but as it becomes common for large multirotors to add passive lag hinges for stowage these factors may become relevant.

Chapter 4

Rotor Experiments

A series of rotor experiments validate the qualitative and quantitative predictions from the model of Chapter 3 for the rotor torque, hub speed, lag-pitch, and flap response. This chapter expands on the author's previous work in [64].

4.1 Prototype Construction

A 32 cm diameter propeller embodying the kinematics of Section 3.2 was constructed. In combination with a commercial motor and custom electronic motor drive, the device allows controlled experiments of the cyclic system during which torque, speed, blade lag angle, and blade flap angle can be measured. The propeller shown in Fig. 4.1 is constructed from 3D printed plastic parts joined by simple stainless steel pins. The visible plastic screws serve only to retain the pins in place. The blade is an commercial 11% thick, symmetric airfoil bonded into the custom blade grip. Two PTFE plastic washers in the lag hinge serve as thrust bearings to reduce the hinge friction under centrifugal loading.

Critical rotor parameters for model calculations are summarized in Table 5.4. The eccentricity e of the hinge location was chosen to be 0.076 which was the smallest practical value given the construction methods. A representative lift curve slope of $0.1\,/^\circ$ and drag coefficient of 0.06 are used, though studies of similar NACA 0012 airfoils [35] caution that these numbers are uncertain at the varying low Reynolds numbers ($Re < 6.1 \times 10^4$) of these

Table 4.1: Propeller properties.

parameter	symbol	value
tip radius	R	159 mm
number blades	N_b	2
hinge eccentricity	e	0.076
washer disk radius	R_D	1.98 mm
hinge pin radius	R_P	0.52 mm
blade mass	m	5.40 g
hub rotational inertia	-	5.1×10^{-7} kg m^2
blade chord	c	19.3 mm
blade pitch	θ_0	9°
section drag coef	c_{d_0}	0.06
section lift curve slope	a	0.1 /°
friction coef steel-plastic	μ_1	0.20
friction coef PTFE-PTFE	μ_2	0.07
air density	ρ	1.2 kg/m^3
downwash angle	$\phi_{3/4}$	4.4°
flap inertia	I_β	3.9×10^{-5} kg m^2
Lock number	γ	2.18

experiments. The characteristic friction coefficients of the PTFE-PTFE sliding contact and the silicone-lubricated steel-plastic interfaces were estimated in separate tilted-plane tests.

The motor and brushless motor controller drive the propeller rotation and are responsible for applying the once-per-revolution modulation of torque to excite the cyclic mode. The motor is a common brushless motor with a rotating shaft exposed at both ends. The motor orientation is directly measured by a contactless 4096-count magnetic rotary encoder mounted beneath the motor on the controller circuit board, shown in Fig. 4.1. This sensor observes the rotation of a diametrically polarized magnet bonded to the shaft end. These angle measurements are used to update the motor winding commutation at 40 kHz and update the speed controller at 2 kHz. In addition, this direct measurement of the hub rotation is used to calculate the modulation voltage $\tilde{V}$ in order to ensure the phase and frequency of modulation remain synchronous with the hub rotation. The critical parameters for the electronic drive system are summarized in Table 5.5. The motor inertia, emf constant, and combined effective resistance of the motor and driver circuitry are fit values based on

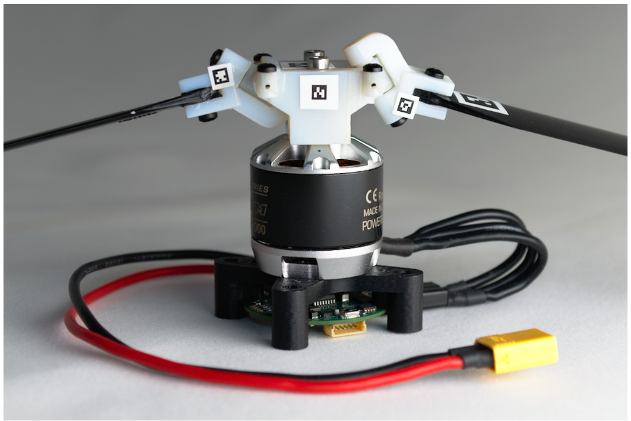

Figure 4.1: Power electronics, motor, and articulated hub for a 318 mm diameter cyclic rotor.

Table 4.2: Motor properties and control gains for 200 rad/s test speed.

parameter	symbol	value
emf constant	K_e	0.00954 V/(rad/s) or N m/A
resistance	R_{ohm}	0.305 ohms
motor rotational inertia	-	3.26×10^{-6} kg m^2
proportional speed gain	K_P	0.03 V/(rad/s)
integral speed gain	K_I	0.03 V/rad

separate frequency response testing of the bare motor without an attached propeller.

During experiments the rotor is supported on a vertical pylon to hold it out of ground effect. Thrust forces and reaction torques are measured by a small six-axis load cell atop the supporting pylon. The drive module of Fig. 4.1 containing the power electronics and motor is mounted directly to the load cell. The propeller is mounted to the rotating face of the motor by two screws to ensure the propeller does not slip relative to the motor during testing.

4.2 Experiments

Experiments were conducted at mean rotor speeds of 100 rad/s, 200 rad/s, and 300 rad/s to determine the sensitivity of the cyclic response to drive amplitude inputs. During low speed and high speed tests, the nominal speed governor gains of Table 5.5 are scaled such that the nondimensional motor coefficients of Eq. 3.46 obtain identical equations of motion in

Eq. 3.56. As a result, measured amplitudes and phase shifts for the torque, hub speed, lag angle, and flap angle response at different test speeds should all fall on single curves from the theory when properly scaled.

At each test speed, a range of amplitudes A for the additive, phase locked excitation voltage $\tilde{V} = A\cos\psi$ are applied and the steady cyclic responses measured. Torque values are derived from the load cell, and hub speed and position measurements are reported by the motor controller. Lag angles are derived from top-down high speed video imagery, and flap angles are derived from side-view strobe photography. Synchronization of these sources is achieved by having the motor controller emit a digital index signal read by the load cell DAQ as well as a visible indicator for the high speed video.

The equation of motion developed for the half-propeller in Eq. 3.56 takes advantage of approximate symmetry to describe the dynamics of a single blade instead of explicitly modeling two blades. To practice cyclic control, one of the blades is mounted with a positive lag-pitch coefficient $\Delta\theta/\Delta\zeta$ and the other is mounted with a negative lag-pitch coefficient, as shown in Fig. 3.5. Model predictions for both the positive and negative case are plotted against the measured data – the difference is only notable in the case of flap, where the purpose of the cyclic system is to ensure the positive and negative blades remain 180° out of phase with each other. The model state space could be extended to explicitly encompass the full system with two independent dissimilar blades, but the simplified model used here exposes the fundamental physics being exploited and makes satisfactory numerical predictions.

4.3 Motor Torque

The amplitude and phase of the first harmonic of the motor reaction torques are plotted in Fig. 4.2 and compared to model predictions for a range of drive voltage amplitudes at three different operating speeds. The motor torques are shown normalized by $\rho\pi R^5\Omega^2$ so that they may be put in the context of the propeller torque coefficient $C_Q = 0.92 \times 10^{-3}$ as calculated from Eq. 3.51. The normalized drive amplitudes u are calculated at each test

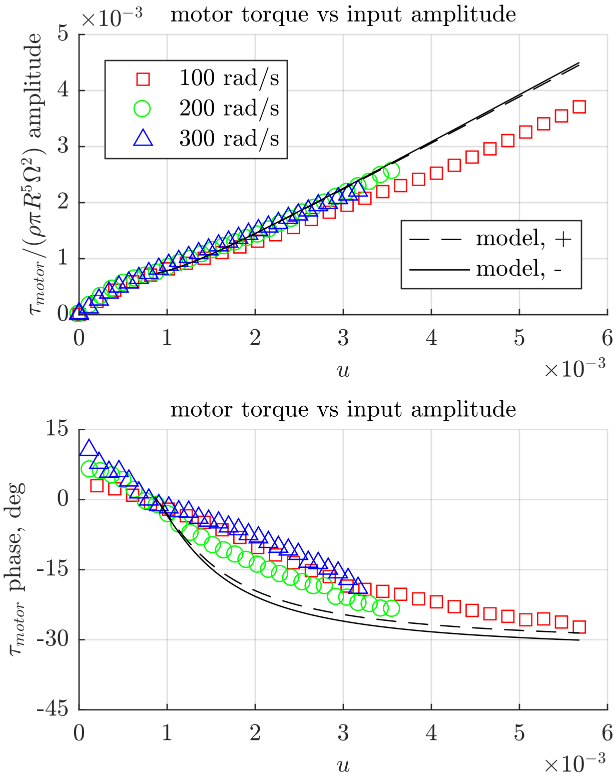

Figure 4.2: Measured motor torque response compared with model prediction for a range of normalized drive torque amplitudes u at three test speeds.

condition from the definition in Eq. 3.55, so that u grows in direct proportion to $\tilde{V}$ for tests conducted at identical average speeds. The input u may be thought of as one of the three terms in Eq. 3.45 which sum to the shaft torque, so it is not surprising that in Fig. 4.2 the normalized torque amplitude closely follows u. Predictions of the torque response amplitude are accurate, but the torque lags the 1/rev modulation in u by up to 15° less than predicted by the model.

Modulating torque incurs a reduction in energy efficiency because the instantaneous power lost to resistance heating inside the motor grows as the square of the torque. This loss can be offset by saved vehicle weight as in the specific example of [61], but it may be advantageous to optimize rotors to require less torque modulation for operation.

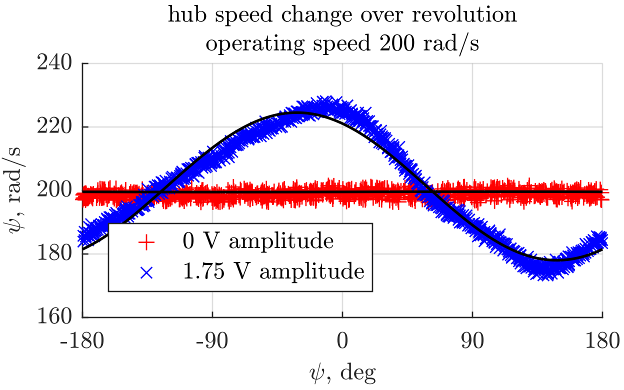

Figure 4.3: Cumulative measurements over one second of operation at 200 rad/s show a hub speed response phase locked to hub orientation. Results with and without an applied sinusoidal drive voltage are shown.

4.4 Hub Speed Response

Variations in the hub speed are easily measured by the motor controller and provide an indicator of the magnitude of the excited lag-pitch-flap response. In these tests the rotor reference speed Ω is fixed, an applied additive voltage amplitude is set, and the cyclic response is obtained. The lag and flap response is obtained rapidly, and we wait several seconds for any transient response of the weak integral speed control law to settle completely before beginning measurements. Speed and position data are sampled for five seconds, representing more than a hundred revolutions of the propeller. The scatter plot of instantaneous hub speed vs position in Fig. 4.3 compounds one second of continuous data, demonstrating that the hub speed variation is phase locked with the rotation and extremely consistent from one revolution to the next. The response can be summarized by the amplitude and phase of the first harmonic fit, also shown. Both the amplitude and rotation phase (direction) of the response can be finely tuned by adjusting the amplitude and phase of the voltage drive.

The hub speed variation ω amplitude and phase are summarized in Fig. 4.4 for a range of drive amplitudes as well as mean operating speeds Ω. For very low drive amplitudes the lag hinges are bound by static friction. In this operating state instead of the hub and blade being joined by a mobile hinge they act effectively as one large inertial mass, the multibody model is no longer appropriate, and very little hub speed variation can be observed.

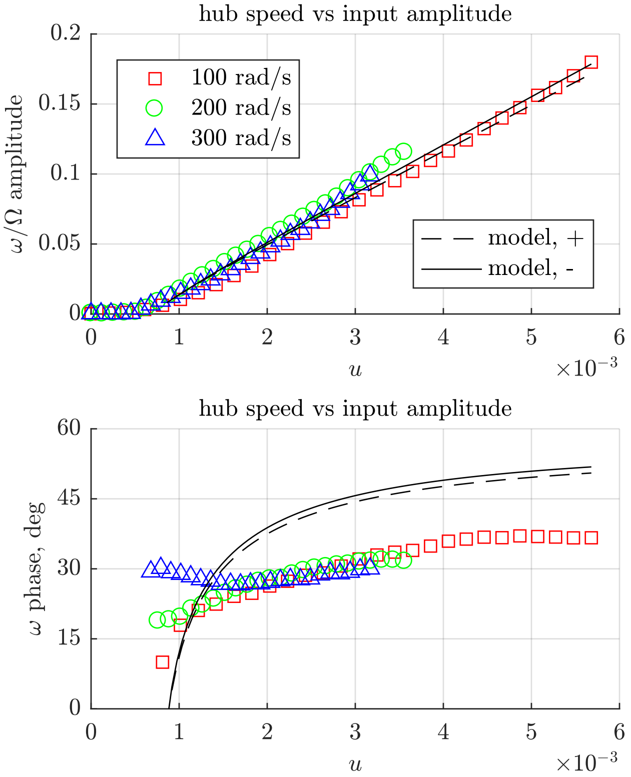

Figure 4.4: Measured hub speed response compared with model prediction for a range of normalized drive torque amplitudes u at three test speeds.

After a critical drive amplitude, the hinges free and the speed variation begins to grow with the applied voltage modulation. The iterative approach described in Section 3.6 for simultaneously solving the equation of motion and the amplitude parameters needed by the hinge damping model does a good job capturing this important nonlinearity in amplitude response, but the phase predictions are less accurate.

4.5 Lag Response

The lag response directly reveals the obtained cyclic pitch variation because the hinge geometry couples the lag and pitch angles. Blade lag angles for the positive coupling blade and negative coupling blade are determined by tracking AprilTag fiducial markers [57] attached to the tops of each blade root and the hub. Figure 4.5 collects measured lag angles for the positive coupling blade at different stations of the hub rotation over many operational

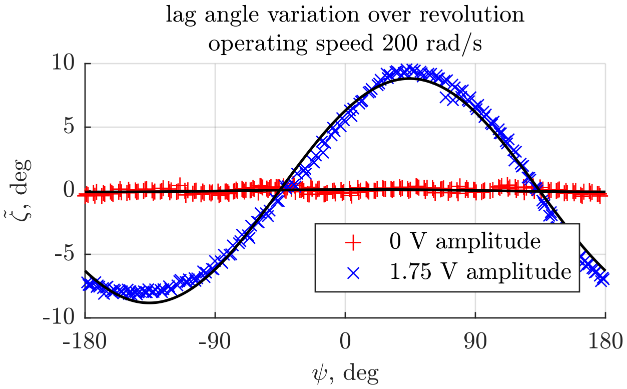

Figure 4.5: The cyclic lag angle response for the positive lag-pitch coupled blade is measured at an operating speed of 200 rad/s with and without an exciting voltage amplitude.

cycles at 200 rad/s, both with and without an excitation voltage. The first harmonic fit to the data is shown alongside the measurements. For this particular prototype the geometric lag pitch couplings $\Delta\theta/\Delta\zeta$ were -1 and +1, so the lag amplitude shown in Fig. 4.5 reflects the amount of cyclic pitch variation obtained. The measured lag or pitch angles are well described by their first harmonic, which means that the pitch changes over a revolution are very similar to those a traditional swashplate system would prescribe.

The lag response amplitude and phase are tabulated over a range of operating speeds and drive amplitudes in Fig. 4.6 for both the positive coupled and negative coupled blades. The model accurately predicts the amplitude of the lag-pitch response, and therefore the degree of cyclic pitch control achieved. The minimum drive amplitude in u needed to excite a lag response corresponds with the knee in the hub speed response of Fig. 4.4, and both features indicate the threshold for breaking static friction in the hinge. Below this drive amplitude the hinges are friction bound, the model does not apply, and the phase of a zero amplitude response is not meaningful. The measured phase of the lag response is in agreement with the model for large drive amplitudes. However, at small amplitudes of motion the equivalent damping model introduced in Section 3.6 may not accurately capture the more complex behavior of both static and dynamic friction. The sensitivity of cyclic pitch to cyclic voltage input shown by Fig. 4.6 is the effect exploited to initiate aircraft maneuvers by approximating cyclic pitch commands.

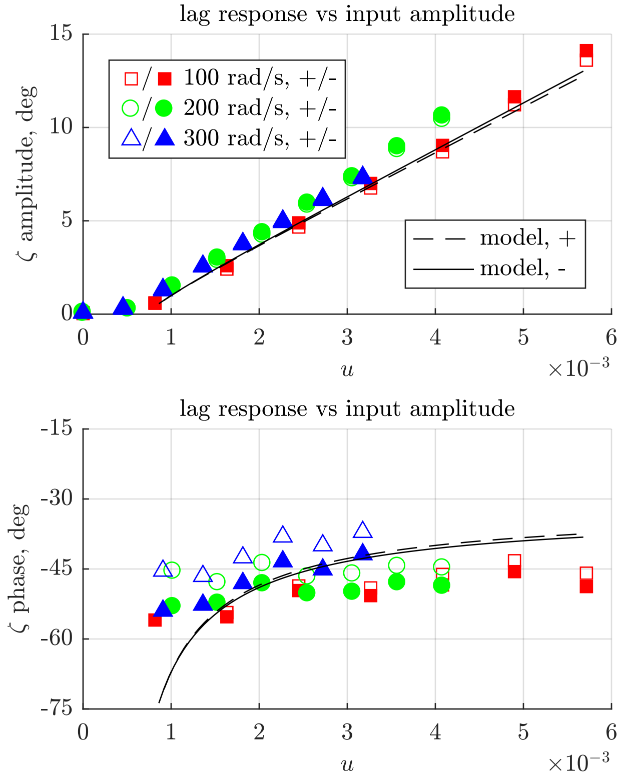

Figure 4.6: Measured blade lag angle response compared with model prediction at three speeds for both the positive and negative lag-pitch coupling blades.

4.6 Flap Response

The ultimate objective of the cyclic system is to drive a coherent blade flapping response as a facsimile of conventional cyclic controls. Gross changes in the tip path plane are readily observed during testing. Figure 4.7 illustrates one half revolution of the propeller with a series of stroboscopic images showing the blade flap motion. Previous experiments with a similar rotor but lacking a flap hinge qualitatively displayed blade bending and higher harmonics in the blade tip flapping motions when observed in high speed video [60]. With the addition of a flap hinge, the flap motion is now concentrated at the hinge and the modeling assumption of rigid blades is appropriate. At the same time, the flap response now takes on the simple once-per-revolution character of a conventional articulated blade responding to cyclic pitch variations.

The degree of flapping is measured by tracking the orientation of fiducial markers on the front of the hub and blade grips in strobe photographs of the blade at different stations of the rotation. It is assumed that the flapping motion of the blade grips is representative of that of the blade as a whole – this assumption of rigidity is qualitatively supported by Fig. 4.7. Instead of physically rotating the test setup, the electronic modulation phase was rotated for each image. Figure 4.8 shows the flap angle response for the positive coupled blade through one revolution at an operating speed of 200 rad/s along with first harmonic fits to the measurements. As expected, the blade does not flap when no excitation voltage is applied. When a voltage amplitude of 1.75 V is applied, a smooth, first harmonic cyclic flapping response is obtained.

The flapping response phase and amplitude for both the positive and negative coupled blades are tabulated in Fig. 4.9 at a range of operating speeds and drive amplitudes. The positive and negative blades flap with approximately the same amplitude, but are approximately 180° out of phase with each other as required for a coherent tilting of the tip path plane as illustrated in the photographs of Fig. 4.7.

The model overestimates the flapping amplitudes by as much as a factor of two in spite of fairly accurate predictions for the blade pitch changes that aerodynamically drive that

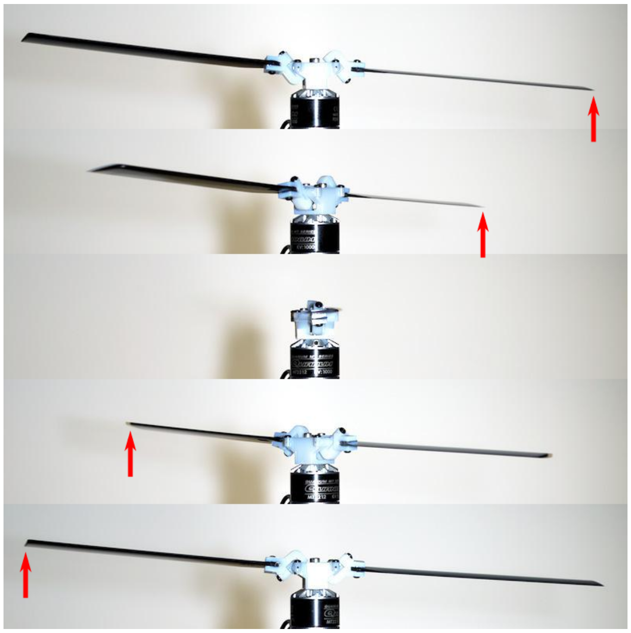

Figure 4.7: The positive coefficient blade begins on the right side at peak downward flap, and achieves maximum upward flap 180° later in the rotation.

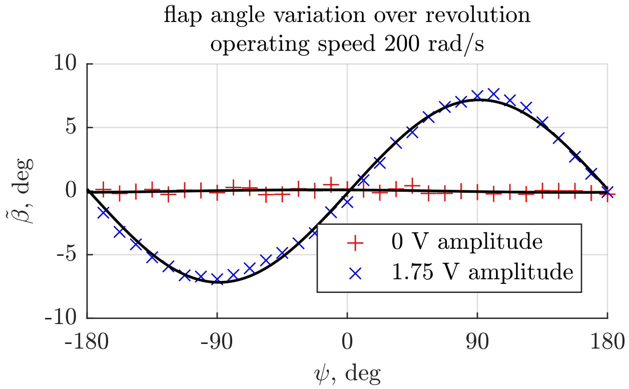

Figure 4.8: The cyclic flap angle response for the positive lag-pitch coupled blade is measured directly at a rotor speed of 200 rad/s with and without an exciting voltage amplitude.

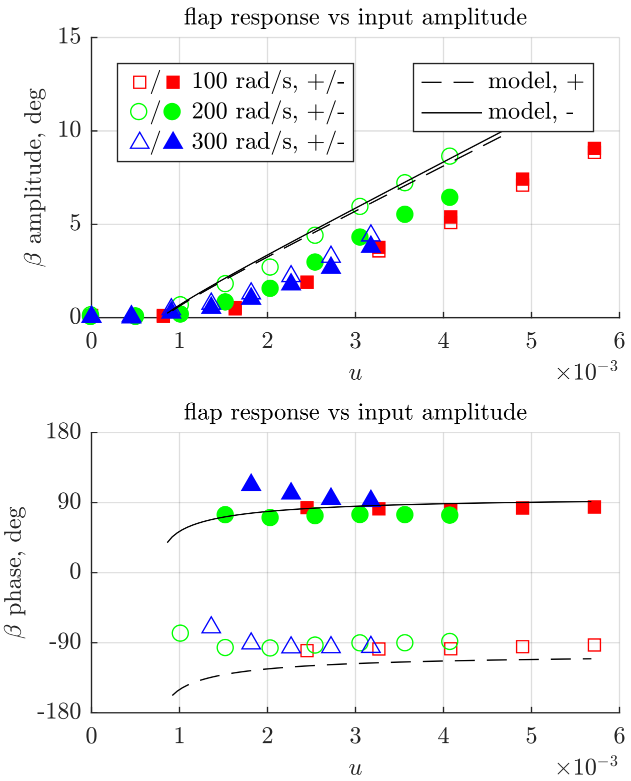

Figure 4.9: Measured blade flap angle response compared with model prediction at three test speeds. The positive coupling blade response is approximately 180° out of phase with the negative coupling blade.

response. A likely reason for the disagreement is that a fixed radial inflow distribution was assumed when deriving aerodynamic forces on the blades, but in practice the downwash is not rotationally symmetric during heavy cyclic operation. This effects a reduction in obtained aerodynamic loads which is often approximated by a lift deficiency function with typical values near 0.5 for moment changes near hover [33]. Incorporating this effect into the model is expected to reduce the predicted aerodynamic loads and bring the predicted flapping response more in line with measurements.

Chapter 5

Scaling

Mechanical swashplate control systems have been successfully deployed in vehicles as small as the 16 g Black Hornet and as large as a 56 000 kg loaded Mi-26 transport helicopter. A natural question arises as to whether the dynamic cyclic approach has similar scalability. This chapter discusses the impact of rotor size and operating speed as anticipated by dimensional analysis and the modeling effort in Chapter 3. A small 10 cm diameter rotor and large 1 m rotor provide experimental validation of those trends. Practical design and technology constraints are also considered. The discussion and experimental results of this section were originally prepared for [65].

There are several interrelated facets of the scale problem spanning rotor design and vehicle integration. How do we design dynamically-similar rotor experiments, and how do we extrapolate isolated rotor test results across differences in scale and operating speed? In the context of aircraft design, what are the consequences of varying rotor size and speed for a fixed aircraft? Finally, what are the general scaling characteristics when the dynamic cyclic system is applied to conceptual aircraft across vastly different scales?

Given the historical importance of scale model testing to the design and development process in aerospace, the subject has received a great deal of attention. The proper application of scaling analysis depends on the purpose of the study. This is why we find Mach number and Reynolds number similarity emphasized when interpreting isolated rotor tests

[29], [81], but Froude number is of great importance to vehicle flying qualities [2], [39], [49], [87], and power considerations can give direct insight into vehicle design [34], [43]. For this reason the appropriate framework of assumptions shifts while consideration of each of the three motivating questions in turn.

5.1 Isolated Rotor Scaling

Isometric scaling is an seemingly obvious requirement for discussing the scaling behavior of an isolated rotor; we frequently wish to consider a family of rotors which have similar geometry but differ in absolute size. A more significant property is to have strict scaling in the dynamic behavior. A set of dynamically similar experiments at different scales can all be described by one single nondimensional equation of motion. The design of such experiments must simultaneously consider both the model construction and also the operating condition. Dynamic similarity is required to conduct meaningful scale model testing. It allows us to extrapolate motions and forces from one isolated test stand experiment or numeric simulation to a continuous family of similar rotors both large and small.

5.1.1 Prescriptive Requirements for Dynamic Similarity

This section develops specific prescriptive requirements for dynamic similarity between rotors which may be used to guide the design of experiments, and it comments on the consequent scaling of physical quantities in the blade response. A treatment of aeroelastic helicopter blades by Hunt based on dimensional analysis identifies nine relevant independent variables governing the rotor involving three physical units (mass, length, and time). Therefore, the Buckingham Pi Theorem permits the selection of six governing nondimensional parameters. Conventionally, these are the Reynolds number, Mach number, Froude number, advance ratio, ratio of aerodynamic to inertial forces (Lock number), and ratio of aerodynamic to elastic forces [29]. It is in fact generally infeasible to maintain similarity across all six parameters, and this particular list is neither unique, necessary, nor exhaustive for all purposes.

We can obtain specific criterion for achieving similarity in dynamic cyclic rotors directly from the governing equations of motion derived in Chapter 3. In developing those equations we selected dimensional normalizing factors for inertia, length, and angular rate listed in Table 5.1.

Table 5.1: Characteristic scales for nondimensionalization.

quantity	normalized by
inertia	I_β
length	R
angular rate	Ω

This basis spans the salient fundamental units of mass, length, and time for our problem if we postpone discussion of the electric motor's operation. These three parameters disappear from the equation of motion after normalization, leaving 15 independent parameters to consider governing Eq. 3.56. For strict dynamic scaling the values of these 15 nondimensional parameters or parameter groups must be preserved. Table 5.2 collects these parameters in order of consideration to design properly scaled experiments.

Table 5.2: Nondimensional parameter groups.

variables	quality
e, l, k, θ_0, σ, N_b, $\frac{\Delta\theta}{\Delta\zeta}$	geometry
X_{I_h}	ratio of inertias
a, c_{d_0}	aerodynamics
γ	ratio of aerodynamic to inertial forces
c_ζ, c_β	structural damping
$\frac{k_m}{I_\beta\Omega^2}$, $\frac{c_m}{I_\beta\Omega}$	motor and controller

The numerous geometric parameters are preserved simply by maintaining geometric similarity between rotors.

Combining isometric scaling with constant mass density will also preserve the inertia ratio X_{I_h} between the hub inertia and the blade flap inertia. In practical applications, motors are selected based on the application's torque demands and not something as arbitrary as the motor's physical size. Consequently, maintaining the inertia ratio for dynamically similar experiments requires a different kind of care in physical motor selection or contrivances such as adding inertial masses to the hub.

The impact of aerodynamics have been summarized by a simple linear aerodynamics model incorporating a lift curve slope a and drag coefficient c_{d_0}. In addition to the airfoil geometry, these parameters are in general dependent on the local Reynolds number, Re, describing the ratio of inertial forces to viscous forces in the flow and the Mach number, Ma, describing the ratio of the flow speed to the speed of sound in the fluid medium. For testing in air at atmospheric pressure it is not possible to simultaneously preserve both Reynolds number and Mach number [29]. However, the lift curve slope is relatively insensitive to small changes in Reynolds number except at very low values, and variations in the drag coefficient are of secondary importance to the system dynamics. If desired, equal Mach numbers are easily obtained by operating at equal tip speeds, but these rotors operate far below their critical Mach number and so variations due to Mach number are small. Consequently, at this level of modeling detail, it is fairly reasonable to consider a and c_{d_0} to be independent constant values associated with the airfoil geometry.

The ratio of aerodynamic to inertial forces on the blade appears in the equations of motion as the Lock number, γ. If geometric similarity, constant mass density, and aerodynamic similarity have been preserved then the Lock number too will be preserved.

Structural damping effects in this model are lumped parameters associated with the hinges. The derivation of the energy equivalent nondimensional damping coefficients c_ζ and c_β in Eq. 3.37 and Eq. 3.35 show these parameters remain constant under isometric scaling assuming constant material friction coefficients.

Finally, the virtual damping and stiffness afforded by the motor and motor controller described by nondimensional parameters k_m and c_m must be held constant for proper dynamic scaling. The expression for these parameters in Eq. 3.46 show them to be functions of both the motor's physical properties (electromotive force constant K_e and resistance R_{ohm}) and the freely chosen software control gains (proportional gain K_P and integral gain K_I). As a result, the critical parameters k_m and c_m can be maintained by applying the correct software gains.

The above nondimensional parameters differ slightly from those identified by Hunt [29].

Since the present analysis considers the near hover condition, the advance ratio is always zero. We additionally do not model gravitational forces on the blade, so the Froude number is irrelevant. If the weight of the blades were to significantly change the coning angle this might be questioned, something possible at artificially low thrust levels. Finally, this model does not incorporate structural elastic effects since the blades are rigid and the hinges have no intrinsic spring stiffness. On the other hand, we explicitly model structural damping through the hinge losses, an effect that is often ignored.

5.1.2 Extrapolation Across Scale and Speed

Having specified criterion for dynamic similarity, we can observe trends in the response of similar rotors at differing size or operated at different speeds. For the moment we will ignore variations in the Reynolds number and Mach number and instead assume a and c_{d_0} remain constant. Table 5.3 associates dimensional quantities such as length or torque with the dimensional basis used to normalize them in the equation of motion, a function of length R, angular rate Ω, and flap inertia I_β. The inertia scales as R^5 under isometric scaling with constant material density, and so for similar rotors these quantities are shown to grow in proportion to products of powers of the rotor radius R and operating speed Ω.

Table 5.3: Dimensional basis and isometric scaling result for model quantities.

quantity	normalized by	isometric scaling
length	R	R
mass	$I_\beta R^{-2}$	R^3
inertia	I_β	R^5
time	Ω^{-1}	Ω^{-1}
angular rate	Ω	Ω
force	$I_\beta \Omega^2 R^{-1}$	$R^4\Omega^2$
torque	$I_\beta \Omega^2$	$R^5\Omega^2$

Table 5.3 shows that torques grow with the square of operating speed and to the fifth power of radius. In particular the aerodynamic drag torque, and therefore the mean motor torque, grow as $R^5\Omega^2$. This is the conventional result which motivates defining torque and power coefficients for propellers. This result extends to the dynamic rotor response to torque

modulation. The amplitude of the motor torque modulation must grow commensurate with the motor drag torque as $R^5\Omega^2$ in order to obtain a similar response in terms of pitch variation or flap angle. Of course, the ultimate useful pitching torque obtained will also rapidly grow as $R^5\Omega^2$. As a result, larger or faster rotors obtain larger useful pitching moments at the expense of proportionally larger drive torques.

The time scale of the transient dynamic response is also of interest; it limits how rapidly the amplitude or azimuthal phase of the rotor response can be varied to pitch or roll the aircraft. Within the linear and time invariant model framework, a metric for this response time is given by calculating the inverse of the real part of the system poles. For similar rotors the transient decay time constant increases proportional to $1/\Omega$, so faster spinning rotors are capable of affecting more rapid changes in roll or pitch commands, independent of size.

5.1.3 Experimental Confirmation

Prototype Construction

Two prototype rotors with diameters of 10 cm and 1 m were constructed. These prototypes were designed to be dynamically similar in the sense described in Section 5.1.1. The smaller 10 cm rotor depicted in Fig. 5.2 incorporates a 3.1 g AP03 brushless motor driven by a custom motor controller. The blade elements are 12 % thick flat plates with a cord of 5.6 mm constructed from pultruded carbon fiber. The hub is 3D printed from a photo cured resin, and the hinges are constructed from stainless steel pins in plain bores with PTFE thrust washers. Visible in the photograph of Fig. 5.2 are AprilTag fiducial markers [57] used for visual tracking of the blade motions during experiments. Rotor dimensions and properties are summarized in Table 5.4 and Table 5.5.

The larger 1 m rotor is driven by a 1280 g T-Motor U13 brushless motor with a custom logic controller driving the power stage of a commercial off-the-shelf hobby grade electronic speed controller. The blade elements are 10 % thick flat plates with rounded edges with a cord length of 56 mm machined from acetal plastic. The hub and blade grips are machined

Table 5.4: Rotor assembly properties.

parameter	symbol	small	large
tip radius	R	5 cm	50 cm
blade chord	c	5.9 mm	59 mm
blade mass	m	0.39 g	362 g
flap inertia	I_β	1.8×10^{-7} kg m^2	1.7×10^{-2} kg m^2
total hub inertia	-	5.2×10^{-8} kg m^2	5.1×10^{-3} kg m^2

Table 5.5: Motor properties.

parameter	symbol	small	large
emf constant	K_e	0.0025 V/(rad/s)	0.11 V/(rad/s)
resistance	R_{ohm}	1.4 ohms	0.24 ohms
motor rotational inertia	-	3.9×10^{-8} kg m^2	1.0×10^{-3} kg m^2

Table 5.6: Nondimensional Parameters.

parameter	symbol	small	large
hinge eccentricity	e	0.09	0.09
blade radius of gyration	l	0.426	0.435
blade radius of oscillation	k	0.607	0.624
rotor solidity	σ	0.0746	0.0746
collective pitch	θ_0	9°	8°
lag-pitch coupling	$\frac{\Delta\theta}{\Delta\zeta}$	1	1
hub inertia ratio	X_{I_h}	0.147	0.148
lift curve slope	a	6.28	6.28
drag coefficient	c_{d_0}	0.06	0.06
Lock number	γ	1.56	1.61
structural lag damping	c_ζ	0.0751	0.0899
structural flap damping	c_β	0.0381	0.0385
drive induced stiffness	$\frac{k_m}{I_\beta \Omega^2}$	9×10^{-5}	9×10^{-5}
drive induced damping	$\frac{c_m}{I_\beta \Omega}$	9×10^{-2}	9×10^{-2}

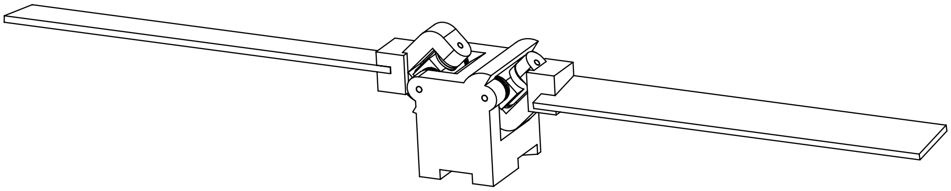

Figure 5.1: 10 cm diameter rotor.

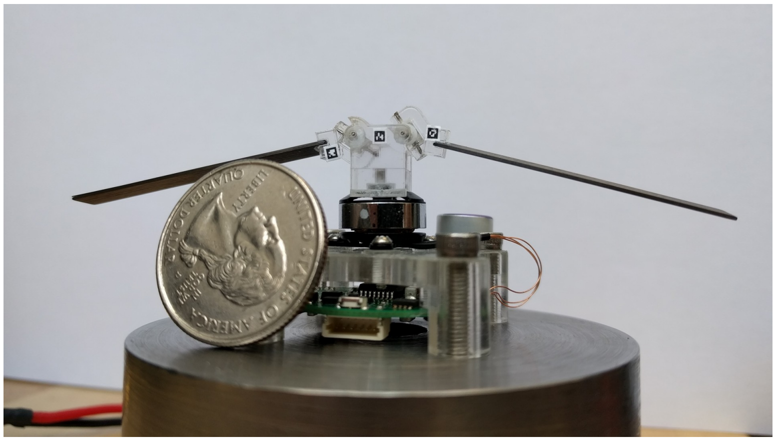

Figure 5.2: 10 cm diameter rotor with motor and motor controller.

from aluminum and use sintered bronze flanged bushings to support 0.25 in diameter stainless steel hinge axles. The photograph of Fig. 5.4 shows the power stage used to drive the motor along with the 1 m prototype. Figure 5.5 displays the AprilTag fiducials used during experiments and an inertial fly bar added to establish dynamic similarity between the large and small rotors by accounting for the inherent difference in the motor inertias.

Cyclic Experiments

A set of test stand experiments was undertaken to establish the validity of the dynamic model for both a 10 cm and 1 m diameter rotor as well as verify the expected scaling trends.

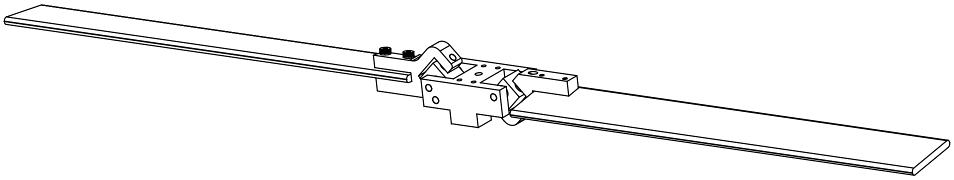

Figure 5.3: 1 m diameter rotor.

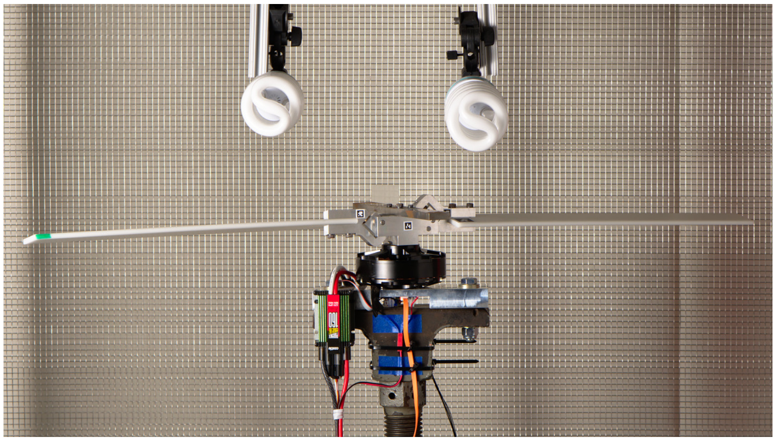

Figure 5.4: 1 m diameter rotor on test stand with motor and motor controller.

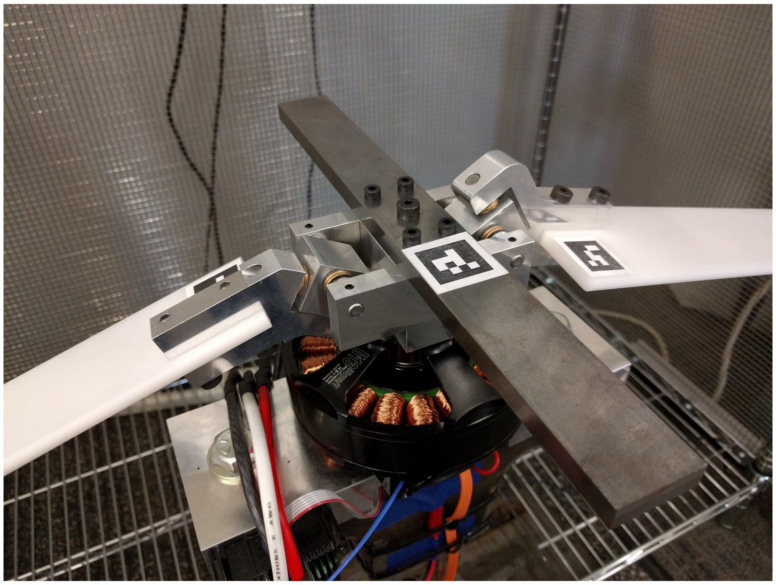

Figure 5.5: 1 m diameter rotor with inertial flybar and fiducial markers.

Figures 5.6 and 5.7 depict the hub speed variation response to changes in the normalized drive voltage amplitude u at several different test speeds from approximately 300 RPM to 9000 RPM. Since these rotors have been designed and operated to be dynamically similar the model prediction curves are very similar for both rotors when plotted nondimensionally. The first set of plots shows the amplitude of the hub speed response to a range of input voltage amplitudes. There is a knee in the response at low amplitude for both rotors where static friction is broken, and then a linear growth in the response closely adhering to the model prediction. At high drive amplitudes the response flattens out, which correlates with the blade audibly hitting hitting hard kinematic stops during the experiments. The second plot shows for the same experiments the phase of the hub speed response relative to the phase of the input sinusoid. There is again a strong nonlinear distortion at low amplitude due to friction and then convergence towards a fixed value at higher amplitudes. At high amplitudes the measured phase response adheres to the model within approximately 10°. The degree to which the data taken at very different speeds and on very different scales overlays on the nondimensional plot verifies the utility of the nondimensional dynamic model.

The blade lag response may be taken as a direct proxy for the cyclic blade pitch response since for these models the lag pitch coupling coefficient was kinematically determined to be unity. As a result, Figs. 5.8 and 5.9 showing the lag response to changes in input drive voltage amplitude may be read as depicting the cyclic blade pitch obtained by this rotor system. Once again both the large and small rotors at both high and low speeds show a low amplitude knee associated with static friction, after which a linear growth in the blade pitch response begins. There is more evidence of the blades hitting the hard kinematic stops for the highest drive amplitudes in both both the small and large rotor. In high speed tests the rotors were not driven much beyond this point due to thermal limits in the small rotor and risk of shock damage to the large rotor. In these experiments both the 10 cm and 1 m diameter propeller were driven up to a cyclic pitch amplitude of approximately 10°. There is notably more variation in the experimentally obtained response phase as well as a larger discrepancy with respect to the model of up to 30°. Some of this is an expected accumulation

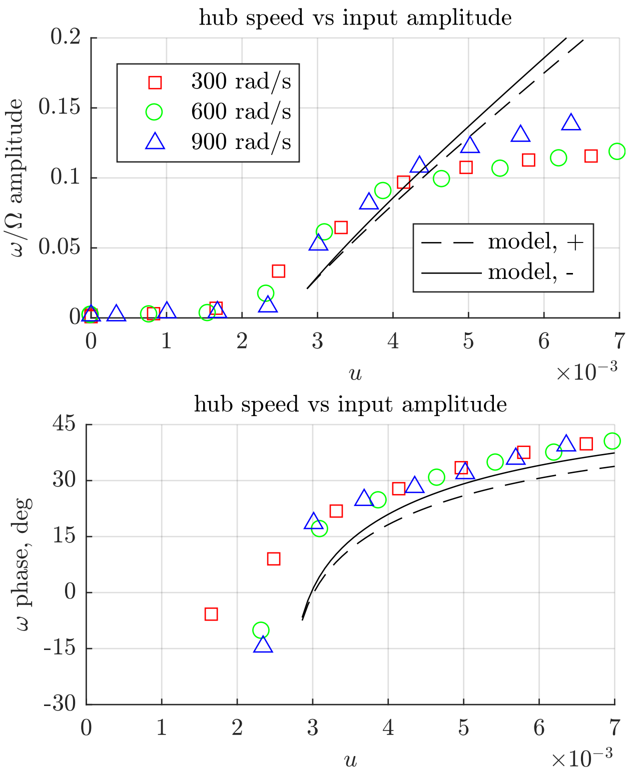

Figure 5.6: Hub speed response in small rotor.

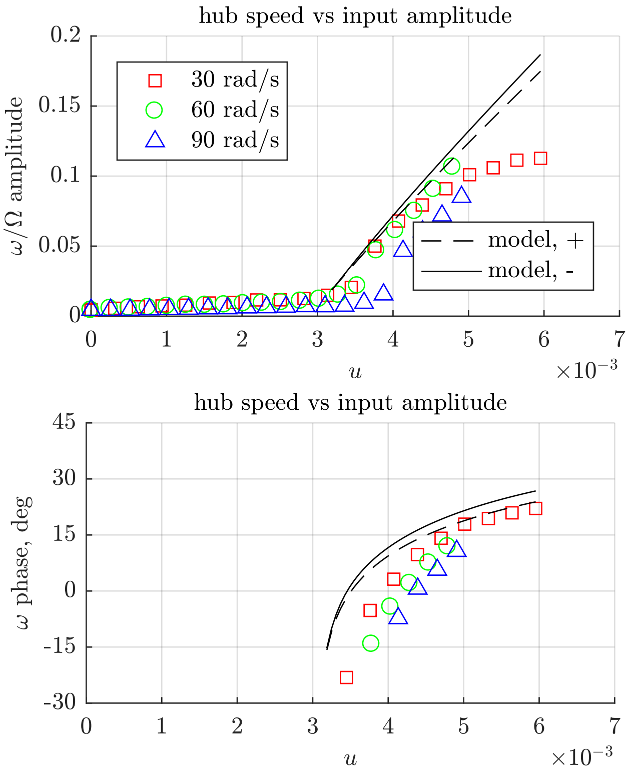

Figure 5.7: Hub speed response in large rotor.

of modeling errors as the measurements become further removed from the input signal. For example, it should not be surprising that if the hub speed response has more phase delay than expected, the lag response will as well. At the same time, it is likely that limits in the timing accuracy of the photographic measurement method or unmodeled system delays affect the phase determination in the highest speed tests, resulting in increasing apparent phase delay at high operating speed.

The flapping response for the small and large rotors are depicted in Fig. 5.10 and 5.11. The response amplitude is once again significantly overestimated by the model as previously shown in Fig. 4.9, which is an expected result of neglecting to model the nonsymmetric inflow distribution obtained during constant heavy cyclic. There is a small unmodeled difference in the observed flap angles between the positive and negative coupled blades in the small rotor, while there is not a corresponding difference in the lag response for the same rotor. Flapping is forced by aerodynamic lift, and our aerodynamic model for these particular rotors is much more uncertain than their inertial properties. One possible explanation is that the two blades are experiencing the onset of stall differently due to unintentional differences in their shape or trim posture. The rotor airfoils are simple flat plates operating at low Reynolds number in these experiments which makes them very sensitive to test conditions. In addition, no attempt was made in these experiments to maintain Reynolds similarity across tests. The large rotors tests show a different unexpected result, which is that the mid-speed test at 60 rad/s consistently yield proportionality higher response amplitudes than the low-speed or high speed tests. This may be due to an unmodeled structural resonance. The acetal blades are moderately flexible and have a nonrotational natural flapping frequency of 64 rad/s in cantilever from the blade grips, which is close to the operating frequency of 60 rad/s. In general, introducing structural stiffness into the model breaks dynamic similarity across operating speeds because the flapping frequency ratio becomes speed dependent, and this may explain the result shown here. Nevertheless, the agreement between the high and low speed tests far from resonance is very good, which suggests the broad scaling trends implied the the nondimensional equations remain useful.

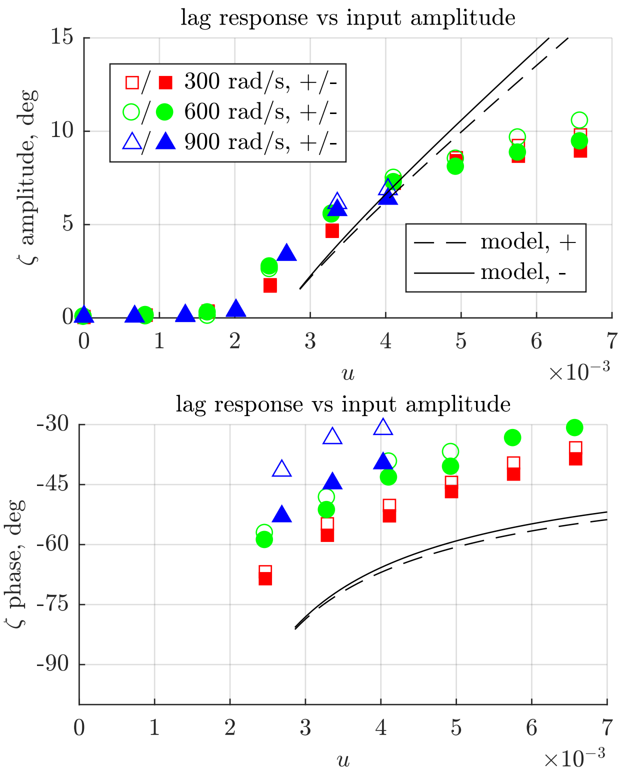

Figure 5.8: Lag (pitch) angle response in small rotor.

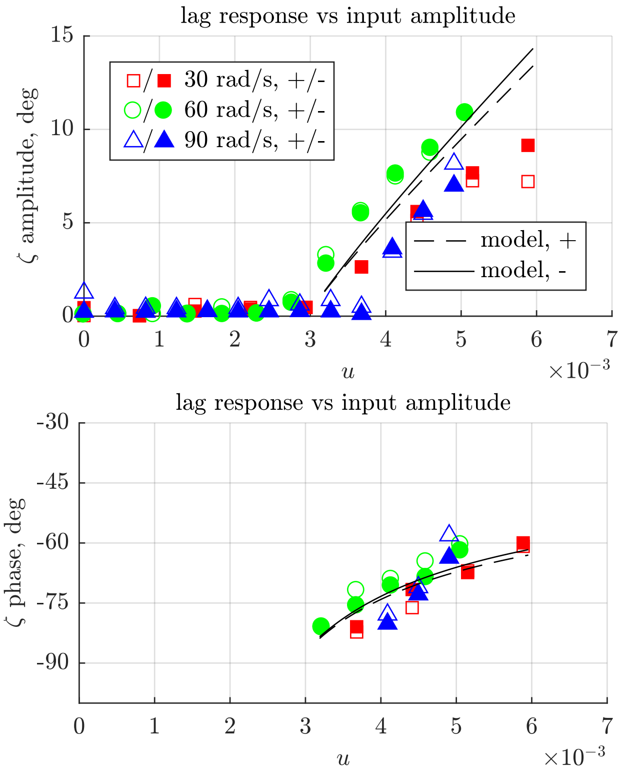

Figure 5.9: Lag (pitch) angle response in large rotor.

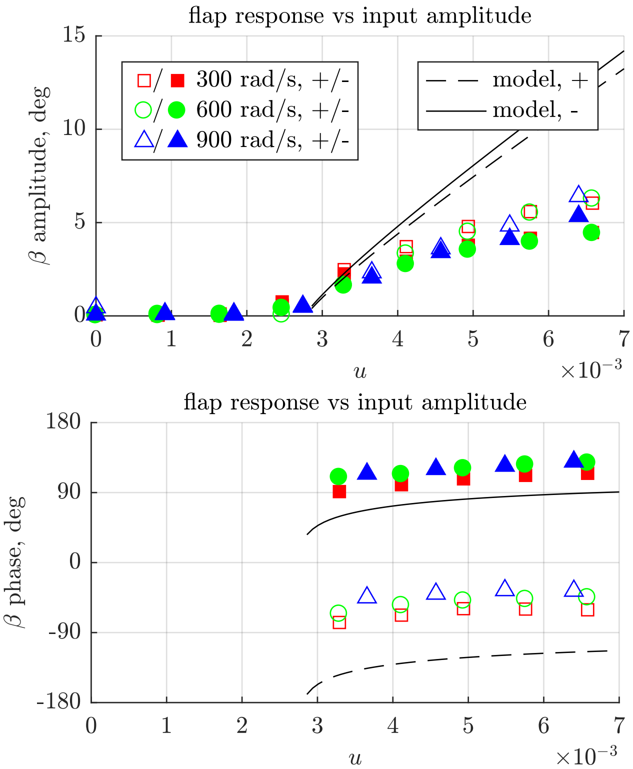
flap response vs input amplitude

flap response vs input amplitude

Figure 5.10: Flap angle response in small rotor.

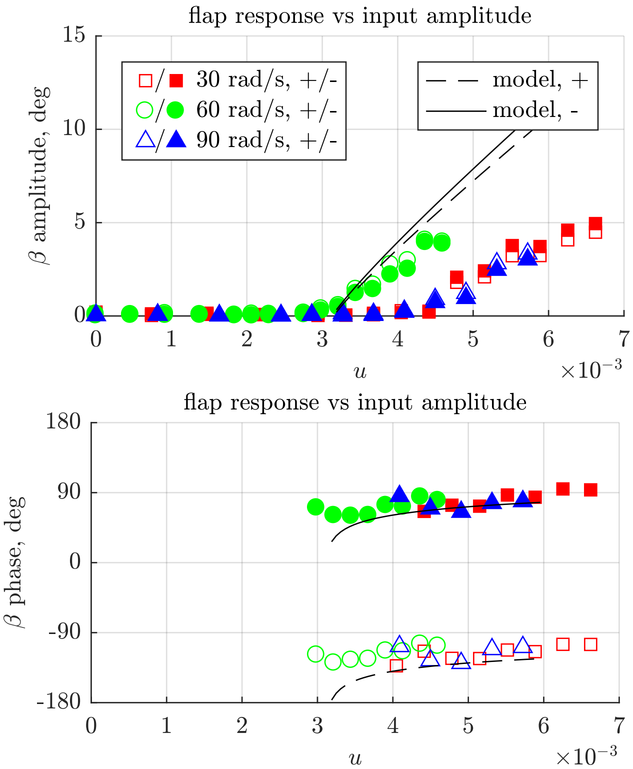
flap response vs input amplitude

flap response vs input amplitude

Figure 5.11: Flap angle response in large rotor.

5.2 Impact of Rotor Size

Rotor sizing is an important part of aircraft design. This section will no longer suppose the kind of arbitrary changes to rotor size or operating speed possible in synthetic test stand experiments. Instead we will consider the impact of moderate changes in rotor size for a given aircraft with a fixed hover thrust requirement. From Table 5.3 in the previous section we saw that the thrust force is proportional to $R^4\Omega^2$, so to maintain a constant thrust with similar rotors the speed must change in proportion to the inverse square of radius, holding $R^2\Omega$ constant. We can recast Table 5.3 to show how the rotor dynamic quantities scale under this new constraint.

Table 5.7: Scaling at constant thrust.

quantity	scaling
length	R
mass	R^3
inertia	R^5
time	R^2
angular rate	R^{-2}
force	1
torque	R

As before, the pertinent torques all scale together for dynamically similar operation. These include the motor's modulation amplitude torque, the useful pitching reaction torque, and the steady drag torque. In particular, the ratio of the motor's modulated torque amplitude to the resulting useful pitching reaction torque remains constant for different sized rotors when operated at the same thrust level and cyclic pitch variation. At the same time, in absolute terms, these torques increase with R.

Given two similar rotors operating at the same thrust level and same cyclic pitch variation, we should expect that the larger rotor generates larger pitching moments in proportion to R. Within a fully linear model framework, this implies that the larger rotor could be operated with a cyclic pitch variation of $1/R$ that of the small rotor in order to obtain the same same pitching moment effect. Note that this requires linearity to justify properly, and is not a generic scale argument. The required driving modulated torque amplitude then grows as $1/R \times R = 1$, independent of size. Changing rotor size while operating at fixed thrust does not change the modulated torque amplitude required to obtain a particular vehicle pitching moment.

Since the drag torque of the larger rotor grows as R while the torque modulation requirement remains constant, the torque modulation described as a percentage of the steady operating torque falls. As a consequence, the drive system for the larger rotor does not need to be oversized by as large a safety factor to tolerate pulsing operation.

The transient response time of the rotors slow as R^2, consistent with our understanding that operating a bigger rotor at the same thrust level implies a slower operating speed. The ability to manipulate the blade pitch through an azimuthal rotation of the hub is unaffected – but the rotor spins more slowly and so the effective bandwidth of vehicle control should be expected to fall off in a similar way to the trend in conventional helicopters with kinematic swashplate systems.

The trends developed in this section are useful for contemplating small changes to the nominal rotor size for a fixed aircraft. In practice, the weight of the rotor must factor into the rotor thrust requirement, so contemplating massive rotors on vehicles with a tiny thrust requirement is unreasonable. Likewise, it is not practical to speak of tiny rotors whose size approach zero and require impossibly large speeds. More fundamentally, requiring a fixed thrust from radically different size rotors preserves the Reynolds number ($Re \propto \Omega R^2 \propto 1$) but entails massive variation in the Mach number ($Ma \propto \Omega R \propto 1/R$). As a result, the assumption that dynamic similarity can be maintained for the rotor at all is highly questionable.

5.3 Impact of Vehicle Size

Finally we come to the question of technology selection. Is dynamic cyclic more or less suitable for very small or very large aircraft? In the previous section it was shown that holding thrust constant and increasing the rotor size reduces the proportional motor torque

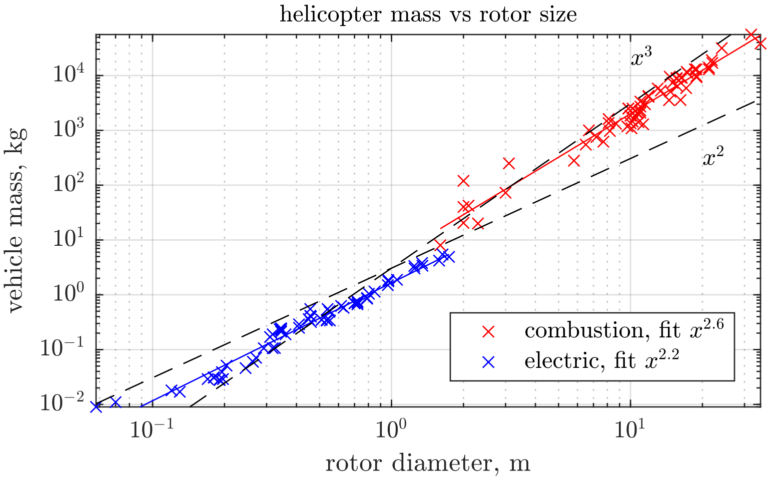

Figure 5.12: Production helicopter mass vs rotor diameter.

modulation requirements but also slows the response time. To look at trends across vehicle sizes, we need a presumptive rule to correlate vehicle mass (or thrust requirement) to rotor size and speed.

Figure 5.12 correlates helicopter mass and rotor diameter for a variety of electric and combustion engine aircraft across more than six orders of magnitude in weight. The manned aircraft data is taken from a previous survey [43] and the unmanned aircraft information is primarily sourced from marketing materials. The logarithmic plot displays quadratic and cubic growth trends for comparison. Generally speaking, helicopter mass grows with rotor diameter slower than isometric scaling would predict, $W \propto R^3$. Larger helicopters have proportionality larger rotors than isometric scaling would suggest. On the other hand, weight grows faster with rotor size than constant disc loading would predict, $W \propto R^2$. As a consequence, larger helicopters must operate at a higher ideal specific power than smaller helicopters on a watts-per-kilogram basis [43]. Separate best fit trends are shown for the exponent of growth for surveyed combustion helicopters ($R^{2.6}$) and electric helicopters ($R^{2.2}$).

Some caution must be exercised in interpreting this plot, as these aircraft represent a wide range in technologies and have been optimized for disparate missions. The data includes heavy transport helicopters at their maximum laden capacity right alongside unmanned electric sport aircraft. Perhaps this explains the apparent difference in weight growth exponent between the two vehicle classes. Electric sport helicopters all rely on the same technologies of lithium polymer batteries and electromagnetic motors and are designed to optimize flight performance with no payload, so their design may be constrained closer to a constant specific power curve by their constitutive technologies.

The majority of scaling analyses assume isometric scaling of the gross vehicle and rotor size together, with the result that the vehicle mass grows as R^3. Table Table 5.3 shows that the rotor's thrust force grows as $R^4\Omega^2$, so similar rotors will need to be operated such that $R\Omega^2$ remains constant in order to maintain the balance of aerodynamic to gravitational forces for the vehicle. This is Froude scaling applied to both the rotor and the vehicle dynamics. The consequences of this in terms of the magnitude of forces, torques, and time scales are shown in Table 5.8.

Table 5.8: Froude scaling for isometric vehicle and rotor growth.

quantity	isometric scaling
length	R
mass	R^3
inertia	R^5
time	$R^{1/2}$
angular rate	$R^{-1/2}$
force	R^3
torque	R^4

These results are identical the analysis of Froude scaling as a model for conventional helicopters given in [49], suggesting that the principle scaling factors relevant to conventional helicopters carry over to the dynamic cyclic system. In particular, larger helicopters are less agile as their rotor response times increase with $R^{1/2}$ and their body angular accelerations due to control torques decrease as $1/R$. Assuming these generic trends are satisfactory, the ratio of modulated torque to rotor drag torque and therefore the motor sizing safety factor needed to exercise dynamic cyclic remains constant.

5.4 Practical Limitations for Manned Helicopters

While the fundamental physics involved in dynamic cyclic control scales similarly to conventional swashplate cyclic systems, dynamic cyclic presents unique challenges for large scale or manned aircraft. The principle technological difficulty is in pulsing the drive torque on the hub at the rotor frequency. This is easy to do with electromagnetic drive motors whose torque response time is significantly faster than the rotor's rotational period. However, small manned helicopters typically employ reciprocating combustion engines and large, high performance helicopters rely on turboshaft engines [41]. A representative time constant describing the torque response to a step increase in fuel flow for the T700 turboshaft engine is 0.6 s and for a step decrease in fuel flow 0.8 s [3]. As a result, torque modulation at a characteristic rotor frequency near 300 RPM (5 Hz) is impractical [21]. As a result, either an alternative propulsion method such as electronic motors or some auxiliary modulation actuator would be required. All-electric helicopters remain an open area of research bringing their own difficulties, and the introduction of additional actuators reintroduces some of the complexity one hopes to avoid by removing the swashplate system.

Safety and redundancy challenges associated with implementing dynamic cyclic are perhaps a more fundamental barrier to using laboratory scale MAV as a literal blueprint for manned aircraft. Conventional manned helicopters incorporate collective blade pitch control in addition to cyclic blade pitch control, which allows them to exploit autorotation for a controlled descent in the case of engine failure. Since the present system does not incorporate collective blade pitch control it can not autorotate safely in this manner. Perhaps more importantly, a conventional helicopter's attitude control is approximately decoupled from the thrust power plant, so the aircraft can maneuver with engine loss. In contrast, if a single electric motor is the sole actuator onboard, its loss leads not just to rapid descent but to complete loss of control.

Chapter 6

Flight Without a Swashplate

Most aircraft which might employ the dynamic cyclic rotor require closed loop position and attitude controllers for practical flight operations. This chapter develops the control framework for coaxial helicopters which use cyclic control on the top rotor, and is excerpted from the author's work in [61]. Flight experiments were conducted on a coaxial helicopter which relies exclusively on the dynamic cyclic rotor for attitude control. The system level performance of this hardware and the cascaded control architecture were observed in terms of trajectory tracking capabilities and transient response to step commands. Additionally, in-flight power measurements were obtained for a variety of payload weights and positions which strained the rotor's control authority. Finally, augmenting a children's toy helicopter to exhibit torque induced cyclic control provides a concrete example of how simple an operational system can be.

6.1 Coaxial Helicopter

The novel cyclic control method permits a very simple mechanical design for the complete MAV, as shown in Fig. 6.1. The vehicle has a 30.0 cm diameter top rotor, stands 16.3 cm tall, and has a flying weight of 227 g. It is comparable in scale to the conventional coaxial Blade CX2 used in [26], [16] which has a 34.5 cm rotor diameter, a height of 18.4 cm, and an identical flying weight of 227 g.

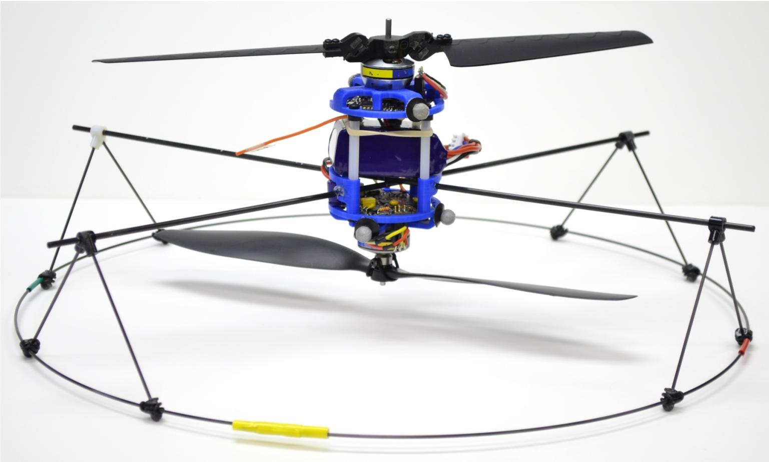

Figure 6.1: A 227 g coaxial MAV exhibits cyclic control without a swashplate or any additional actuators.

The hinged control rotor is directly mounted to the top motor, pointed upwards. A rigid rotor is mounted to the bottom motor, which is inverted to place the rotor at the bottom of the vehicle. This arrangement has been used in the past to avoid the complexities of hollow shaft, concentric drive systems [25], [80]. A bottom rotor guard ring and landing gear supports the vehicle, enabling free takeoff and landing. While this configuration is expedient, the bottom rotor might also be replaced by a tail rotor or a second top rotor in order to permit a suspended payload.

6.2 Electrical Design

A pair of identical custom avionics boards mounted at the rear of each motor support communication, inertial sensing, computation, and motor control. The electronics hardware for these controllers was designed by the authors of [67] and the software developed in collaboration. Onboard controllers are executed by a 32 bit microcontroller (STM32f373) running at 72 MHz. A 900 MHz low power transceiver (AT86RF212) enables half duplex communication at 250 kbits/s for command reception and transmission of flight data.

A hall effect encoder on the circuit board detects the orientation of a diametrically polarized magnet affixed to the bottom of the spinning motor shaft. This absolute position information is used to generate the three phase drive for the brushless motor, enabling both conventional steady commutation to spin the motor and synthesizing our once-per-cycle applied sinusoidal drive component.

An onboard inertial measurement unit (MPU6050 IMU) provides acceleration and rotation rate measurements at 250 Hz to the onboard attitude estimator and controller. Finally, onboard voltage and current sensing enables precise power measurements during maneuvers for offline evaluation. Presently only the top avionics board executes the flight controllers and state estimator, and the bottom avionics board acts as a simple I2C slave motor controller.

6.3 Control Rates and Timescales

The timescales and update rates of the cascaded communications and control system are summarized in Fig. 6.2. During maneuvers, thrust and desired attitude commands are received at 75 Hz. These may be direct commands from a human pilot, or autonomously generated in the motion capture environment. The onboard attitude controller updates at 250 Hz, generating motor commands expressed as a mean value, amplitude, and phase offset parameters. Output to the motor is based on these parameters and the motor's instantaneous mechanical orientation.

The sinusoidal component of the motor control needs to be synthesized smoothly even as the propeller spins at approximately 40 Hz. At this speed, the normal three phase electrical commutation frequency is approximately 280 Hz (the motor has seven pole pairs). In comparison, synthesis of the 40 Hz superimposed sinusoid we require does not represent

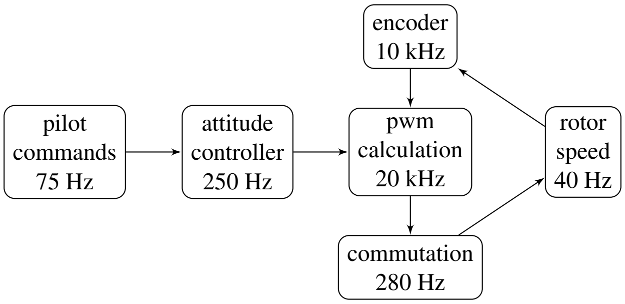

Figure 6.2: Representative frequencies. The attitude control rate is decoupled from both the rotor speed and PWM synthesis of the pulsing torque.

an unusual burden. The motor outputs are updated at the 20 kHz pulse width modulation frequency based on position estimates from the absolute encoder, which updates internally at 10 kHz. The driver circuitry and the motor itself are completely conventional. The critical aspect of these control layers is that the generation of the pulsing torque which enables cyclic control is abstracted from the attitude controller as mean value, amplitude, and phase parameters. This strongly decouples the attitude controller rate from either the propeller speed or the motor drive update rate.

6.4 Attitude Control

Automated trajectory tracking is achieved with a nested inner attitude controller and outer position and velocity tracking controller. This follows the common approach of cascading controllers for trajectory tracking [48] or path following [16] tasks. The inner attitude controller onboard the vehicle is depicted in Fig. 6.3.

Onboard the vehicle, an unscented Kalman filter following [37] forms an estimated orientation quaternion $\hat{\mathbf{q}}$ and angular velocity vector $\hat{\boldsymbol{\omega}}$ based on measurements from the onboard IMU. Our controller employs a nonlinear attitude tracking controller operating directly on quaternions as in [86], which is widely practiced. A desired body moment vector $\mathbf{u}$ is computed from the estimates $\hat{\mathbf{q}}$, $\hat{\boldsymbol{\omega}}$ and the desired orientation and angular velocities $\bar{\mathbf{q}}$, $\bar{\boldsymbol{\omega}}$ based on an orientation error vector $\mathbf{e}_R$ and angular rate error vector $\mathbf{e}_\omega$ with diagonal gain matrices K_R and K_w.

$$\mathbf{u} = -K_R\mathbf{e}_R - K_w\mathbf{e}_\omega \tag{6.1}$$

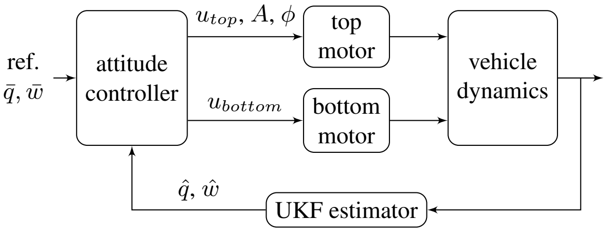

Figure 6.3: The controller operates on an estimated orientation and angular rate ($\hat{q}$, $\hat{w}$) and desired values ($\bar{q}$, $\bar{w}$). Outputs are mean drive voltages u_{bottom}, u_{top} and an additive sinusoidal component of amplitude A and phase ϕ.

The angular rate error vector is intuitively defined.

$$\mathbf{e}_\omega = \hat{\boldsymbol{\omega}} - \bar{\boldsymbol{\omega}}. \tag{6.2}$$

To form the orientation error vector $\mathbf{e}_R$, we consider the error quaternion $\mathbf{q}_e = \bar{\mathbf{q}}^*\hat{\mathbf{q}}$ whose real and scalar parts $\mathbf{q}_e = (\cos(\theta/2), \mathbf{v}\sin(\theta/2))$ describe a rotation of θ radians about a unit vector $\mathbf{v}$. We define the error vector $\mathbf{e}_R = \sin(\theta/2)\mathbf{v}$ by extracting the vector part of the error quaternion.

$$\mathbf{e}_R = \text{sign}(s)\mathbf{x}, \text{ given } \mathbf{q}_e = (s, \mathbf{x}) \tag{6.3}$$

As noted in [38], this bears a resemblance to an alternative matrix formulation suggested in [40].

$$\mathbf{e}_R = \frac{1}{2}(R_d^T R - R^T R_d)^\vee \tag{6.4}$$

A similar geometric interpretation is aided by Rodrigues' formula: if the error rotation is a rotation of θ radians about the unit vector $\mathbf{v}$, then $\mathbf{e}_R = \sin(\theta)\mathbf{v}$. However, we prefer to work uniformly with the quaternion representation of (6.3).

In the new vehicle, the calculated control vector $\mathbf{u}$ and a commanded thrust voltage f determine the top rotor mean drive voltage u_{top}, bottom rotor mean drive u_{bottom}, top rotor pulsing amplitude A, and top rotor pulsing phase ϕ. Collective increase and decrease of u_{bottom} and u_{top} increases and decreases net thrust. A differential between u_{bottom} and u_{top} affects a differential torque between the counter rotating propellers and yaws the vehicle. Pitch and roll corrections are achieved through the sinusoid amplitude A and phase angle ϕ which are determined by the magnitude and direction of the desired in plane control moment vector $\{u_x, u_y\}$. In practice the amplitude A is modified to eliminate a deadband value A_0

below which no cyclic oscillation is excited.

$$u_{bottom} = f + u_z \tag{6.5}$$

$$u_{top} = f - u_z \tag{6.6}$$

$$A = \sqrt{u_x^2 + u_y^2} + A_0 \tag{6.7}$$

$$\phi = \mathrm{atan2}(u_y, u_x) \tag{6.8}$$

This very simple mapping from $\{f,\ \mathbf{u}\}$ to $\{u_{bottom},\ u_{top},\ A,\ \phi\}$ achieves adequate performance near trim. A fixed calibration offset θ_0 relates the blade attachment angle to the rotation sensor and airframe. The final applied voltages are based on the instantaneously measured rotor position θ.

$$V_{bottom} = u_{bottom} \tag{6.9}$$

$$V_{top} = u_{top} + A\cos(\theta - \theta_0 - \phi) \tag{6.10}$$

6.5 Trajectory Tracking

The two motor system is capable of tracking 3D reference trajectories through space while independently regulating the heading orientation, making these vehicles suitable for a variety of camera pointing or precision delivery and retrieval tasks. In this respect the cyclic system maintains the advantage of quadrotors and swashplate systems over the many fixed wing, ornithopter, and toy helicopter systems which can not reject lateral positioning disturbances without turning.

A 20 cm lateral step in desired position excites a roll response and position correction as shown in Fig. 6.4. In the figure, the thin line marks the instantaneous step in desired position and the data points reflect the true motion capture measurements. During this brief maneuver the vehicle attains a maximum roll angle of 9° and speed of 0.47 m/s. Such a side step motion resembles the attitude controller response to a lateral double shown in [16] for a similar scale conventional coaxial helicopter.

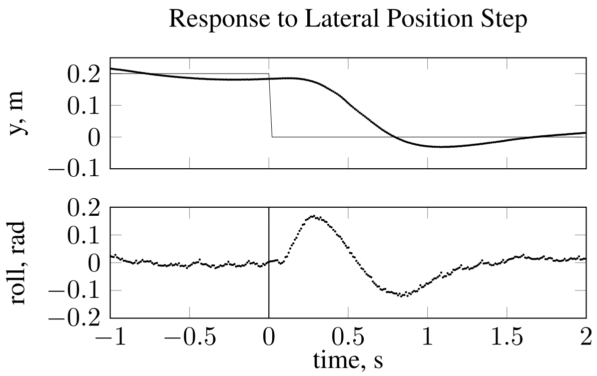

Figure 6.4: A 20 cm step in desired position towards the right results in a roll response and corrective lateral motion.

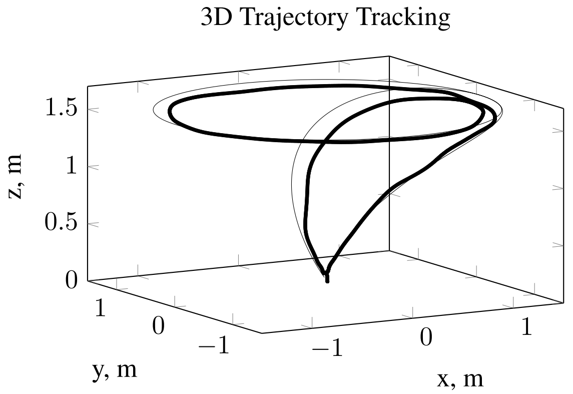

Figure 6.5: Automated tracking of a spiral ascent to 1.5 m height, a 1.5 m radius circuit at 1 m/s, and return to origin.

Fig. 6.5 shows a more realistic multi-axis maneuver in which the vehicle executes a spiral ascent up to 1.5 m altitude, completes one circuit of a 1.5 m radius circle at 1 m/s cruising speed, and finally descends to land at the origin. The think line indicates the desired position, and the data points reflect motion capture observations. Throughout the maneuver the vehicle maintains a northward heading, demonstrating independent control over both direction of travel and the yaw orientation.

6.6 Power for Hover

6.6.1 Symmetric Loading

Many useful tasks call for a MAV to loiter near a site of interest while supporting a sensor payload. The impact of added weight on power consumption was investigated by hovering

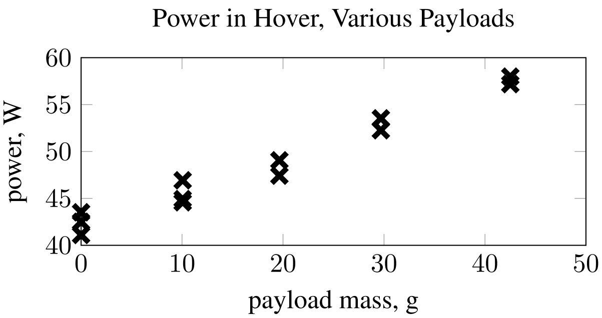

Figure 6.6: Electrical power consumption in hover with various payload masses.

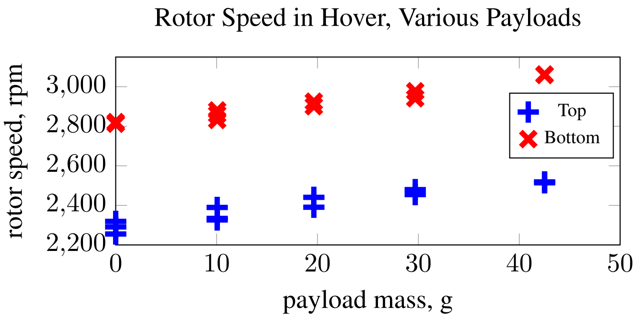

Figure 6.7: Rotor speed of the top (pulsing) and bottom (non-pulsing) propellers in hover with various payload masses.

with added masses of up to 18 % of the vehicle weight. Power consumption was measured onboard in flight, representing the combined requirements of the hosted electronics, thrust, and attitude control action. The rise in power consumption and rise in rotor speeds are shown in Fig. 6.6 and 6.7 for trials at five distinct loads. Importantly, the pulsing cyclic strategy works satisfactorily across the range of rotor speeds, requiring no parameter tuning.

These tests also establish that very little power in hover is wasted due to the pulsing attitude stabilization action. Roll and pitch control was disabled for brief periods of 0.5 s or more during which power consumption was monitored after waiting 0.25 s for initial transients to abate. This test accurately captures the inflow condition and torque balance between the propellers in flight. We also observe that pulsing control does not notably affect rotor speed in the hover condition. Over ten trials the mean power consumption was 40.6 W with a standard deviation of 1.0 W. As expected, little control effort is exerted in the hover condition and the hover power consumption of 42.4 W does not greatly exceed the thrust requirements alone.

For comparison, the addition of just the 24 g in dead mass representing the servos, linkages, and stabilizer bar of the comparable CX2 helicopter would increase the hover power requirement by more than 5.9 W to 114 % of the original. The removal of these components and their replacement with pulsing cyclic control represents an improvement in projected hover endurance, even neglecting the power requirements of the discarded actuators themselves.

For a fixed thrust, momentum theory indicates that increasing rotor area strongly correlates with decreased power requirements. This has been cited as a possibly advantage of large single rotor craft over conventional quadrotors, an advantage which motivates the hybrid vehicle in [19], [20]. Our method of cyclic control is another approach towards aerodynamically efficient rotorcraft which dispatch with the weight and complexity of servomotors, linkages, and swashplates.

6.6.2 Asymmetric Loading

In many cases a MAV can be co-designed with its payload to control the center of mass placement throughout the operation. For example, a fixed camera or a deployable chemical sensor might be considered in the initial design. However, an airframe retrofit or collection of an unknown payload can result in an asymmetric loading that must be balanced in flight by the vehicle's attitude control authority.

A series of hover tests demonstrate the ability of the pulsing blade control to overcome such persistent disturbances. Fig. 6.8 shows the increase in power requirements as a 10 g payload is repositioned from the center out towards the periphery of the vehicle. As expected, the rotor speeds remain relatively constant throughout these tests (Fig. 6.9) and the significant increase in power is due to the active pulsing control needed to maintain level flight. As with all MAVs, the location of the center of mass remains an important constraint for vehicles incorporating this style of attitude control.

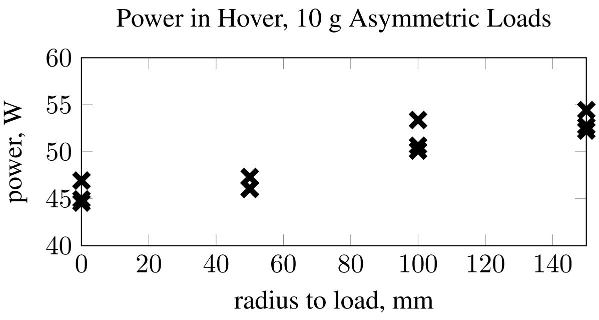

Figure 6.8: Electrical power consumption in hover with a 10 g payload offset laterally from the vehicle center.

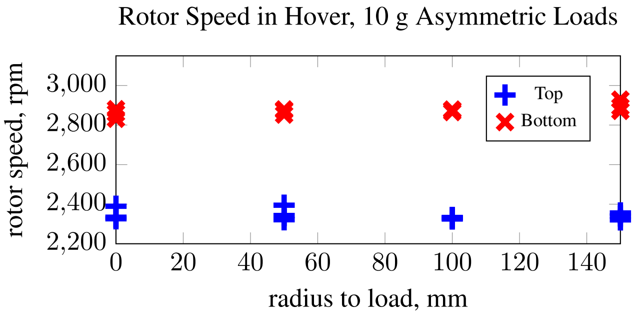

Figure 6.9: Rotor speed of the top (pulsing) and bottom (non-pulsing) propellers in hover with a 10 g payload offset laterally from the vehicle center.

6.7 Actuator Mass Budget

After the battery itself, actuator mass represents the second largest fraction of vehicle weight in five of the six quadrotors surveyed in [52], an ensemble of micro air vehicles from 43 g to 967 g. Conventional coaxial helicopters like the CX2 require only two drive motors instead of four, but must integrate a swashplate mechanism (Fig. 2.5), additional servomotors to drive it, and potentially a passive stabilizer bar to reduce the required control bandwidth (Fig. 2.4). Fig. 6.10 compares the mass budget of the 227 g pulsing coaxial helicopter to the 227 g conventional CX2 coaxial helicopter and an ensemble average quadrotor distribution from [52]. Elimination of the swashplate and actuators represents a significant reduction in the total actuator mass, therefore allowing larger onboard batteries and potentially longer flight endurance. A complete breakdown of the mass distribution within the pulsing coaxial helicopter is provided in Table 6.1.

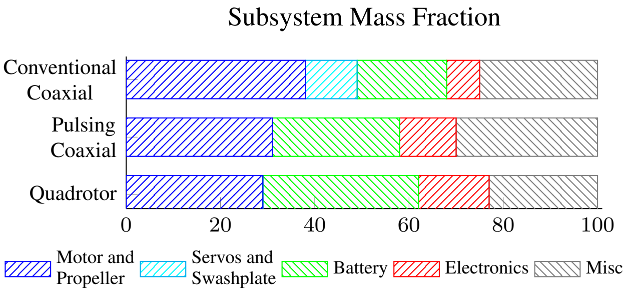

Figure 6.10: The swashplate and servomotors are a large fraction of the mass in a conventional coaxial helicopter (Blade CX2) but are eliminated in a pulsing coaxial helicopter and in quadrotors (ensemble averages from [52]).

Table 6.1: Mass budget of coaxial helicopter shown in Fig. 6.1.

component	mass
hinged propeller and fasteners	11.3 g
fixed propeller and fasteners	10.2 g
brushless motors	2 x 24.5 g
control circuit boards	2 x 14.0 g
11.1 V, 850 mAh battery	76.1 g
landing gear	18.3 g
8 mm reflective markers (4)	2.6 g
airframe and misc. hardware	31.6 g
total	227. g

6.8 Manufacturability and Cost

The rapid growth of quadrotor use in the MAV space owes in part to their mechanical simplicity and ease of manufacture. For quadrotors, the only moving parts are the commercial off-the-shelf motors themselves. Emerging manufacturing methods such as 3D printing, origami inspired folding, and laser cut fabrication have all been applied to rigid airframes [46], enabling prototyping and small batch production with low cost equipment.

In contrast, the conventional swashplate control system of the CX2 involves eight distinct ball and socket joints attending to the five linkages shown in Figs. 2.4 and 2.5 in addition to a ball bearing for the swashplate itself and free feather hinges for each blade. These types of precision components are a barrier to affordable direct additive prototyping. Further, while they are readily produced by injection molding in a factory environment, they introduce a laborious final assembly procedure. If fouled by grit from the environment, they will require field maintenance. The associated actuator cost is also not insignificant: the two \$15 servos in a CX2 actually cost more than the two \$10 brushed drive motors.

Direct cyclic control through pulsing torques introduces only two simple pin hinges and completely eliminates the need for ball and socket joints or ball bearings. The hinged hub itself is readily manufactured on common 3D printers, and could be molded directly as a feature of the propeller in a large scale operation. As a result, halving the number of motors, motor controllers, and propellers as found in a quadrotor can in fact reduce the overall component count and assembly time for these types of micro air vehicles.

6.9 Acoustics

The adoption of this control strategy may confer other indirect benefits which require further investigation. If MAV technologies are to be unobtrusively integrated into daily life, it will be important to consider the nuisance noise they generate [82]. Anecdotally, colleagues more familiar with quadrotors often comment on how quiet the coaxial vehicle is in flight. The central large rotors are much slower than the small rotors of a similarly sized quadrotor such as the KMel Nano+, which may help reduce noise levels. The median sound level in hover is 62 dBA for the pulsing coaxial helicopter and 70 dBA for the quadrotor as measured at 1 m by a consumer grade sound level meter. This is a perceptually significant difference in sound level. Simultaneously, we have eliminated the servomotors, stabilizer bar, and gearbox found in most helicopters, each a potential source of noise. Future work may consider how to leverage this design to promote quiet operation, improving user confidence in close quarters and opening new applications and operational environments to MAVs.

6.10 Other Coaxial Helicopter Demonstrations

6.10.1 Larger MAV with Loosely Integrated Avionics

The original test vehicle for dynamic cyclic control described in [60] was the coaxial helicopter shown in Fig. 6.11. The 358 g aircraft incorporated top and bottom propellers with a vertical separation of 28 cm, and used only the 39 cm top rotor for control. The system mass budget shown in Table 6.2 reveals the airframe and landing gear made up a large portion of the vehicle weight, and this inefficiency was improved upon in later iterations. The on board system included two motor controllers and a separate custom flight controller designed by the authors of [66] as well as a separate commercial internal measurement unit (IMU) device. This aircraft used the original non-flapping rotor described in [60] on the top and a commercial rigid rotor on the bottom to balance the drag torque and provide additional lift. It was flown manually, but automated testing and performance measurements were not undertaken.

6.10.2 Smaller MAV With Highly Integrated Avionics

A much smaller aircraft is shown in Fig. 6.12, with a total flying weight of 29 g (38 g with camera) and a rotor diameter of only 19.5 cm. This coaxial helicopter was demonstrated at [63] where it flew a simulated mission piloted remotely through its onboard camera system. In contrast with the other coaxial helicopters show here, this vehicle uses a conventional rotor configuration with two rotors above the body, one of which incorporated a passive stabilizer bar.

The motor, rotor, and chassis components were adapted from a $17 Syma S107G toy he-

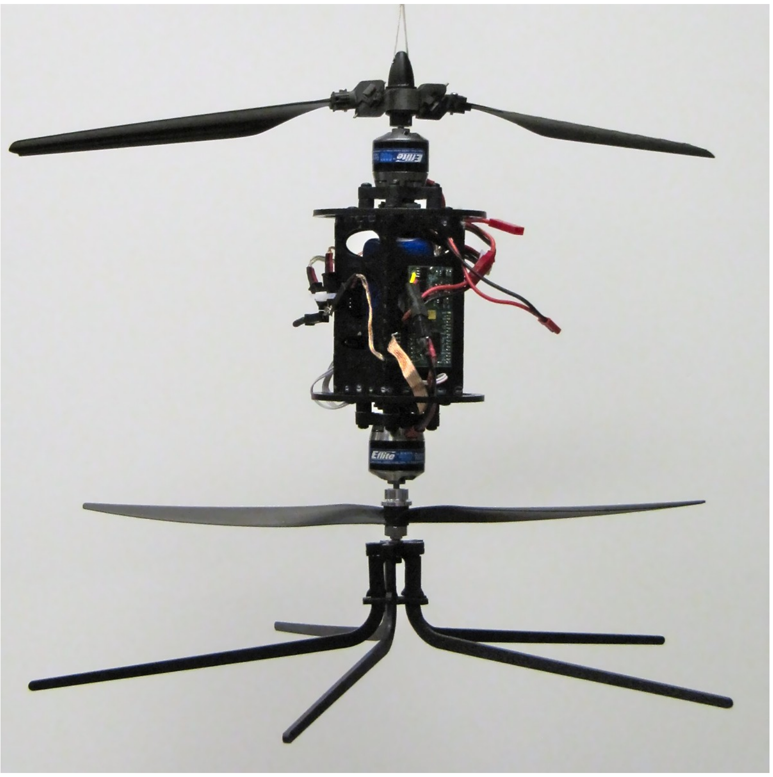

Figure 6.11: First coaxial helicopter to incorporate the dynamic cyclic rotor.

Table 6.2: Mass budget of original coaxial helicopter.

component	mass
hinged propeller and mandrel	21.0 g
fixed propeller and mandrel	16.6 g
brushless motors	2 x 54.8 g
motor controllers	2 x 10.5 g
inertial measurement unit (IMU)	2.5 g
radio and attitude controller	12.3 g
lithium polymer battery	70.4 g
landing gear	20.8 g
airframe and misc. hardware	84. g
total	358. g

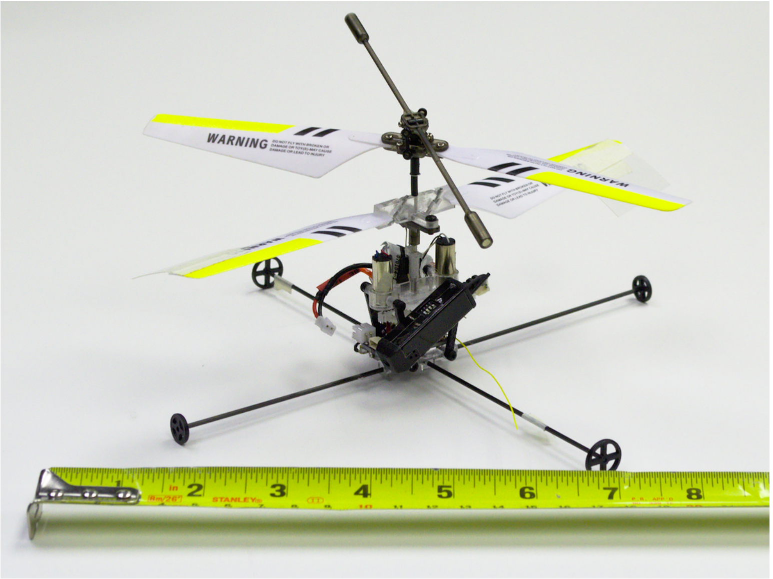

Figure 6.12: A 37 g coaxial MAV with onboard camera.

licopter as a donor vehicle. As a result the drive system uses mass produced brushed motors and a simple plastic gearbox. The original helicopter has no cyclic system, instead relying entirely on passive stability from a flybar system and employing a third pusher propeller for longitudinal control. The upgraded aircraft adds dynamic cyclic control to the bottom rotor for true roll and pitch authority. Rotor position sensing is based on timed interpolation between a once-per-revolution index from a binary hall effect proximity sensor. An onboard camera, full IMU with onboard attitude estimation, and digital telemetry capabilities were also added. In spite of these features and extended capabilities, the final aircraft weighs less than the original 40.3 g donor vehicle.

The final version of the aircraft uses a miniaturized version of the non-flapping hub employing simple pin hinges in a 3D printed body. However, early prototypes used monolithic flexible hub shown in Fig. 6.13. The hub was created by overmolding rigid polyurethane onto a flexible polyethylene sheet. The sheet acted as the flexible joint in defined regions where it was left exposed. Figure 6.14 illustrates the flexible sheet and the molding process. This construction principle is similar to methods for creating linkage and joint systems from laminates of rigid and flexible layers [88]. This hub was flown successfully and exhib-

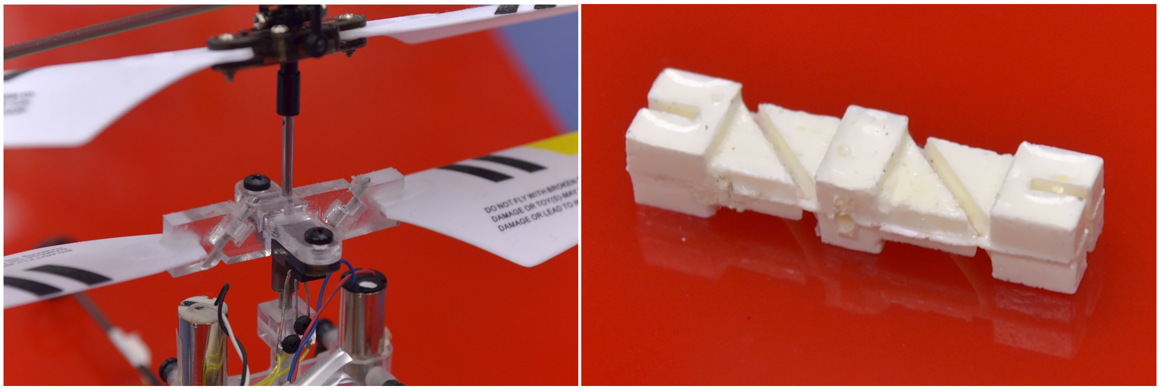

Figure 6.13: Pin hinge hub and alternative one-piece flexible hub.

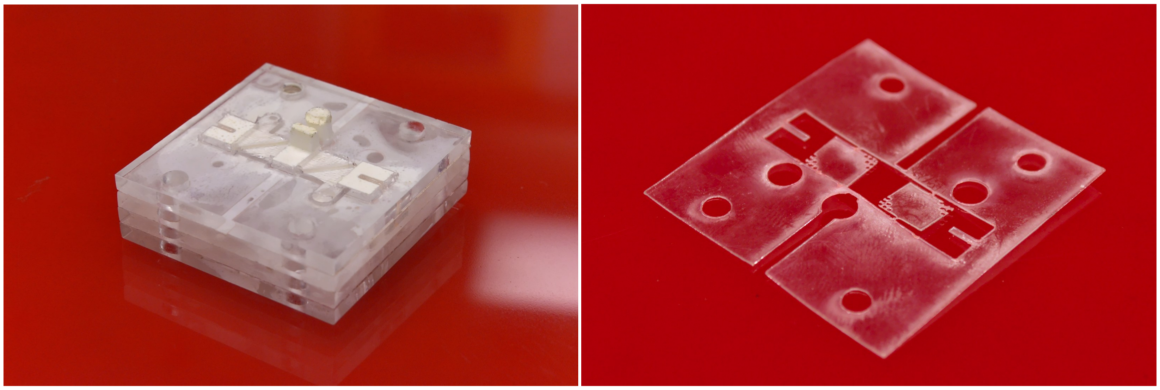

Figure 6.14: Polyurethane overmolding of flexible polyethylene sheet.

ited cyclic control, but the flexible element frequently tore out of the polyurethane during crashes, making it impractical. In addition a worn flexure would not act like an ideal hinge axis, but would instead allow some free torsion in pitch which tended to defeat the intended pitch-lag coupling and could even result in blade flutter. With good materials and process control a flexure might be an economical way to mass produce these hubs, but 3D printing small pin hinges has proven more reliable for single prototypes.

Chapter 7

Emulating a Fully Actuated MAV

Beyond replicating the function of conventional helicopter and quadrotor MAV, a compact cyclic control system enables new capabilities. The flapping rotor described in Chapter 4 is modified to instead employ a single teetering hinge, allowing now for control over the direction of the thrust vector with minimal direct moment at the hub. Two such actuators can emulate full actuation over net forces and moments in a coaxial helicopter, allowing maneuvers not possible with conventional underactuated MAV.

The control analysis, vehicle design, and flight experiments described in this chapter have been prepared previously for publication in collaboration with Bennet Caraher [62]. Bennet conducted a large amount of flight testing as a summer undergraduate lab assistant which led him to make important contributions to both the rotor construction methods and control software configuration. In collaboration with the author, some of the preliminary control allocation ideas were explored within a linear controls framework as part of Lindsey Marinello's bachelor's thesis [45].

7.1 Underactuated and Fully Actuated Aircraft

A variety of micro air vehicle (MAV) technologies are now available which provide the fundamental flight capabilities required for basic survey and transport tasks. These aircraft exhibit highly coupled rotational and lateral dynamics which must be taken into account in the control design and when specifying aggressive required trajectories. A popular example is the planar quadrotor, whose flight state exists in six dimensions over position and body orientation but which is equipped with only four actuators. These aircraft only have control over their attitude moment vector and the magnitude of net thrust downward in the body frame, and so they must maneuver spatially by constantly changing their orientation. As a direct consequence of this underactuation they are incapable of independently regulating both position and orientation. Furthermore, even smooth spatial trajectories can be infeasible unless they are c^3, which excludes such common techniques as both minimum jerk and trapezoidal velocity multi-segment trajectories.

Fully actuated aircraft with independent control over body forces and moments could support a multitude of new capabilities. Such aircraft would be able to apply arbitrary wrenches on the environment, making them useful for construction or object manipulation. In flight they could independently point cameras, sensors, or high gain antennas independent of motion trajectories or the wind environment. In indoor environments with humans they would able to gesture with the aircraft posture to make their motion intentions more legible to bystanders, visually indicate objects or directions as a guide, or provide visual cues to aid in human-robot task coordination. These possibilities have inspired diverse efforts to realize new types of fully actuated MAV.

Many previous embodiments of fully actuated, holonomic, or omnidirectional MAV are conceptually inspired by the quadrotor and proceed by adding additional actuators. By configuring six conventional rigid rotors with their orientations canted out of plane it is possible to obtain independent control over forces and moments in proximity to hover, but the inability to reverse independent rotor thrust directions limit feasible forces and therefore feasible stable orientations [12], [31]. With seven unidirectional rotors it becomes in principle possible to hover in all orientations, even upside down [56]. Incorporating eight variable-direction rotors allows practical flight in all orientations and would potentially permit control strategies which avoid driving motors at low speeds or with rapid direction changes [8]. Similar capabilities in six-rotor configurations become possible with high performance reversing motor drivers [83].

Coaxial helicopters offer a different point of departure for developing fully actuated aircraft. One can obtain authority over net forces and moments by augmenting two fixed pitch rotors with four more actuators to independently gimbal each motor in roll and pitch, vectoring their thrust [75]. Alternatively, a pair of conventional swashplates and teetering rotors can be driven by four roll and pitch servos to tilt the rotor tip path plane and achieve a similar effect [25]. These aircraft have an efficiency advantage over the aforementioned multirotors in that all of the rotor thrust can be directed downwards when in hover. However, they still require a minimum of six actuators for operation.

This chapter introduces a new coaxial helicopter which emulates fully actuated aircraft using only two actuators. We do this by taking advantage of the control over a flapping rotor's tip path plane exhibited in 4 using only modulation of the motor drive torque. Section 7.2 describes the idealized vehicle dynamics in terms of vectored thrusts derived from tilting top and bottom rotor tip path planes. Our method for controlling the tip path plane response is described in Section 7.3 along with measurements of the individual rotor capabilities for our particular realization. The vehicle hardware design is summarized in Section 7.4, and the control architecture described in Section 7.5. Flight results in Section 7.6 demonstrate decoupled lateral and rotational dynamics, confirming that this two-actuator MAV emulates the primary capabilities of a six-actuator, fully actuated MAV. This includes sustaining a stationary hover while pitching the aircraft up to 8°, and tracking trajectories with discontinuous accelerations up to $1\,\mathrm{m/s^2}$ without pitching or rolling.

7.2 Idealized Vehicle Dynamics

The vehicle dynamics can be approximated by considering a coaxial helicopter capable of tilting the direction of thrust from each rotor away from vertical. This thrust vectoring effect could conventionally be obtained from teetering rotors equipped with cyclic blade pitch control actuators. Our unique method for controlling the blade response using only the main drive torque will be examined in Section 7.3, but first we address a generic thrust

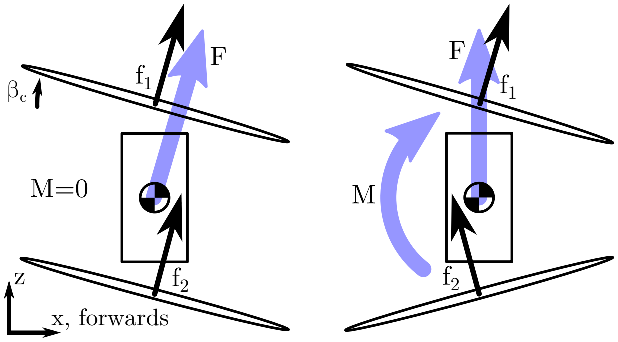

Figure 7.1: Teetering rotors allow independent control of force and moments.

vectoring idealization. Figure 7.1 depicts one rotor mounted a distance r_1 above the center of mass and a second counter rotating rotor mounted a distance r_2 below the center of mass. The figure conceptually illustrates that the force vectors f_1 and f_2 can be directed counter to each other in order to produce a net pitching moment about the vehicle's center of mass while maintaining zero net lateral force. Alternatively, the force vectors can be pointed in similar directions, yielding a net lateral force on the aircraft while maintaining zero net moment.

Equation 7.1 develops the net force F and moment M vectors about the aircraft center of mass as a linear function of the individual rotor force vectors f_1 and f_2. In addition to these rotor forces, we model a corresponding reaction torque about the z axis for each rotor which is proportional to its thrust along the z axis by a constant coefficient k_Q. This is a reasonable approximation for the small angular deflections in the forces considered here. Vectors F, M, f_1, and f_2 are written in component form in Eq. 7.1 with respect to body fixed x, y, and z axes.

$$\begin{bmatrix} F_x \\ F_y \\ F_z \\ M_x \\ M_y \\ M_z \end{bmatrix} = \begin{bmatrix} 1 & 0 & 0 & 1 & 0 & 0 \\ 0 & 1 & 0 & 0 & 1 & 0 \\ 0 & 0 & 1 & 0 & 0 & 1 \\ 0 & -r_1 & 0 & 0 & r_2 & 0 \\ r_1 & 0 & 0 & -r_2 & 0 & 0 \\ 0 & 0 & -k_Q & 0 & 0 & k_Q \end{bmatrix} \begin{bmatrix} f_{1x} \\ f_{1y} \\ f_{1z} \\ f_{2x} \\ f_{2y} \\ f_{2z} \end{bmatrix} \tag{7.1}$$

The constant coefficient matrix has a determinant of $2k_Q(r_1+r_2)^2$ and so will be full rank and invertible so long as the two rotors are not co-located. As a result the relationship can be inverted, and Eq. 7.2 provides a unique solution for allocating individual rotor controls f_1 and f_2 given a desired net vehicle force and moment. If the six components of rotor forces f_1 and f_2 are available as independent inputs, the aircraft will be fully actuated in all six operational degrees over orientation and position.

$$\begin{bmatrix} f_{1x} \\ f_{1y} \\ f_{1z} \\ f_{2x} \\ f_{2y} \\ f_{2z} \end{bmatrix} = \begin{bmatrix} \frac{r_2}{r_1+r_2} & 0 & 0 & 0 & \frac{1}{r_1+r_2} & 0 \\ 0 & \frac{r_2}{r_1+r_2} & 0 & \frac{-1}{r_1+r_2} & 0 & 0 \\ 0 & 0 & \frac{1}{2} & 0 & 0 & -\frac{1}{2k_Q} \\ \frac{r_1}{r_1+r_2} & 0 & 0 & 0 & \frac{-1}{r_1+r_2} & 0 \\ 0 & \frac{r_1}{r_1+r_2} & 0 & \frac{1}{r_1+r_2} & 0 & 0 \\ 0 & 0 & \frac{1}{2} & 0 & 0 & \frac{1}{2k_Q} \end{bmatrix} \begin{bmatrix} F_x \\ F_y \\ F_z \\ M_x \\ M_y \\ M_z \end{bmatrix} \tag{7.2}$$

7.3 Implementation Of Thrust Vectoring

Thrust vectoring for control through tilting of the tip path plane can be implemented without adding any additional actuators beyond the top and bottom drive motors themselves. In previous work it has been shown that a single motor can control both the mean operating speed and cyclic blade pitch variation of a rotor by modulating the applied drive torque [61]. Two blades are attached to a hub with skewed lag-pitch hinges, as shown in Fig. 7.2. Modulating the motor torque sinusoidally at one-per-rev excites a synchronous lead-lag motion in each blade within the plane of rotation. The skewed lag-pitch hinge couples this lag oscillation into a blade pitch oscillation. The two blades are mounted on asymmetric hinges so that one has a positive lag-pitch coupling and the other a negative lag-pitch coupling. As a result a one-per-rev sinusoidal modulation in motor torque causes the blades to pitch 180° out of phase with each other, phase locked with the rotor rotation. By controlling the amplitude and phase of the motor torque the amplitude and azimuthal phase of the blade pitch can be controlled. The aircraft in [61] is capable of attitude control like a standard

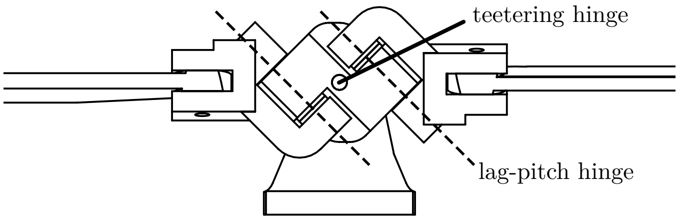

Figure 7.2: Teetering rotor with skewed lag-pitch hinges.

quadrotor or helicopter and maneuvers by taking advantage net direct hub moments arising when, for example, both blades cyclically pass across the aircraft nose at minimum pitch and lift but pass across the tail at maximum pitch and lift.

Independent offset flap hinges were added in [64] to allow each blade to individually flap up and down during each revolution in response to changing blade pitches and the resulting blade lift. In addition to direct moments on the hub, this causes an apparent tilting of the tip path plane and redirection of the thrust vector.

The operational principle depicted in Fig. 7.1 benefits from large flapping angles and a pure thrust vectoring effect with no direct moments applied to the hub which earlier versions of the rotor do not achieve [61]. This is now obtained by incorporating a single, central teetering hinge as seen in Figs. 7.2 and 7.3. For each degree of cyclic blade pitch authority a teetering rotor enjoys one degree of flap and tip path plane inclination, and the thrust force may be thought of as remaining perpendicular to this tip path plane. At the same time, no direct torques can be transfered to the hub through the teetering hinge.

The change in blade flap angle β as a function of azimuthal angle ψ is conventionally described as

$$\beta(\psi) = \beta_c \cos(\psi) + \beta_s \sin(\psi) \tag{7.3}$$

where $\psi = 0$ in the aft direction and ψ increases in the direction of rotation. It follows that, for the counterclockwise top rotor, β_c describes a longitudinal tilting of the tip path plane forwards and β_s describes a lateral tilt towards the side of the retreating blade. The thrust can be expressed as a function of rotor speed Ω_1 and thrust coefficient k_T as $k_T\Omega_1^2$. Employing a small angle approximation in β the rotor force vectors f_1 and similarly constructed f_2

are expressed in Eq. 7.4, where the difference in sign is due to their opposing directions of rotation.

$$
\begin{aligned}
f_{1x} &= k_T \Omega_1^2 \beta_c & f_{2x} &= k_T \Omega_2^2 \beta_c \\
f_{1y} &= k_T \Omega_1^2 \beta_s & f_{2y} &= -k_T \Omega_2^2 \beta_s \\
f_{1z} &= k_T \Omega_1^2 & f_{2z} &= k_T \Omega_2^2
\end{aligned} \tag{7.4}
$$

The motor torques driving the gross propeller rotation as well as the cyclic blade pitch and flapping response are a result of modulating the applied motor voltage. The applied voltage V is the sum of two parts: a proportional-integral control on error between the observed rotor speed $\dot{\psi}$ and desired speed Ω with gains k_P and k_I, and an additional voltage modulation $\tilde{V}$.

$$V = -k_P(\dot{\psi} - \Omega) - k_I \int (\dot{\psi} - \Omega) dt + \tilde{V} \tag{7.5}$$

Previous modeling and experimental validation suggests a useful approximation for the flap response in terms of the applied voltage modulation [64]. The flap response in β lags the voltage modulation $\tilde{V}$ by an angle ϕ_β. The flap amplitude is proportional to the voltage amplitude $\tilde{V}$ in excess of a minimum threshold $\tilde{V}_{min}$ by a linear constant k_β. Parameters ϕ_β, $\tilde{V}_{min}$, and k_β are functions of the rotor physical properties, electromechanical motor properties, and software speed control gains. They are valid near a trim thrust condition, and are readily determined with a bench test. The final expression for $\tilde{V}$ is then given by Eq. 7.6, where it is convenient to write the desired flapping in terms of polar amplitude a and phase ϕ.

$$
\begin{aligned}
a &= \sqrt{\beta_c^2 + \beta_s^2} \\
\phi &= \operatorname{atan2}(\beta_s, \beta_c) \\
\tilde{V} &= (\tilde{V}_{min} + k_\beta a) \cos(\psi - \phi - \phi_\beta)
\end{aligned} \tag{7.6}
$$

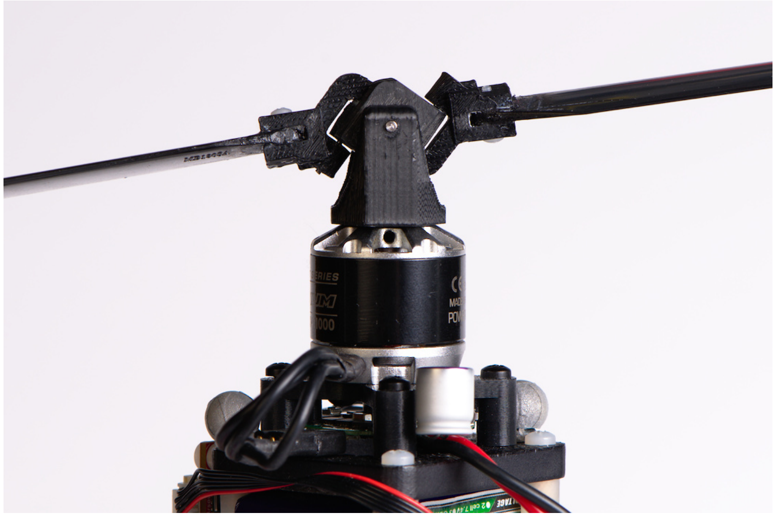

Figure 7.3: Top rotor of coaxial helicopter.

7.4 Hardware Design

The flight vehicle is shown in Fig. 7.4, incorporating two counter-rotating propeller systems which are depicted in Fig. 7.3. The rotors are 32 cm in diameter, and are driven to a trim hover speed of approximately 370 rad/s by two size 2212 BLDC motors. The rotor blades are commercial symmetric airfoils attached to custom 3D printed hub pieces which are joined by steel pin hinges with PTFE plastic washers added to reduce friction. The full aircraft mass is 380 g, with the center of mass approximately equidistant between the two rotors which are themselves 16 cm apart.

A commercial flight controller using the PX4 autopilot software [47] runs an attitude tracking control law to generate desired body moments M. The desired body attitude as well as additional body force commands F are passed in through a WiFi radio link. The flight controller calculates speed Ω and flap parameters β_c, β_s for each rotor based on linear combinations of F and M consistent with Eqs. 7.2 and 7.4 near trim. These parameters are passed to the motor controller as three PWM encoded values.

The custom motor controller is responsible for applying drive voltage V based on desired parameters Ω, β_c, and β_s according to Eq. 7.5 and 7.6. This is made possible by direct measure of the hub orientation ψ using a 4096 count hall effect rotary encoder.

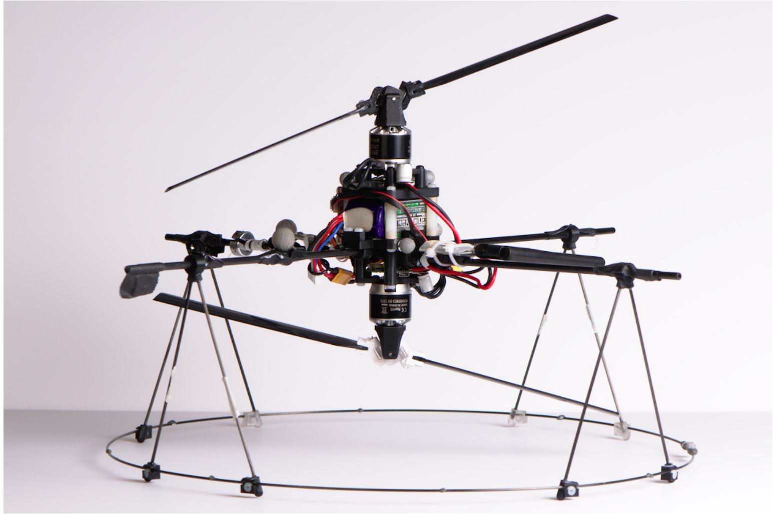

Figure 7.4: Coaxial helicopter.

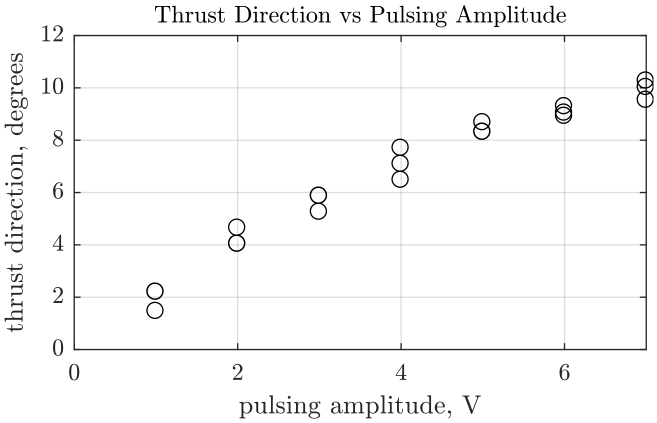

Figure 7.5: Bench measurements of lateral forces and increasing voltage modulation amplitude.

During bench testing the rotor was operated at 370 rad/s, obtaining a thrust of 2.9 N. Figure 7.5 shows the obtained angular deflection of the thrust vector due to blade flapping as determined by measuring the lateral forces generated. These angles agree closely with a visual observation of the tip path plane. A maximum deflection of 10° in the force vector was obtained, corresponding to a lateral force of 0.5 N. At lower operating speeds, large flap angles become practical.

The tip path plane response is rapid but unlike the idealization used to motivate the control design it is not instantaneous. The two images in Fig. 7.6 were captured sequentially, separated by 200 ms. During this time the rotor tip path plane was moved from

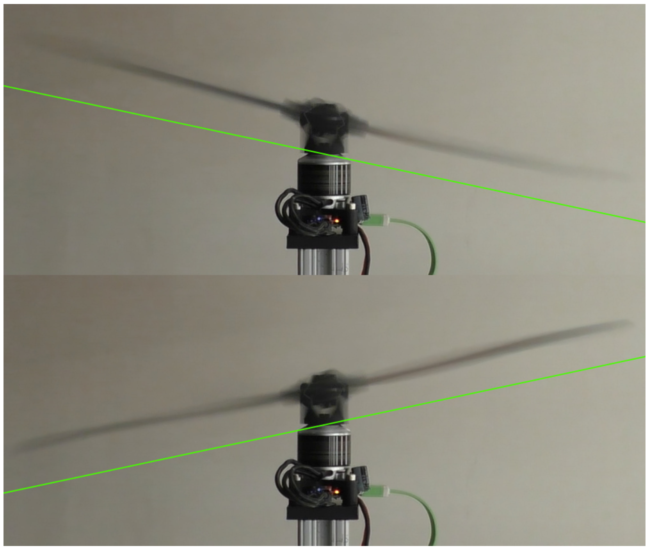

Figure 7.6: Tip path plane transition over 200 ms shown with ±12° reference.

approximately 12° to −12° while operating at a nominal head speed of 300 rad/s.

7.5 Control Design

Trajectory tracking control for a conventional underactuated quadrotor might proceed as illustrated in Fig. 7.7 using cascaded position and attitude controllers. A reference spatial trajectory x_t is compared with the observed vehicle position x and desired corrective accelerations $\ddot{x}_{des}$ are computed. An attitude planner identifies a desired vehicle orientation R_{des} and thrust T_{des} associated with that acceleration, and a closed loop attitude controller generates desired body moments M_{des} to track the commanded orientation. The desired thrust T_{des} and moment M_{des} are passed through an approximate inverse actuator model to produce low level actuator commands u (e.g. rotor speeds). Those commands produce aerodynamic forces and moments F and M for the physical aircraft, which responds subject to its dynamics.

In contrast, the updated control architecture in Fig. 7.8 takes advantage of the fully actuated capabilities of the new aircraft. The desired orientation R_{des} can be freely specified as part of the trajectory alongside x_t. Desired translational accelerations $\ddot{x}_{des}$ can be expressed in the body frame directly as desired forces F_{des}. Desired forces and moments

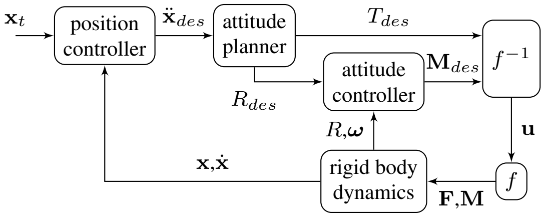
$\mathbf{x}_t$
position controller
$\ddot{\mathbf{x}}_{des}$
attitude planner
T_{des}
R_{des}
attitude controller
$\mathbf{M}_{des}$
f^{-1}
R,$\boldsymbol{\omega}$
$\mathbf{u}$
$\mathbf{x}$,$\dot{\mathbf{x}}$
rigid body dynamics
$\mathbf{F}$,$\mathbf{M}$
f

Figure 7.7: Conventional trajectory control for underactuated quadrotor.

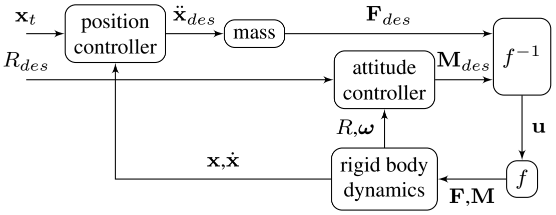
$\mathbf{x}_t$
R_{des}
position controller
$\ddot{\mathbf{x}}_{des}$
mass
$\mathbf{F}_{des}$
attitude controller
$\mathbf{M}_{des}$
f^{-1}
R,$\boldsymbol{\omega}$
$\mathbf{u}$
$\mathbf{x}$,$\dot{\mathbf{x}}$
rigid body dynamics
$\mathbf{F}$,$\mathbf{M}$
f

Figure 7.8: Fully actuated trajectory and orientation control.

F_{des}, M_{des} are transformed by an approximate inverse actuator model into low level actuator commands Ω, β_c, and β_s representing the speed and tip path plane tilt for each rotor.

7.6 Flight Experiments

Three different flight experiments were conducted to demonstrate full actuation of aircraft moments and forces, separation of rotational and translational dynamics, and the impact of actuator limitations on the available flight envelope. In each flight the aircraft tracks a time parameterized trajectory in simultaneous orientation and position. The attitude tracking controller and actuator control allocation are performed on the aircraft using onboard sensor information. The position controller is implemented on a group based laptop which makes use of absolute position and heading information available from a motion capture system. The resulting force commands sent to the vehicle reflect both proportional-derivative action and the reference acceleration of the target trajectory.

7.6.1 Orientation Control in Hover

In the first experiment the aircraft ascends to a stable hover at position $(x, y) = (0, 0)$. The aircraft then pitches nose down to -8° and then up to 8° while maintaining a stationary position error of less than 13 cm as shown in Fig. 7.9. Since the aircraft is stationary, the

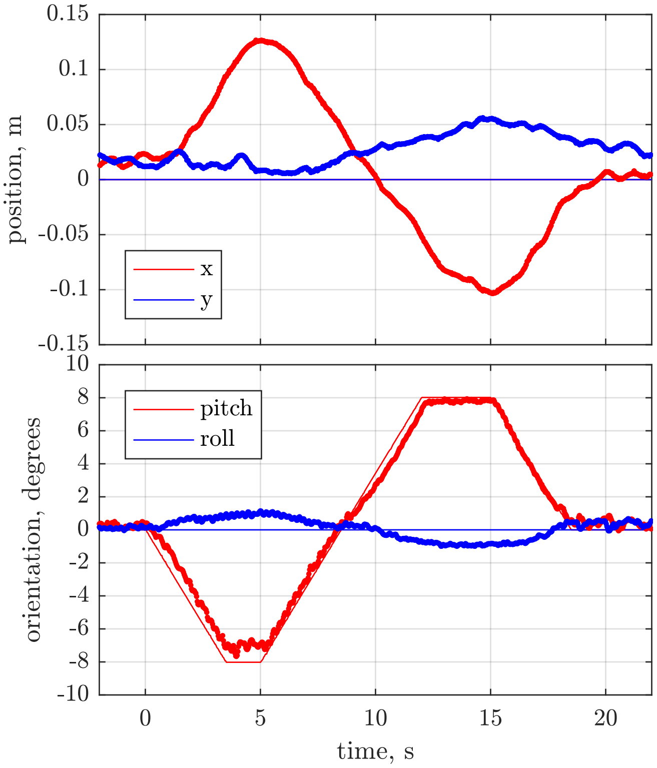

Figure 7.9: Stationary hover while pitching from −8° to 8°.

net force must be the aircraft weight 3.7 N directed 8° off the body fixed z axis, representing a lateral force in the body frame of 0.5 N.

This test demonstrates the maximum pitch angle at which the vehicle can remain stationary. At larger pitch angles there is insufficient flapping authority to avoid accelerating in the direction of the aircraft pitch. The position data shows a small offset in the x direction which correlates to the current pitching angle. This is a result of a systematic underestimation of the cyclic commands required to balance the lateral force at any particular pitch angle, which then must be brought into balance for hover by the proportional term of the position error controller. The magnitude of this position error is therefore a function of both the accuracy of the actuator models and the stiffness of the position control gains.

Since this experiment establishes that the vehicle can produce 0.5 N lateral force in hover, one might expect a theoretical maximum lateral acceleration of $1.3\,\mathrm{m/s^2}$ even while maintaining perfect level pitch, which is analogous to the acceleration of a quadrotor pitched over at 8°.

7.6.2 Acceleration without Pitch or Roll

The experiment described in Fig. 7.10 demonstrates tracking a trajectory which would be very challenging for an underactuated quadrotor to execute accurately. Furthermore, the aircraft maintains a level attitude throughout the maneuver which would be impossible for a quadrotor. From rest in hover, the commanded lateral acceleration steps instantaneously to $1\,\mathrm{m/s^2}$. The velocity increases uniformly until the aircraft reaches $1\,\mathrm{m/s}$, at which time the acceleration instantaneously becomes zero again. After cruising some distance at constant speed the vehicle speed is then arrested with a period of constant deceleration at $1\,\mathrm{m/s^2}$. Figure 7.10 shows that the vehicle faithfully tracks the trapezoidal velocity profile. Because the tip path plane dynamics are so much faster than the body attitude dynamics of a quadrotor, it can even do a fair job tracking the instantaneous step in acceleration which, for a quadrotor, would require instantaneous reorientation of the entire vehicle. Meanwhile the vehicle remains within approximately 1° of a flat hover posture throughout the maneuver, while a quadrotor would be forced to pitch to more than 5° to achieve similar acceleration.

7.6.3 Smooth Trajectory Following

Many apparently smooth trajectories which might be desired by camera operators or generated by spline methods are likewise difficult for an underactuated MAV to execute cleanly. Figures 7.11 and 7.12 show the MAV flying at $0.5\,\mathrm{m/s}$ and then entering tangentially into a circular path of radius 35 cm. Upon entry into the circle, the required acceleration jumps from $0\,\mathrm{m/s^2}$ to $0.7\,\mathrm{m/s^2}$. Then as the circle is tracked while maintaining heading in the x direction the acceleration vector continuously changes direction in both the world and body frames. Once again this maneuver can be completed with approximately 1° of unwanted pitching and rolling of the aircraft.

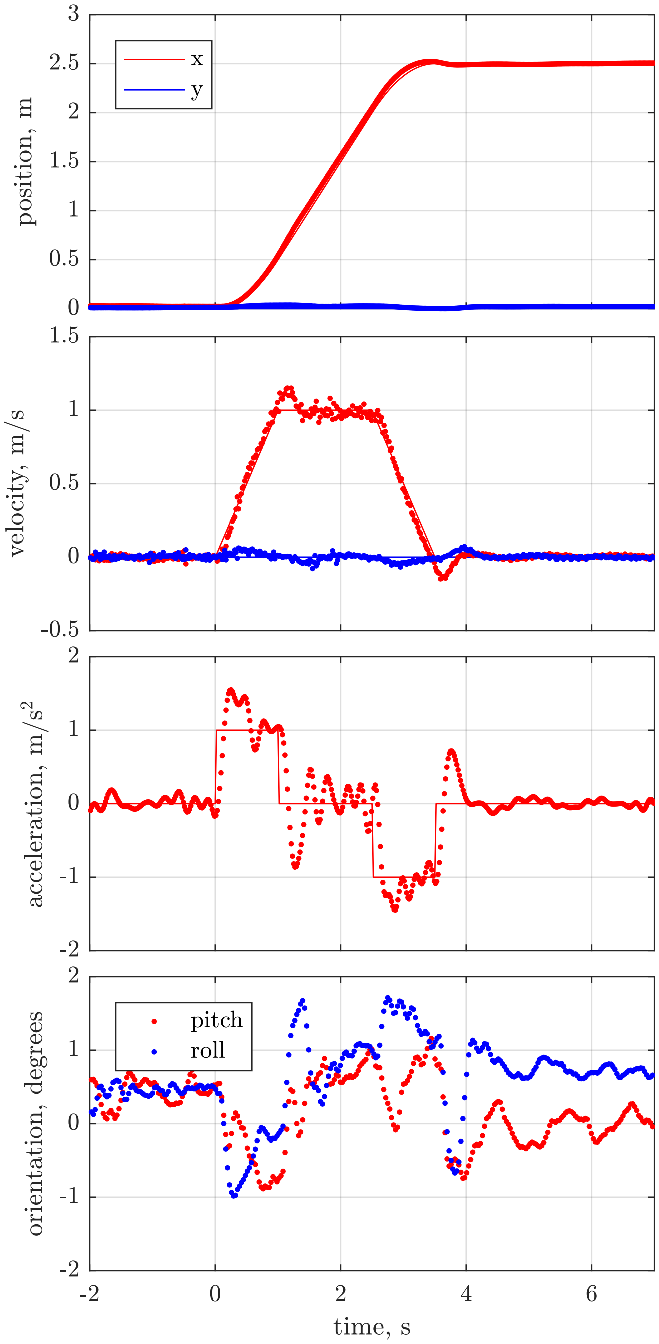

Figure 7.10: Acceleration at $1\,\mathrm{m/s^2}$ while maintaining flat attitude.

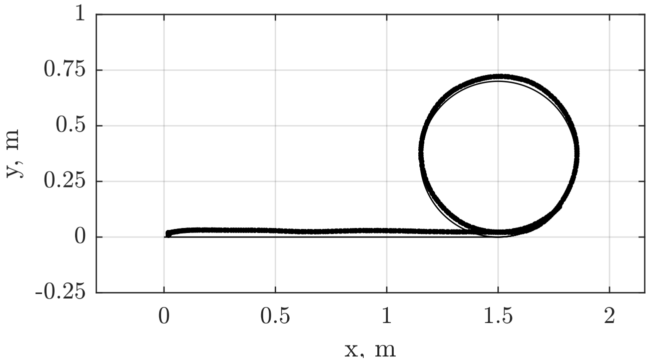

Figure 7.11: Flight at 0.5 m/s into a circle of radius 35 cm.

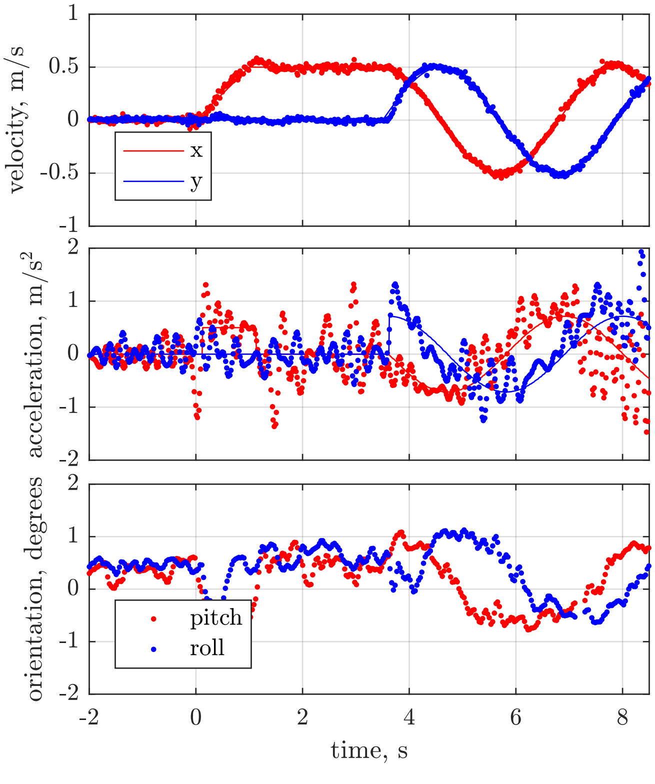

Figure 7.12: Rapid changes in desired acceleration tracked while maintaining vertical orientation.

7.7 Applications and Future Work

The preceding flight experiments demonstrate that this coaxial helicopter, equipped with only two actuators, can emulate the capabilities of a fully actuated MAV. Unlike a conventional underactuated quadrotor this MAV enjoys independent control over the body moment and force vectors, making it possible to hover in non-upright orientations or accelerate laterally without pitching or rolling the aircraft. Similar capabilities in the past have only been achieved using a total of six or more actuators. Experiments demonstrate the ability to maintain a stationary hover while pitched at up to 8°, as well as the ability to accelerate laterally at $1\,\mathrm{m/s^2}$ without pitching or rolling. Since the aerodynamic force is directed by fast rotor flapping dynamics instead of relying on changing the attitude of the entire aircraft, even smooth trajectories with discontinuous required accelerations can be tracked with a high degree of fidelity.

Existing platforms overcome the limitations of underactuated flight dynamics by adding articulated subsystems. Conventional quadrotors can not fully control their body wrench, but they can be equipped with a dexterous manipulator to apply wrenches to grasped objects. The view from a rigidly mounted camera suffers uncontrollable rolling and pitching during flight maneuvers, but cameras can be mounted on multi-axis gimbals. Embedding these capabilities directly into the flight platform may allow for lighter, cheaper or more robust MAV.

Future work will focus on increasing the angle of thrust vectoring available from each rotor. This will expand the permissible orientations for hover and increase the feasible lateral forces and accelerations for tracking trajectories or rejecting wind disturbances. The aerodynamic interaction between the rotors has been ignored in the present work. Modeling these effects may inform the design of the top and bottom rotors for both improved aerodynamic efficiency, or suggest command allocations for more accurately generating desired forces and moments. Finally, we have considered only the situation where both aircraft orientation and path are simultaneously prescribed. Returning to the classic problem of tracking aggressive spatial trajectories, we may consider how to optimally exploit both the free attitude dynamics and force vectoring capabilities subject to actuator constraints.

Chapter 8

Future Aircraft Formats

Contemporary micro air vehicle design has been strongly informed by available actuator technologies, and so it is to be expected that a new compact method for cyclic control could enable new and exotic formats for future MAV. An eventual progeny of the 1996 DARPA MAV program, the dominating aspect of the RQ-16 T-Hawk is the combustion driven ducted fan around which the vehicle is built [28]. Later outputs of the 2005 DARPA NAV program were similarly dictated by their propulsion and control technologies. The disparate designs of a coaxial helicopter, flapping wing MAV, and spinning maple seed aircraft each attempted to leverage different emerging technologies [30]. The relaxation of the passenger-centric constraints of manned aviation along with the co-location of roll, pitch, and thrust control in a single actuator permit a variety of unusual vehicle morphologies.

8.1 Single Motor Aircraft

Fig. 8.1 shows UNO, a vehicle with only a single rotor and motor, with a freely counter-rotating body. UNO is one of a family of vehicles devised by Matthew Piccoli which demonstrate stable passive attitude dynamics [67], and the mechanical design and aerodynamic optimization of UNO is detailed in [68]. As the single propeller is driven clockwise the aircraft body (itself consisting of lifting fins) is driven counterclockwise. Even without an onboard controller, UNO tends to orient upright and come to rest with respect to the rel-

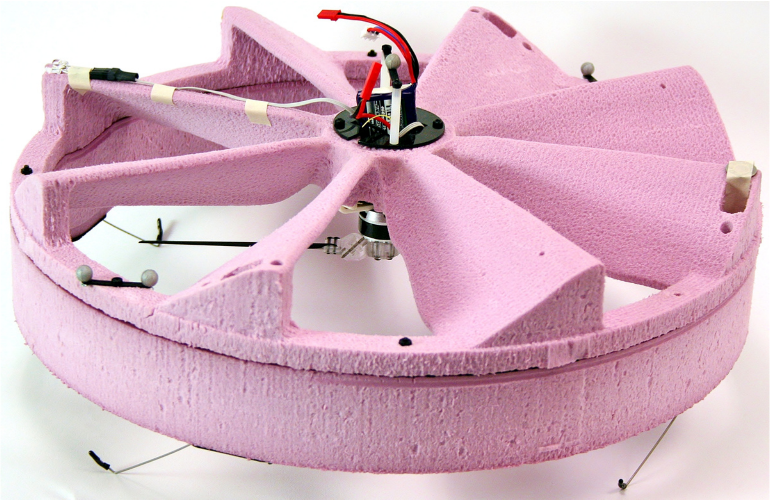

Figure 8.1: UNO, a single motor MAV. Photo credit: Matthew Piccoli [68].

ative wind. This remarkable property is achieved by taking advantage by the difference in lift generated by the fan blades on the advancing and retreating side of the body as the vehicle translates laterally. The resulting body torque, coupled with favorable gyroscopic dynamics, tilts the vehicle opposing the direction of motion and brings it back to rest with respect to the relative wind.

UNO as configured in Fig. 8.1 weighed 184 g with an outer body diameter of 392 g. The body with integrated fan blades was machined from a block of extruded polystyrene with plastic threaded inserts added to allow the attachment of the motor drive model as used in Chapter 7 and a separate custom flight controller designed by Piccoli.

In collaboration with the author, UNO has been augmented with a dynamic cyclic rotor to allow maneuvering control through 3D space despite having only a single onboard motor. UNO has no natural nonrotational reference frame since the entire vehicle operates as a coaxial rotor system consisting of a large slow fan (body) and fast inner rotor. A virtual north-pointing pilot frame was generated using an onboard estimate of the body azimuthal angle determined from a MEMS rate gyroscope. During manual flight operations this pilot frame was allowed to drift slowly with integrated angular error, to be compensated for by the pilot. However, in conjunction with an offboard motion capture system an absolute pilot frame heading was also achieved. A forward pointing indicator for the pilot frame was generated by an LED on the spinning body, taking advantage of the persistence of vision effect. The pilot frame then provided a reference to apply cyclic torque modulation for an underactuated rotor of the type discussed in Chapter 4. By applying a continuous cyclic effort the vehicle's trim condition could be displaced from a steady hover to a steady forward cruise.

Use of cyclic blade control stands in contrast to the eventual control strategy employed by Piccoli in [70] for a tiny 5 g spinning body embodiment of this aircraft. For cyclic control, a central large rotor is driven with a torque modulation at the rotor frequency to excite a coherent cyclic response. Instead, a smaller rigid rotor mounted offset from center may have its speed modulated at the body frequency, increasing and decreasing its thrust as the body rotates. The later strategy was considered more practical for the tiny aircraft, as the body rotational speed was much slower than the extreme operating speeds of a 28 mm propeller. On the other hand a centered rotor allows for larger propeller for a given overall aircraft diameter, which is generally expected to improve power efficiency in hover.

8.2 VTOL Flying Wing Aircraft

Fixed wing aircraft can have significantly larger operating ranges than hovering rotorcraft, but many application for MAV require the use of unprepared landing zones or loitering near objects of interest. As a compromise, many variations on vertical takeoff and landing (VTOL) fixed wing aircraft have been proposed. These aircraft are often heavier, more complex, and more costly than either a conventional multirotor or airplane because they combine or duplicate subsystems found in both. Some aircraft use lifting rotors for vertical flight which are then stowed as dead weight during fixed wing transit. Tilt wing aircraft add additional motors to actuate the wing posture to orient rotors upwards for hover and forwards for flight [23]. Individual rotors can also be mounted on gimbals and rotate separately from the wing [55], allowing two rotors and two servomotors to control both hover and fixed wing flight. There are four-propeller flying wing aircraft where the rotors have been spaced on pylons sufficiently far above and below the wing that they can operate as quadrotors in

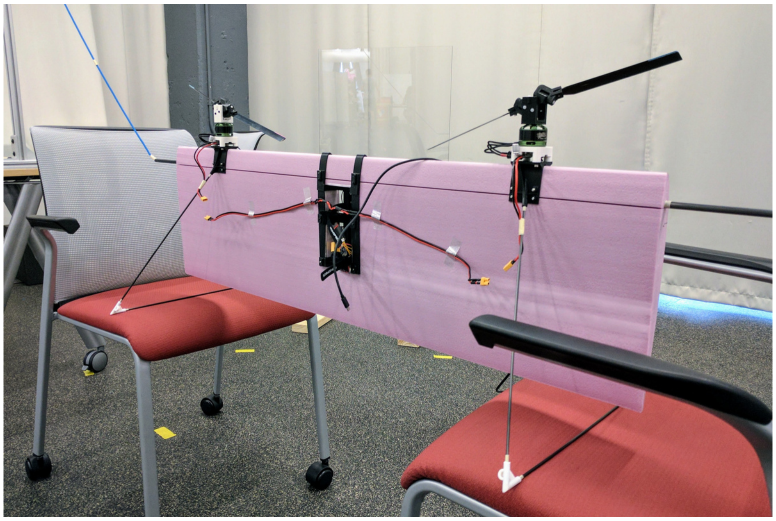

Figure 8.2: VTOL flying wing aircraft with only two motors.

hover [22]. Finally, cyclic control of large rotors may be used for attitude stabilization in hover [17].

The flying wing aircraft shown in Fig. 8.2 was developed by Ashish Macwan in collaboration with the author as part of his master's thesis in order to understand how dynamic cyclic control could simplify the design of fixed wing VTOL aircraft [44]. Ashish was responsible for the detailed aircraft design as well as all construction and flight testing. The author developed the principle concept with the benefit of fruitful discussions with David North and others of the Mars Electric Reusable Flyer group at NASA Langley [55], and benefited from the experience of Matthew Piccoli [69] while refining the onboard electronics.

Using the dynamic cyclic approach, two rotors in tandem are sufficient to stabilize a flying wing aircraft in hover with no added gimbals or control surfaces. The net thrust and rolling moments in the hover posture can be controlled by increasing and decreasing the rotor speeds, much as in a multirotor aircraft. Pitching moments and generated by applying forward or aft cyclic to both rotors. Finally, yaw control requires applying forward cyclic to one rotor and aft cyclic to the other and taking advantage of the thrust vectoring properties of the flapping rotors, as shown in Fig. 8.3. In fact, without this thrust vectoring effect it would not be possible to simultaneously govern yaw and roll as variations in thrust and drag torque are coupled.

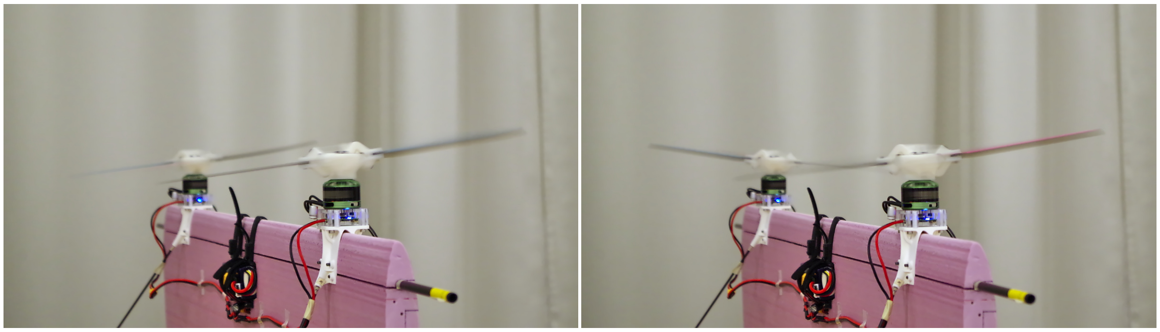

Figure 8.3: Rotor tilt for roll and yaw maneuvers. Photo credit: Ashish Macwan.

Table 8.1: VTOL fixed wing aircraft properties.

mass	870 g
wingspan	1 m
rotor diameter	33.5 cm
measured airspeed	8.1 m/s

Gross specifications for this prototype are given in Table 8.1. During manually piloted experiments with onboard attitude stabilization the aircraft has performed controlled near-hover maneuvers indoors. The aircraft has also performed the transition from hover to forward flight outdoors, but control authority during fixed wing cruise is very limited and recovery to hover has not been successfully demonstrated. In the future, control authority may be improved by increasing the allowed tip path plane pitching or by augmenting the aircraft with conventional control surfaces, a method which has previously been combined with active gimbaled rotors [55].

Chapter 9

Conclusion

This work develops the first dynamical model and first experimental demonstration of a rotor system which exploits lag-pitch coupling in order to allow motor torques to control cyclic blade pitch. Using this principle a single motor and rotor can control thrust, roll, and pitch in a MAV. The technology has been successfully applied to a broad family of MAV aircraft including coaxial helicopters, spinning body aircraft, and twin rotor VTOL airplanes. Applying this technique in commercial MAV can improve existing mission endurance or confer new capabilities without increasing the aircraft's complexity to the operator.

Rotor modeling and experimental validation establish a foundation for quantitative predictions of rotor performance and a qualitative analysis of the technology's suitability to very small and very large scale systems. The dynamical model extends the combined lag-flap modeling for rotors with lag-pitch coupling in the literature to include the impact of a non-constant hub speed. This has a dramatic effect on the lag dynamics for aircraft with low inertia hubs, including many modern electronic drive MAV. By explicitly considering unsteady torques as an input, the model resolves the dynamical mechanism by which cyclic torques can excite useful cyclic blade pitch changes.

Experiments validate the rotor model across an order of magnitude in scale and speed, from 10 cm to 100 cm in diameter and from 90 rad/s to 900 rad/s in rotor speed. To this end, we have developed new low-cost and non-invasive methods for measuring blade motions in the tiny, high speed rotors central to future MAV and NAV research. These techniques reveal that our model accurately predicts the blade motion in terms of motor reaction torque, hub speed, lag angle, and blade pitch.

Scaling arguments show the fundamental dynamic rotor response is relatively insensitive to size and in principle applicable to both very small MAV and large manned aircraft. However, large scale combustion engine technologies do not have the bandwidth required for torque modulation at the rotor frequency, and so for the time being these techniques are most readily applied to electric drive aircraft. With respect to operation of a fixed aircraft, we find that as mission weight increases the modulation torque required to achieve a particular cyclic blade pitch increases in proportion to the rotor's drag torque. With respect to aircraft design, we find that increasing the rotor size for a given mission weight reduces torque modulation requirements relative to the drag torque. As a result, aircraft using this technology are free to adopt large, aerodynamically efficient rotors.

Flight experiments with an array of aircraft from 29 g to 870 g demonstrate the practical application of this new actuator to existing MAV configurations as well as the creation of new, unique capabilities enabled by this technology as shown in Table 9.1.

The dynamic cyclic technique can improve the flight endurance and reduce the complexity of parts requiring maintenance in conventional helicopters while replicating conventional flight capabilities. Flight experiments with a coaxial helicopter demonstrate that a two-actuator vehicle can track paths through 3D space and maintain yaw heading in much the same manner as four-actuator quadrotors or four-actuator conventional helicopters, and it may do so using the same cascaded trajectory tracking framework. Weighed against conventional servomotor and swashplate technology, we show that the reduction in hover power requirement due to reduced actuator weight dominates the increased electrical power associated with torque modulation in near hover. As a result, these aircraft benefit from the conventional aerodynamic power efficiency advantages of large rotor helicopters over multi-rotors. At the same time, all of the mechanical complexity of the swashplate servo system, linkages, and ball joints is replaced in this vehicle by simple hinges in an articulated rotor.

	Traditional trajectory tracking with two actuators instead of the usual four or more.
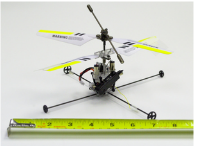	Teleoperated flight with cyclic control using toy-grade hardware.
	Emulating full actuation with two motors instead of the usual six or more.
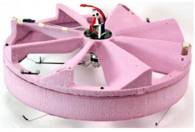	A single motor flying vehicle with control in 3D space.
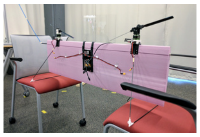	Tandem hovering configuration for a tailsitter airplane.

Table 9.1: Flight validation experiments.

Much like in a quadrotor, the entire propeller may be viewed as a single interchangeable component that may be discarded and replaced when damaged. We have also shown that the rotor can be constructed as a monolithic molded component with localized flexures, making it amenable to mass production on the same scale as rigid propellers.

Beyond conventional capabilities, this technology allows a coaxial helicopter to emulate full actuation over forces and moments while using only two motors. Similar holonomic or omnidirectional aircraft have previously only been possible using at least six motors by augmenting conventional aircraft formats with even more rotors or ancillary actuators. The separation of rotational and translational dynamics allows the aircraft to rapidly respond to lateral disturbances without pitching or rolling, or to orient the body independent of the spatial motion trajectory. These features enable level camera views while maneuvering, an important trait for MAV serving in their traditional role as observational platforms. Such aircraft also support future applications requiring contact and manipulation of the environment with both forces and torques.

Further exotic aircraft formats and capabilities are enabled by this compact actuator, some of which have previously been infeasible or impractical. It provides a new solution for steering control in recently developed single-motor spinning body MAV, allowing one actuator to control a vehicle in 3D space during flight experiments. Such simple aircraft could prove extremely inexpensive to produce and easy to deploy in large swarms. With two rotors in a tandem configuration, a tailsitter airplane with no additional control surfaces can maneuver in hover and has demonstrated transition into forward flight for vertical takeoff and landing (VTOL) operations. Reducing the actuation redundancies found in contemporary VTOL aircraft may extend their operational range, decrease their production cost, and reduce their complexity to those who operate and maintain them.

The pivotal innovation of the last century underpinning manned vertical flight has been cyclic blade pitch control practiced with a mechanical swashplate. Today's extreme pressures to miniaturize, reduce cost, reduce complexity, and eliminate the need for skilled maintenance in micro air vehicles have now brought quadrotors to the forefront. The quadrotor has been made practical by new high power density electronic drives as well as the compact computation and inertial sensing required for active stability. These same technologies can now be leveraged to practice cyclic control as the natural dynamic response to modulation of a single motor's torque, gaining control over thrust, roll, and pitch all from one motor and rotor. In doing so much of the complexities of helicopters of the past have been eliminated while preserving their operational elegance and aerodynamic efficiency. Extracting this expressive control from a single actuator can streamline and extend the endurance of existing rotorcraft, add new capabilities such as simultaneous torque and force control, and promote innovative new types of aircraft with minimal actuation.

Appendices

Appendix A

Motor Drive System Identification

The predictive accuracy of the overall propeller model is critically dependent on having an accurate model for the combined electromagnetic motor and associated drive electronics. Commercial off the shelf motors for MAV applications are typically not fully specified by the manufacturer and are susceptible to manufacturing variations from device to device. Furthermore, the hardware implementation details of commercial motor controllers are typically proprietary. This chapter describes two system identification methods appropriate for dealing with uncertain motor and drive properties. The first strategy requires use of an external torque sensor, and the second requires no such sensor. The methods themselves are elementary. However, the results provide a justification for the simplified motor model structure chosen in this work. Additionally, we may compare the two experimental methods' identified parameters for the combined drive-motor system with the typical naive approach of ignoring the drive electronics' impact and assuming datasheet values for the motor.

As in Chapter 3, we will assume the basic DC motor model given by Eq. 3.41 and repeated below in Eq. A.1 with slightly different notation. The motor velocity ω accelerates subject to the instantaneous motor torque τ and hub inertia I_h. The torque τ is a function of the electrical current i, constant no load current i_0, and motor electromotive force constant K_e. The current is driven by an applied terminal voltage V and subject to speed ω, constant

K_e, and effective series resistance R.

$$\begin{aligned} \dot{\omega} &= \frac{1}{I_h}\tau \\ \tau &= K_e(i - i_0) \\ i &= \frac{1}{R}(V - K_e\omega) \end{aligned} \tag{A.1}$$

This system is linearized about an operating speed Ω to obtain Eq. A.2. In Eq. A.2 and through the rest of this chapter ω and τ implicitly refer to variations from the steady state.

$$\begin{aligned} \dot{\omega} &= \frac{1}{I_h}\tau \\ \tau &= \frac{K_e}{R}(V - K_e\omega) \end{aligned} \tag{A.2}$$

The system identification problem reduces to identifying three parameter quantities: the motor constant K_e, effective resistance R, and rotational inertia I_m.

A.1 Method 1: Speed and Torque Measurement

The three parameters K_e, R, and I_m can be identified by experimentally observing both the torque and speed frequency response to applied voltage. A linear first order ODE in velocity is obtained in Eq. A.3 by eliminating the variable τ from Eq. A.2. This immediately yields the velocity transfer function from V to ω given by Eq. A.4.

$$\dot{\omega} + \frac{K_e^2}{I_m R}\omega = \frac{K_e}{I_m R}V \tag{A.3}$$

$$\frac{\omega}{V} = \frac{1}{K_e} \cdot \frac{1}{\frac{IR}{K_e^2}s + 1} = \frac{1}{K_e} \cdot \frac{\frac{K_e^2}{IR}}{s + \frac{K_e^2}{IR}} \tag{A.4}$$

Experimentally, the motor is run at speed with an additive applied sinusoidal input V and the gain magnitude and phase of the velocity response ω are collected into a Bode plot. A first order transfer function fit to the data identifies two parameter groups: K_e associated with the steady state gain and the product IR associated with the location of the single

Table A.1: Quanum MT 2212 motor properties from speed and torque.

parameter	value
K_e	$9.54 \times 10^{-3}\,\mathrm{V/(rad/s)}$ or Nm/A
R	$0.305\,\Omega$
I_h	$3.26 \times 10^{-6}\,\mathrm{kgm^2}$

Table A.2: AP03 motor properties obtained by speed and torque.

parameter	value
K_e	$2.37 \times 10^{-3}\,\mathrm{V/(rad/s)}$ or Nm/A
R	$1.46\,\Omega$
I_h	$4.02 \times 10^{-8}\,\mathrm{kgm^2}$

pole.

Measuring the reaction torques with a torque transducer during the experiment finally allows us to disambiguate I and R. The transfer function from V to τ is given by Eq. A.5. The parameter R can be determined from the group K_e/R using the previously identified value for K_e. Finally, the inertia I can be calculated from previously determined product IR.

$$\frac{\tau}{V} = \frac{K_e}{R} \cdot \frac{\frac{IR}{K_e^2}s}{\frac{IR}{K_e^2}s + 1} = \frac{K_e}{R} \cdot \frac{s}{s + \frac{K_e^2}{IR}} \tag{A.5}$$

This procedure was applied to the Quanum MT 2212 motor to determine the motor parameters used in [64]. The data and fitted transfer function are presented in Fig. A.1-A.4 for the Quanum MT 2212 motor and the much smaller AP03 motor. Two data series are shown for each motor, each conducted at different motor speeds and different voltage input drive amplitudes. The resulting fitted parameter values obtained by this method are given in Table A.1-A.2.

The fitted transfer function describes the magnitude plots well throughout the entire frequency test range from 1 Hz to 100 Hz. The phase measurements show some additional unmodeled phase loss at high frequency which is most evident in the speed plots beginning around 200 rad/s. This phase error in the speed response likely represents the time delay

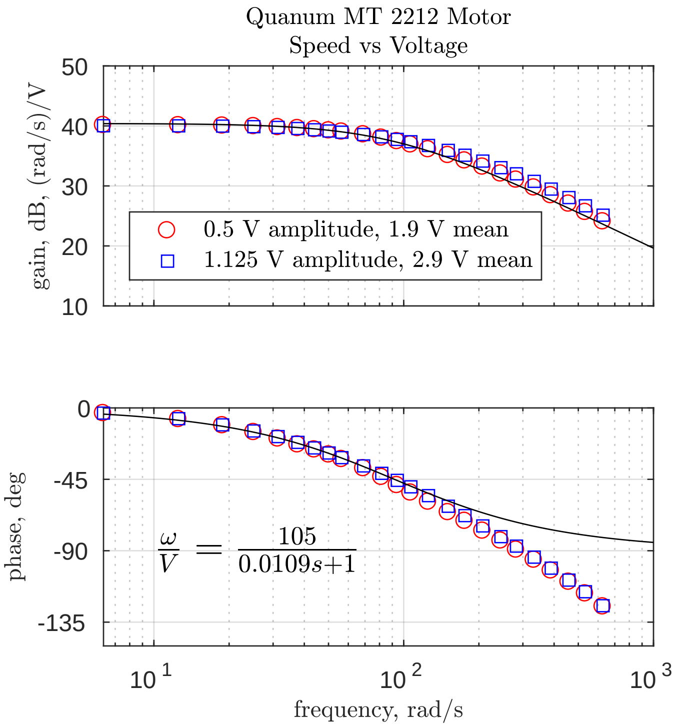

Figure A.1: Speed frequency response for medium 22 mm size motor.

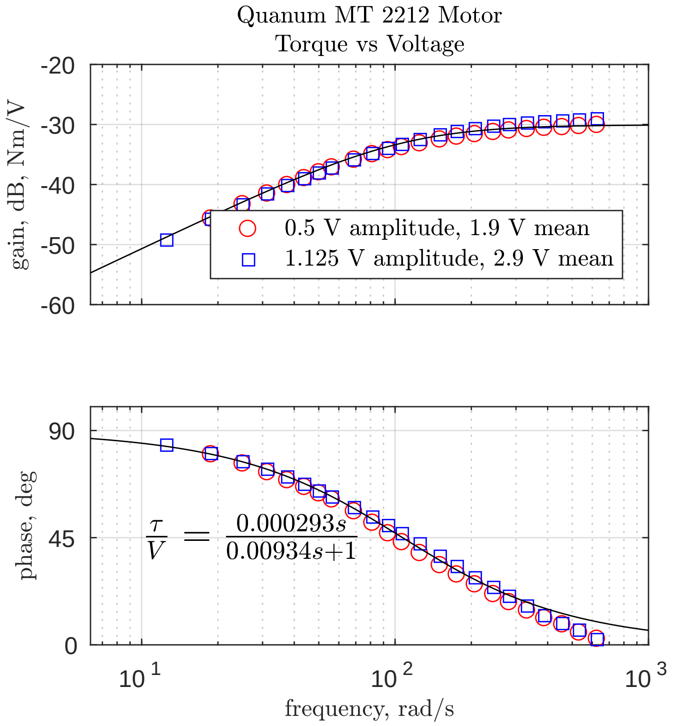

Figure A.2: Torque frequency response for medium 22 mm size motor.

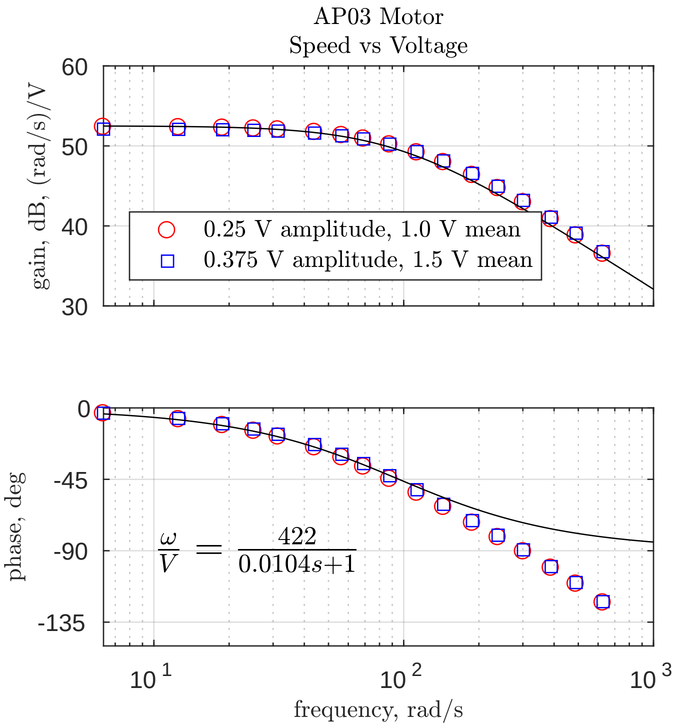

Figure A.3: Speed frequency response for small 11 mm size motor.

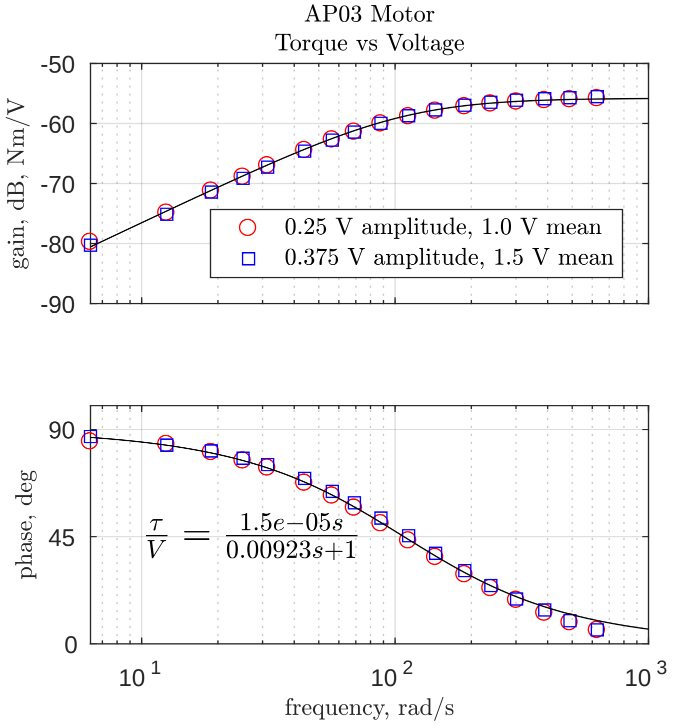

Figure A.4: Torque frequency response for small 11 mm size motor.

associated with discrete speed sampling from the encoder as well as the action of an applied digital low pass filter with a cutoff frequency of 250 Hz for these tests. As a result of such unmodeled effects, the fitted transfer functions for the speed and torque response show slightly different pole locations, even though the characteristic equation for both should be identical under the model. This causes the order of procedure for calculating R and I from the transfer function coefficients described earlier to make small difference to their final determined value. The second parameter identification methodology described below avoids this apparent difficulty, and the nature of the modeling errors will be discussed there in more detail.

A.2 Method 2: Speed Measurement with Proof Mass Flywheel

Motor parameters K_e, R, and I can alternatively be determined using only speed measurements by observing the frequency response to applied voltage with two or more different known added inertial loads. Since the dynamic range of torque transducers is limited, this method may be more convenient for very small motors like the AP03 or very large motors like the U13. It can also be accomplished without any external instrumentation, requiring only the ability to manufacture disks with a known inertia.

The applied voltage to speed variation transfer function for the motor inertia I with an added inertia I_j is shown in Eq. A.6, modified from Eq. A.4. The added inertia will tend to reduce the time constant $(I + I_j)R/K_e^2$ as shown in the Bode plots of Fig. A.5 and A.7.

$$\frac{\omega}{V} = \frac{1}{K_e} \cdot \frac{1}{\frac{(I+I_j)R}{K_e^2}s + 1} \tag{A.6}$$

As before, the two fitted transfer function coefficients can be used to calculate the two parameter groups K_e and the product $(I + I_j)R$. By repeating the experiment $N >= 2$ times with known values of I_j we can find the least squares solution for I and R by solving N equations in two unknowns. This regression can be illustrated graphically as in Fig. A.8

Table A.3: U13 motor properties from flywheel tests.

parameter	value
K_e	$0.109\,\mathrm{V/(rad/s)}$ or $\mathrm{Nm/A}$
R	$0.140\,\Omega$
I	$1.05 \times 10^{-3}\,\mathrm{kgm^2}$

Table A.4: AP03 motor properties from flywheel tests.

parameter	value
K_e	$2.44 \times 10^{-3}\,\mathrm{V/(rad/s)}$ or $\mathrm{Nm/A}$
R	$1.40\,\Omega$
I_h	$3.92 \times 10^{-8}\,\mathrm{kgm^2}$

and A.6, where the y-intercept gives the inertia-resistance product with zero added inertia from flywheels.

As the motor control designer we have some additional insight into the filter dynamics of the speed measurement. For these experiments the encoder is oversampled at high rate and passed to a first order low pass filter with corner frequency of $f_c = 1000\,\mathrm{Hz}$. The measurements are then sampled at 2000 Hz causing an effective zero order hold with period T. The expected transfer function from true speed ω to observed speed $\hat{\omega}$ is given by Eq. A.7. In practice only the residual frequency response is fitted to the motor model, reducing the modeling discrepancy discussed in Section A.1.

$$\frac{\hat{\omega}}{\omega} = \frac{1}{\frac{1}{2\pi f_c}s + 1} \times \frac{1}{s}(1 - e^{-Ts}) \tag{A.7}$$

Figures A.5 and A.7 show the total modeled transfer function fit in solid lines and the associated motor model in dashed lines to depict the corrective impact of this measurement model which is most apparent at higher frequencies.

The final fitted parameters for the large U13 motor and the small AP03 motor are given in Table A.3 and A.4. These values are used for the interpretation of the scaling tests. It was feasible to test the AP03 motor using both methods, and the resulting values agree within 4 %.

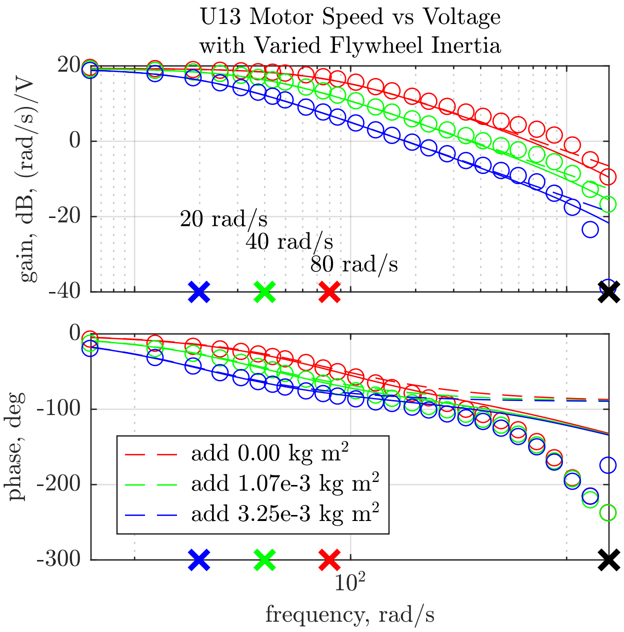

Figure A.5: Speed frequency response of large U13 105 mm size motor with inertial flywheel.

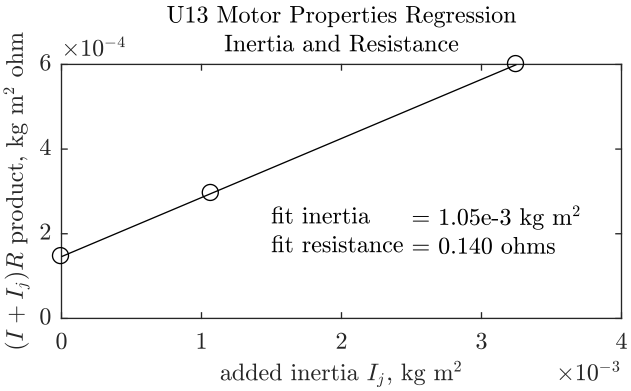

Figure A.6: Inertia regression for large U13 105 mm size motor.

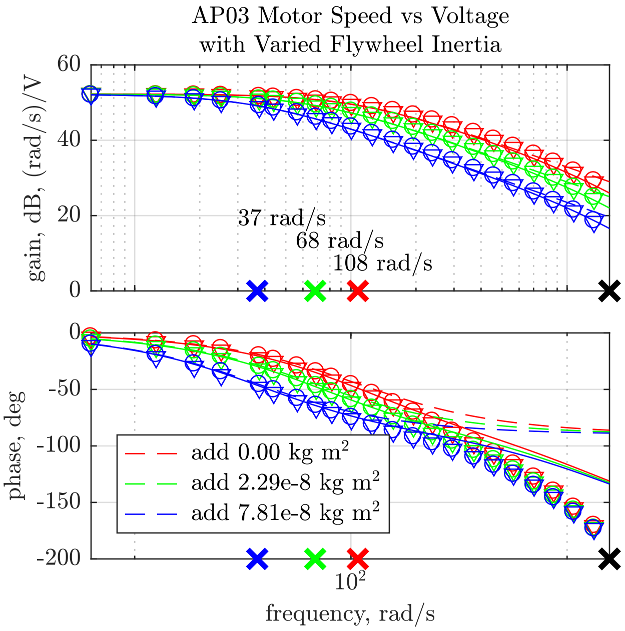

Figure A.7: Speed frequency response of small AP03 11 mm size motor with inertial flywheel.

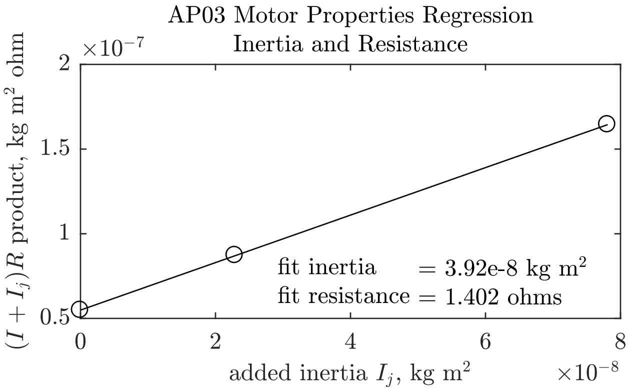

Figure A.8: Inertia regression for small AP03 11 mm size motor.

Bibliography

[1] P. Abbeel, A. Coates, and A. Y. Ng, "Autonomous helicopter aerobatics through apprenticeship learning," *The International Journal of Robotics Research*, vol. 29, no. 13, pp. 1608–1639, Jan. 11, 2010. DOI: `10.1177/0278364910371999`.

[2] J. Alvarenga, N. I. Vitzilaios, M. J. Rutherford, and K. P. Valavanis, "Scaled control performance benchmarks and maneuvers for small-scale unmanned helicopters," in *2015 54th IEEE Conference on Decision and Control (CDC)*, Dec. 2015, pp. 6035–6042. DOI: `10.1109/CDC.2015.7403168`.

[3] M. G. Ballin, "A high fidelity real-time simulation of a small turboshaft engine," NASA, TM-100991, Jul. 1988.

[4] M. Bangura, H. Lim, H. J. Kim, and R. Mahony, "Aerodynamic power control for multirotor aerial vehicles," in *2014 IEEE International Conference on Robotics and Automation (ICRA)*, May 2014, pp. 529–536. DOI: `10.1109/ICRA.2014.6906906`.

[5] C. Bermes, S. Leutenegger, S. Bouabdallah, D. Schafroth, and R. Siegwart, "New design of the steering mechanism for a mini coaxial helicopter," in *2008 IEEE/RSJ International Conference on Intelligent Robots and Systems (IROS)*, Sep. 2008, pp. 1236–1241. DOI: `10.1109/IROS.2008.4650769`.

[6] S. Bouabdallah, C. Bermes, S. Grzonka, C. Gimkiewicz, A. Brenzikofer, R. Hahn, D. Schafroth, G. Grisetti, W. Burgard, and R. Siegwart, "Towards palm-size autonomous helicopters," *Journal of Intelligent & Robotic Systems*, vol. 61, no. 1, pp. 445–471, 2011. DOI: `10.1007/s10846-010-9483-y`.

[7] W. G. Bousman, "The effects of structural flap-lag and pitch-lag coupling on soft inplane hingeless rotor stability in hover," NASA, TP-3002, May 1, 1990.

[8] D. Brescianini and R. D'Andrea, "Design, modeling and control of an omni-directional aerial vehicle," in *2016 IEEE International Conference on Robotics and Automation (ICRA)*, May 2016, pp. 3261–3266. DOI: `10.1109/ICRA.2016.7487497`.

[9] D. Brescianini, M. Hehn, and R. D'Andrea, "Quadrocopter pole acrobatics," in *2013 IEEE/RSJ International Conference on Intelligent Robots and Systems (IROS)*, Nov. 2013, pp. 3472–3479. DOI: `10.1109/IROS.2013.6696851`.

[10] A. Briod, A. Klaptocz, J.-C. Zufferey, and D. Floreano, "The AirBurr: A flying robot that can exploit collisions," in *2012 International Conference on Complex Medical Engineering (ICME)*, Jul. 2012, pp. 569–574. DOI: `10.1109/ICCME.2012.6275674`.

[11] C. J. Brooks, C. V. MacDonald, L. Donati, and M. J. Taber, "Civilian helicopter accidents into water: Analysis of 46 cases, 1979-2006," *Aviation, Space, and Environmental Medicine*, vol. 79, no. 10, pp. 935–940, Oct. 1, 2008. DOI: `10.3357/ASEM.2247.2008`.

[12] B. Crowther, A. Lanzon, M. Maya-Gonzalez, and D. Langkamp, "Kinematic analysis and control design for a nonplanar multirotor vehicle," *Journal of Guidance, Control, and Dynamics*, vol. 34, no. 4, pp. 1157–1171, 2011. DOI: `10.2514/1.51186`.

[13] M. Cutler and J. P. How, "Analysis and control of a variable-pitch quadrotor for agile flight," *Journal of Dynamic Systems, Measurement, and Control*, vol. 137, no. 10, pp. 101 002–101 002, Jul. 1, 2015. DOI: `10.1115/1.4030676`.

[14] M. Cutler, N. K. Ure, B. Michini, and J. P. How, "Comparison of fixed and variable pitch actuators for agile quadrotors," in *AIAA Guidance, Navigation, and Control Conference*, Portland, Aug. 2011. DOI: `10.2514/6.2011-6406`.

[15] N. Dadkhah and B. Mettler, "System identification modeling and flight characteristics analysis of miniature coaxial helicopter," *Journal of the American Helicopter Society*, vol. 59, no. 4, pp. 1–16, Oct. 2014. DOI: `10.4050/JAHS.59.042011`.

[16] N. Dadkhah and B. Mettler, "Control system design and evaluation for robust autonomous rotorcraft guidance," *Control Engineering Practice*, Advanced Software Engineering in Industrial Automation (INCOM'09), vol. 21, no. 11, pp. 1488–1506, Nov. 2013. DOI: `10.1016/j.conengprac.2013.04.011`.

[17] C. De Wagter and E. J. Smeur, "Control of a hybrid helicopter with wings," *International Journal of Micro Air Vehicles*, vol. 9, no. 3, pp. 209–217, Sep. 1, 2017. DOI: `10.1177/1756829317702674`.

[18] "Drehflügler, rotorsystem und steuerung," WO2005087587 A1, Sep. 22, 2005.

[19] S. Driessens and P. Pounds, "The triangular quadrotor: A more efficient quadrotor configuration," *IEEE Transactions on Robotics*, vol. 31, no. 6, pp. 1517–1526, Dec. 2015. DOI: `10.1109/TRO.2015.2479877`.

[20] S. Driessens and P. Pounds, "Towards a more efficient quadrotor configuration," in *2013 IEEE/RSJ International Conference on Intelligent Robots and Systems (IROS)*, Nov. 2013, pp. 1386–1392. DOI: `10.1109/IROS.2013.6696530`.

[21] A. Duyar, Z. Gu, and J. S. Litt, "A simplified dynamic model of the T700 turboshaft engine," presented at the American Helicopter Society Annual Forum, 3-5 Jun. 1992, United States, Jun. 1, 1992.

[22] P. Ferrell, B. Smith, B. Stark, and Y. Chen, "Dynamic flight modeling of a multimode flying wing quadrotor aircraft," in *2013 International Conference on Unmanned Aircraft Systems (ICUAS)*, May 2013, pp. 398–404. DOI: `10.1109/ICUAS.2013.6564714`.

[23] W. Fredericks, R. McSwain, B. Beaton, D. Klassman, and C. Theodore, "Greased Lightning (GL-10) flight testing campaign," NASA, TM-2017-219643, Jul. 2017.

[24] M. A. Garratt, A. J. Lambert, and H. Teimoori, "Control of hover for a micro-air-vehicle using a visual snapshot," in *Proceedings of the 2011 Australasian Conference on Robotics and Automation*, Dec. 7, 2011.

[25] S. George and P. Samuel, "On the design and development of a coaxial nano rotorcraft," in *50th AIAA Aerospace Sciences Meeting*, Nashville, TN, Jan. 9, 2012. DOI: `10.2514/6.2012-585`.

[26] S. Han, A. D. Straw, M. H. Dickinson, and R. M. Murray, "A real-time helicopter testbed for insect-inspired visual flight control," in *2009 IEEE International Conference on Robotics and Automation (ICRA)*, May 2009, pp. 3055–3060. DOI: `10.1109/ROBOT.2009.5152667`.

[27] G. Heredia, A. Ollero, M. Bejar, and R. Mahtani, "Sensor and actuator fault detection in small autonomous helicopters," *Mechatronics*, vol. 18, no. 2, pp. 90–99, Mar. 2008. DOI: `10.1016/j.mechatronics.2007.09.007`.

[28] M. Hirschberg, "To boldly go where no unmanned aircraft has gone before: A half-century of DARPA's contributions to unmanned aircraft," in *48th AIAA Aerospace Sciences Meeting Including the New Horizons Forum and Aerospace Exposition*, Orlando, Florida: American Institute of Aeronautics and Astronautics, Jan. 2010. DOI: `10.2514/6.2010-158`.

[29] G. K. Hunt, "Similarity requirements for aeroelastic models of helicopter rotors," in *RAE Technical Report 72005 (ARC 33730)*, 1972.

[30] T. Hylton, C. Martin, R. Tun, and V. Castelli, "The DARPA Nano Air Vehicle Program," in *50th AIAA Aerospace Sciences Meeting Including the New Horizons Forum and Aerospace Exposition*, Nashville: American Institute of Aeronautics and Astronautics, Jan. 2012. DOI: `10.2514/6.2012-583`.

[31] G. Jiang and R. Voyles, "Hexrotor UAV platform enabling dextrous interaction with structures - flight test," in *2013 IEEE International Symposium on Safety, Security, and Rescue Robotics (SSRR)*, Oct. 2013, pp. 1–6. DOI: `10.1109/SSRR.2013.6719377`.

[32] E. Johnson and D. Schrage, "The Georgia Tech unmanned aerial research vehicle: GTMax," in *AIAA Guidance, Navigation, and Control Conference and Exhibit*, Austin, TX: American Institute of Aeronautics and Astronautics, Aug. 11, 2003.

[33] W. Johnson, *Helicopter Theory*, revised. New York: Dover Publications, 1994, 1120 pp.

[34] K. Karydis and V. Kumar, "Energetics in robotic flight at small scales," *Interface Focus*, vol. 7, no. 1, p. 20 160 088, Feb. 6, 2017. DOI: `10.1098/rsfs.2016.0088`.

[35] D.-H. Kim, J.-W. Chang, and J. Chung, "Low-Reynolds-Number effect on aerodynamic characteristics of a NACA 0012 airfoil," *Journal of Aircraft*, vol. 48, no. 4, pp. 1212–1215, 2011. DOI: `10.2514/1.C031223`.

[36] K. Kondak, F. Huber, M. Schwarzbach, M. Laiacker, D. Sommer, M. Bejar, and A. Ollero, "Aerial manipulation robot composed of an autonomous helicopter and a 7 degrees of freedom industrial manipulator," in *2014 IEEE International Conference on Robotics and Automation (ICRA)*, May 2014, pp. 2107–2112. DOI: `10.1109/ICRA.2014.6907148`.

[37] E. Kraft, "A quaternion-based unscented Kalman filter for orientation tracking," in *Proceedings of the Sixth International Conference of Information Fusion, 2003*, vol. 1, Jul. 2003, pp. 47–54. DOI: `10.1109/ICIF.2003.177425`.

[38] V. Kumar and N. Michael, "Opportunities and challenges with autonomous micro aerial vehicles," *The International Journal of Robotics Research*, vol. 31, no. 11, pp. 1279–1291, Sep. 1, 2012. DOI: `10.1177/0278364912455954`.

[39] A. Kushleyev, D. Mellinger, C. Powers, and V. Kumar, "Towards a swarm of agile micro quadrotors," *Autonomous Robots*, vol. 35, no. 4, pp. 287–300, Nov. 1, 2013. DOI: `10.1007/s10514-013-9349-9`.

[40] T. Lee, M. Leok, and N. H. McClamroch, "Geometric tracking control of a quadrotor UAV on SE(3)," in *49th IEEE Conference on Decision and Control (CDC)*, Dec. 2010, pp. 5420–5425. DOI: `10.1109/CDC.2010.5717652`.

[41] G. J. Leishman, *Principles of Helicopter Aerodynamics*, 2nd ed. Cambridge: Cambridge University Press, 2006, 864 pp.

[42] Y. Long and D. J. Cappelleri, "Complete dynamic modeling, control and optimization for an over-actuated MAV," in *2013 IEEE/RSJ International Conference on Intelligent Robots and Systems*, Nov. 2013, pp. 1380–1385. DOI: `10.1109/IROS.2013.6696529`.

[43] R. D. Lorenz, "Flight power scaling of airplanes, airships, and helicopters: Application to planetary exploration," *Journal of Aircraft*, vol. 38, no. 2, pp. 208–214, 2001. DOI: `10.2514/2.2769`.

[44] A. Macwan, "Application of a novel underactuated propeller technology to the design of a vertical take-off and landing flying wing," M.S.E. Thesis, University of Pennsylvania, Philadelphia, 2017.

[45] L. Marinello, "Dynamics, linear control, and simulation for a holonomic micro air vehicle," B.A. Thesis, Bryn Mawr College, 2017.

[46] A. M. Mehta, D. Rus, K. Mohta, Y. Mulgaonkar, M. Piccoli, and V. Kumar, "A scripted printable quadrotor: Rapid design and fabrication of a folded MAV," in *Robotics Research*, ser. Springer Tracts in Advanced Robotics 114, M. Inaba and P. Corke, Eds., 2016, pp. 203–219. DOI: `10.1007/978-3-319-28872-7_12`.

[47] L. Meier, D. Honegger, and M. Pollefeys, "PX4: A node-based multithreaded open source robotics framework for deeply embedded platforms," in *2015 IEEE International Conference on Robotics and Automation (ICRA)*, May 2015, pp. 6235–6240. DOI: `10.1109/ICRA.2015.7140074`.

[48] D. Mellinger and V. Kumar, "Minimum snap trajectory generation and control for quadrotors," in *2011 IEEE International Conference on Robotics and Automation (ICRA)*, May 2011, pp. 2520–2525. DOI: `10.1109/ICRA.2011.5980409`.

[49] B. Mettler, C. Dever, and E. Feron, "Scaling effects and dynamic characteristics of miniature rotorcraft," *Journal of Guidance, Control, and Dynamics*, vol. 27, no. 3, pp. 466–478, 2004. DOI: `10.2514/1.10336`.

[50] M. Mueller and R. D'Andrea, "Relaxed hover solutions for multicopters: Application to algorithmic redundancy and novel vehicles," *The International Journal of Robotics Research*, vol. 35, no. 8, pp. 873–889, 2016. DOI: `10.1177/0278364915596233`.

[51] Y. Mulgaonkar, G. Cross, and V. Kumar, "Design of small, safe and robust quadrotor swarms," in *2015 IEEE International Conference on Robotics and Automation (ICRA)*, May 2015, pp. 2208–2215. DOI: `10.1109/ICRA.2015.7139491`.

[52] Y. Mulgaonkar, M. Whitzer, B. Morgan, C. M. Kroninger, A. M. Harrington, and V. Kumar, “Power and weight considerations in small, agile quadrotors,” in *Proceedings of SPIE*, vol. 9083, 2014. DOI: `10.1117/12.2051112`.

[53] H. Murao, H. Tamaki, and S. Kitamura, “Application of reinforcement learning to RC helicopter control,” in *SICE 2003 Annual Conference*, vol. 3, Aug. 2003, 2306–2309 Vol.3.

[54] R. M. Murray, Z. Li, and S. S. Sastry, *A Mathematical Introduction to Robotic Manipulation*. Boca Raton: CRC Press, 1994.

[55] *NASA Langley engineers propose mars flyer concept*, Mar. 2017.

[56] A. Nikou, G. C. Gavridis, and K. J. Kyriakopoulos, “Mechanical design, modelling and control of a novel aerial manipulator,” in *2015 IEEE International Conference on Robotics and Automation (ICRA)*, May 2015, pp. 4698–4703. DOI: `10.1109/ICRA.2015.7139851`.

[57] E. Olson, “AprilTag: A robust and flexible visual fiducial system,” in *2011 IEEE International Conference on Robotics and Automation (ICRA)*, Shanghai, May 2011, pp. 3400–3407. DOI: `10.1109/ICRA.2011.5979561`.

[58] R. A. Ormiston and D. H. Hodges, “Linear flap-lag dynamics of hingeless helicopter rotor blades in hover,” *Journal of the American Helicopter Society*, vol. 17, no. 2, pp. 2–14, Apr. 1, 1972. DOI: `10.4050/JAHS.17.2`.

[59] W. C. Orthwein, *Clutches and Brakes: Design and Selection*, 2nd Ed. New York: Marcel Dekker, Feb. 18, 2004, 364 pp.

[60] J. Paulos and M. Yim, “An underactuated propeller for attitude control in micro air vehicles,” in *2013 IEEE/RSJ International Conference on Intelligent Robots and Systems (IROS)*, Tokyo, Nov. 2013, pp. 1374–1379. DOI: `10.1109/IROS.2013.6696528`.

[61] J. Paulos and M. Yim, “Flight performance of a swashplateless micro air vehicle,” in *2015 IEEE International Conference on Robotics and Automation (ICRA)*, Seattle, WA, May 2015, pp. 5284–5289. DOI: `10.1109/ICRA.2015.7139936`.

[62] J. Paulos, B. Caraher, and M. Yim, *Emulating a fully actuated aerial vehicle using two actuators*, 2018.

[63] J. Paulos, E. Kiderman, J. Mickelson, and B. Gupta, “Micro air vehicle student challenge 2015,” poster, Virginia Beach, VA, Apr. 5, 2015.

[64] J. Paulos and M. Yim, “Cyclic blade pitch control for small UAV without a swashplate,” presented at the AIAA Atmospheric Flight Mechanics Conference, SciTech 2017, Grapevine, TX, Nov. 1, 2017.

[65] J. Paulos and M. Yim, “Scalability of cyclic control without blade pitch actuators,” presented at the Atmospheric Flight Mechanics Conference, 2018 AIAA SciTech Forum, Kissimmee, Florida, Jan. 9, 2018.

[66] M. Piccoli, S. Revzen, and M. Yim, “SEAL Pack versatile, portable, and rapidly deployable sea, air, and land vehicle,” in *2013 IEEE International Symposium on Safety, Security, and Rescue Robotics (SSRR)*, Oct. 2013, pp. 1–6. DOI: `10.1109/SSRR.2013.6719362`.

[67] M. Piccoli and M. Yim, “Passive stability of a single actuator micro aerial vehicle,” in *2014 IEEE International Conference on Robotics and Automation (ICRA)*, May 2014, pp. 5510–5515. DOI: `10.1109/ICRA.2014.6907669`.

[68] M. Piccoli, “Passive stability and actuation of micro aerial vehicles,” Ph.D. Thesis, University of Pennsylvania, Philadelphia, 2016.

[69] M. Piccoli and M. Yim, “Anticogging: Torque ripple suppression, modeling, and parameter selection,” *The International Journal of Robotics Research*, vol. 35, pp. 148–160, 1-3 Jan. 1, 2016. DOI: `10.1177/0278364915599045`.

[70] M. Piccoli and M. Yim, “Piccolissimo: The smallest micro aerial vehicle,” in *2017 IEEE International Conference on Robotics and Automation (ICRA)*, May 2017, pp. 3328–3333. DOI: `10.1109/ICRA.2017.7989378`.

[71] P. E. I. Pounds, D. R. Bersak, and A. M. Dollar, “Practical aerial grasping of unstructured objects,” in *2011 IEEE Conference on Technologies for Practical Robot Applications (TePRA)*, Apr. 2011, pp. 99–104. DOI: `10.1109/TEPRA.2011.5753489`.

[72] P. Pounds, R. Mahony, and P. Corke, “Modelling and control of a quad-rotor robot,” in *Proceedings of the Australasian Conference on Robotics and Automation*, 2006.

[73] P. Pounds, R. Mahony, P. Hynes, and J. M. Roberts, “Design of a four-rotor aerial robot,” in *Proceedings of the 2002 Australasian Conference on Robotics and Automation (ACRA 2002)*, W. Friedrich and P. Lim, Eds., Auckland, New Zealand: Australian Robotics & Automation Association, Nov. 2002, pp. 145–150.

[74] “Propeller blade tip path plane inclining device,” US5259729 A, Nov. 9, 1993.

[75] S. Prothin and J.-M. Moschetta, “A vectoring thrust coaxial rotor for micro air vehicle: Modeling, design and analysis,” presented at the 3AF, 48th International Symposium of Applied Aerodynamics, Saint Louis, France, Mar. 2013.

[76] F. Ruffier and N. Franceschini, “Visually guided micro-aerial vehicle: Automatic take off, terrain following, landing and wind reaction,” in *2004 IEEE International Conference on Robotics and Automation (ICRA)*, vol. 3, 2004, 2339–2346 Vol.3. DOI: `10.1109/ROBOT.2004.1307411`.

[77] A. Salpukas, “Arthur M. Young dies at 89; early helicopter developer,” *The New York Times*, Jun. 3, 1995.

[78] P. Samuel, J. Sirohi, F. Bohorquez, and R. Couch, “Design and testing of a rotary wing MAV with an active structure for stability and control,” presented at the American Helicopter Society Forum 61, Grapevine, TX, 2005.

[79] D. Schafroth, C. Bermes, S. Bouabdallah, and R. Siegwart, “Micro helicopter steering: Review and design for the muFly project,” in *2008 IEEE/ASME International Conference on Mechatronic and Embedded Systems and Applications (MESA)*, Beijing, Oct. 2008, pp. 216–221. DOI: `10.1109/MESA.2008.4735700`.

[80] D. Schafroth, S. Bouabdallah, C. Bermes, and R. Siegwart, “From the test benches to the first prototype of the muFly micro helicopter,” *Journal of Intelligent and Robotic Systems*, vol. 54, pp. 245–260, 1-3 Mar. 1, 2009. DOI: `10.1007/s10846-008-9264-z`.

[81] J. D. Singleton and W. T. Yeager, "Important scaling parameters for testing model-scale helicopter rotors," *Journal of Aircraft*, vol. 37, no. 3, pp. 396–402, 2000. DOI: `10.2514/2.2639`.

[82] A. Stoica, E. Dente, Y. Iwashita, and A. Chiolerio, "UAVs you can't see or hear - a survey of key technologies," in *2015 Sixth International Conference on Emerging Security Technologies (EST)*, Sep. 2015, pp. 50–55. DOI: `10.1109/EST.2015.21`.

[83] *Team Volonomic VI demo video*, Apr. 2, 2017.

[84] M. Turpin, K. Mohta, N. Michael, and V. Kumar, "Goal assignment and trajectory planning for large teams of interchangeable robots," *Autonomous Robots*, vol. 37, no. 4, pp. 401–415, Dec. 1, 2014. DOI: `10.1007/s10514-014-9412-1`.

[85] B. K. Walker, E. Gai, and M. N. Desai, "A fault-tolerant approach to helicopter swashplate control," *Journal of Guidance, Control, and Dynamics*, vol. 8, no. 1, pp. 62–70, 1985. DOI: `10.2514/3.19936`.

[86] B. Wie and P. M. Barba, "Quaternion feedback for spacecraft large angle maneuvers," *Journal of Guidance, Control, and Dynamics*, vol. 8, no. 3, pp. 360–365, 1985. DOI: `10.2514/3.19988`.

[87] C. H. Wolowicz, J. S. Brown, and W. P. Gilbert, "Similitude requirements and scaling relationships as applied to model testing," Aug. 1, 1979.

[88] R. J. Wood, S. Avadhanula, R. Sahai, E. Steltz, and R. S. Fearing, "Microrobot design using fiber reinforced composites," *Journal of Mechanical Design*, vol. 130, no. 5, pp. 052304–052304–11, Mar. 26, 2008. DOI: `10.1115/1.2885509`.